THEORETICAL STUDY OF SOLVATION OF IONS BY ARGON ATOMS

by

Ming-Kang Brad Tsai

BS, National Chiao Tung University, Taiwan, 1997

Submitted to the Graduate Faculty of

The Department of Chemistry in partial fulfillment

of the requirements for the degree of

Doctor of Philosophy

University of Pittsburgh

2005

UNIVERSITY OF PITTSBURGH

FACULTY OF ARTS AND SCIENCES

This dissertation was presented

by

Ming-Kang Brad Tsai

It was defended on

Nov. 18, 2005

and approved by

Kenneth D. Jordan, Ph. D.

David W. Pratt, Ph. D.

Peter E. Siska, Ph. D.

Dan Sorescu, Ph. D.

Kenneth D. Jordan, Ph. D.
Dissertation Director

Advisor: Kenneth D. Jordan, PhD

THEORETICAL STUDY OF SOLVATION OF IONS BY ARGON ATOMS

Ming-Kang Brad Tsai, PhD

University of Pittsburgh, 2005

Gas phase experiments have been used to study the molecular properties of finite systems in order to minimize the environmental perturbations. The measurements conducted in vacuum environment setup the standard reference value of experimental observables which builds up the foundation of non-vacuum scientific researches. The solvents, *e.g.* noble gas atoms, used in the gas phase experiments play an important role. It not only cools down the cluster in order to approach the 0° K but also drastically increase spectroscopic sensitivity. The binding position of the solvent atoms also impacts the interpretation of the experimental results. The aid from the theoretical studies was limited due to the computational expense. Three projects are listed in this thesis to show the theoretical challenges in studying different complex systems. The first project is a model potential development with the inclusion of electron correlation at quantum chemistry level to study the $(H_2O)^-Ar_n$ clusters. The second project is using the *ab inito* calculations to explain the infrared spectroscopic measurement of $Mg^+(H_2O)Ar_n$ clusters. The last project is a study of the complex electronic structure of $Fe^+(H_2O)Ar_n$ clustes with using state-of-the-art *ab intio* methods.

TABLE OF CONTENTS

LIST OF TABLES

LIST OF FIGURES

PREFACE

I cannot image at this moment that I am writing the preface of my Ph.D. thesis. In other words, the last piece of this five-year hard work is going to be finished.

I am so grateful to all the people who have helped me to get where I am now. I would like to thank all the group members, past and present, for the help in all the aspects of my Ph.D. life. Especially, I want to thank Drs. Dominic Alfonso, Thomas Sommerfield, and Feng Wang for the inspiring discussions about my research projects.

I would also want to thank my lovely wife, Su-Fang Yao, for the endless encourage and support for the last five years. Thanks my parents praying for me from the other side of Pacific Ocean days and nights.

Finally, I want to thank my advisor, Prof. Kenneth D. Jordan, for giving me the opportunity to complete my Ph.D. degree in his group and to use the cutting-edge computational facilities to clarify any idea I was interested. His unlimited patience and thorough guidance really leads me to complete project by project successfully.

This is really a wonderful journey.

M. Brad Tsai in Pittsburgh

Nov. 2, 2005

1. INTRODUCTION

Small clusters in gas phase have been intensively studied for decades. For clusters primarily consisted of atoms, some properties, *e.g.* electron detachment energies, ionization potentials, collision induced dissociation cross section, and metastable fraction,[1,2] have been studied by following the size dependence. It was first described by Mackay[3] that clusters forming high symmetric structures have the most intense signal in the mass spectrum. For example, Ar_{13}^+ which forms an icosahedral structure[4] has a stronger signal than the Ar_{12}^+ or Ar_{14}^+ clusters.

For clusters consisting of simple molecule, *e.g.* Ar_n-HF and Ar_n-HCl, the structural information has been obtained by the rotational and vibrational spectroscopic measurements conducted in the microwave[5] and infrared[6,7] regions. However, without the cluster selection process, the measurement quality is limited by the experimental sensitivity and spectral congestion, and prior species identification. Adding the clusters selection procedure, *i.e.* scattering by a second molecular beam,[8-10] much improve the experimental measurement quality on the neutral cluster systems. Besides the neutral clusters, experiments conducted on the ionic cluster systems can use mass spectrometry coupled with laser spectroscopy to provide the cluster size selection.[11-14]

A weakly bound "spectator", first introduced by Y. T. Lee and coworkers,[12,15,16] serves a very important role in the ionic cluster experiment, which couple the mass spectrometry and laser spectroscopy. In the early experiments, H_2 was employed as the spectator, *e.g.* H_3^+-$(H_2)_n$. However, the spectrum was complicated to interpret due to the identifiable vibrational frequency associated with the first and subsequent coordination shells. As a consequence, rare gas atom became the main stream of the tagging technique in the more recent experiments.

The rare gas atom tags not only serve as a cooling agent to keep down the cluster temperature but the perturbations by the rare gas atoms also have the spectroscopic consequences. Dopfer and coworkers have studied the attachment of multiple argon atoms on many cation molecular complexes,[17-22] while Johnson and coworkers have investigated the influence of Ar atoms on the spectroscopy of many anion complexes.[23-29] Although many experiments have been conducted to study the tagging atom effect, theory has not provide much insight into the influence of the Ar atoms on the spectra. That is primarily due to different cores in the experiments present different theoretical challenges. For example, the dipole-bound anion system in Johnson's experiment requires use of very diffuse basis set in order to describe the excess electron, introducing linear dependency problems. For cation clusters, the charge of the core introduces strong polarization on the Ar atoms. It increases the difficulty for the development of polarizable model potentials. Moreover, the sizable polarizability of Ar atoms requires use of appropriate theory level and a decent basis set to describe the dispersion interaction if one considers to use *ab initio* electronic structure calculations.

In the following chapters, three systems involving the interaction of Ar atoms with ionic species are described. The first addresses Ar atom solvation of the dipole-bound water dimer. The second system considered is $Mg^+(H_2O)Ar_n$, and the third system considered is $Fe^+(H_2O)Ar_n$. The methods used in treating these systems vary from a novel model potential, to state-of-the art *ab initio* electronic structure methods.

2. ELECTRON ATTACHMENT TO $(H_2O)_2Ar_n$ CLUSTERS

This work was published as

Tsai, M.-K.; Wang, F.; Jordan, K. D. *J. Phys. Chem. A*. **2004**, *108*, 2912

2.1. ABSTRACT

The neutral and negatively charged $(H_2O)_2Ar_n$, n = 1 – 14, clusters are investigated theoretically by use of a polarizable model potential together, in the case of the anionic clusters, with a Drude-model approach to incorporate dispersion interactions between the excess electron and the Argon atoms and water molecules. The $(H_2O)_2Ar_{11}$ and $(H_2O)_2^-Ar_{12}$ clusters are predicted to be "magic numbers", with their high stability being a result of their global minima adopting icosahedral-like structures. Based on these results, a mechanism for formation of the anions is proposed. In addition, the rapid falloff in intensity of the n ≥ 7 anionic clusters in the observed mass spectrum and the absence of an observable signal for the n = 10 cluster are accounted for.

2.2. INTRODUCTION

Negatively charged water clusters have been the subject of numerous experimental and theoretical studies.[30-46] Although the water monomer does not have a bound anion state, the dimer is a prototypical dipole-bound anion in which the excess electron is bound in a diffuse orbital "trapped" by the dipole field.[46-51] Experimentally, $(H_2O)_2^-$ ions were first produced by

injection of low-energy electrons into the high pressure region of a seeded supersonic expansion.[40-43] The diffuse nature of the excess electron orbital of $(H_2O)_2^-$ was first experimentally demonstrated by Haberland *et al.*,[40,41] who, using electron detachment in an external field, obtained an electron affinity of 17 meV. In these experiments, the supersonic beam was seeded with argon atoms to produce cold clusters. Subsequently, Bowen *et al.*[42,43] determined from photodetachment experiments a value of 45 ± 6 meV for the vertical electron detachment energy (VDE) of $(H_2O)_2^-$. They also observed weak HOH bending and OH stretching vibrational features indicative of a geometry change between the neutral and anionic dimers. Recently, Bouteiller *et al.*[44] reported an adiabatic electron affinity of $(H_2O)_2$ of 30 ± 4 meV from field-detachment of $(H_2O)_2^-$ anions produced by transfer of an electron from Rydberg helium atoms.

Theoretical studies have shown that while $(H_2O)_2$ has a *trans*-like structure the anion has a *cis*-like structure as shown in Figure 1. This geometrical change associated with electron capture is due to the larger dipole moment, and hence, enhanced electron binding for the *cis* orientation of the two water molecules. To a large extent the difference between the recent experimentally determined values of the VDE of $(H_2O)_2^-$ and of the adiabatic EA of $(H_2O)_2$ can be understood in terms of this geometry change.

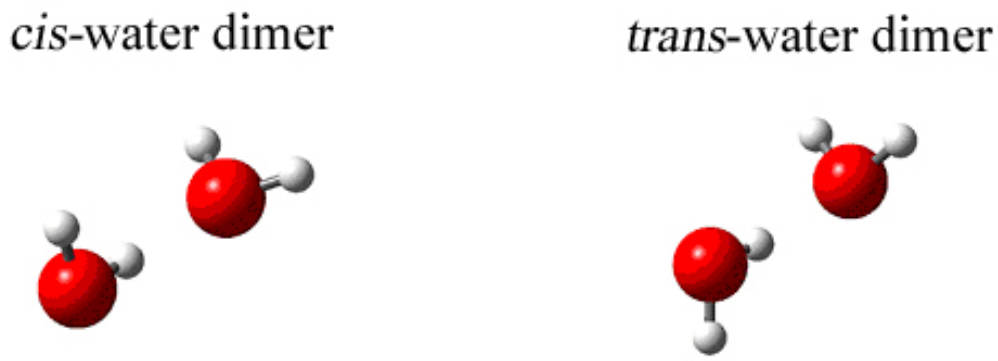

Figure 1: cis- and trans-$(H_2O)_2$. The cis structure is not a potential energy minimum in the absence of the excess electron. The dipole moments are 4.02 and 2.45 D from MP2/aug-cc-pVDZ calculations for cis and trans dimer, respectively.

As noted above, one way of preparing the fragile $(H_2O)_2^-$ species is *via* the interaction of an electron source with a co-expansion of water and argon. The seeding gas helps cool the $(H_2O)_2$ dimer, thereby suppressing vibrational hot bands and electron autodetachment. The co-expansion with argon also leads to mixed $(H_2O)_2^-Ar_n$ clusters. A representative mass spectrum of $(H_2O)_2^-Ar_n$ determined by Ayotte and Johnson[52] is shown in Figure 2. The signals due to the n = 1 and 3 – 6 clusters are of roughly the same intensity, with that due to the n = 2 ion being roughly half as intense. There is a significant falloff in ion intensity for $n > 6$, with no detectable signal for n = 10, and with the n = 9 and 12 clusters appearing with much greater intensity than the n = 11, and 13 – 15 clusters.[52] Interestingly, Corcelli *et al.*[53] have reported a mass spectrum of the $Cl^-H_2O Ar_n$, n = 1 – 13, clusters which displays intense peaks through n = 11 and low intensities for $n \geq 12$. This was interpreted in term of icosahedral closing at n = 11 with the Cl^- ion occupying the center of the icosahedron and a H_2O molecule substituted at one position of the first solvation shell. This raises the question as to whether icosahedral-type arrangements

might also play a role in establishing the intensity pattern in the mass spectrum of the $(H_2O)_2^-Ar_n$ clusters.

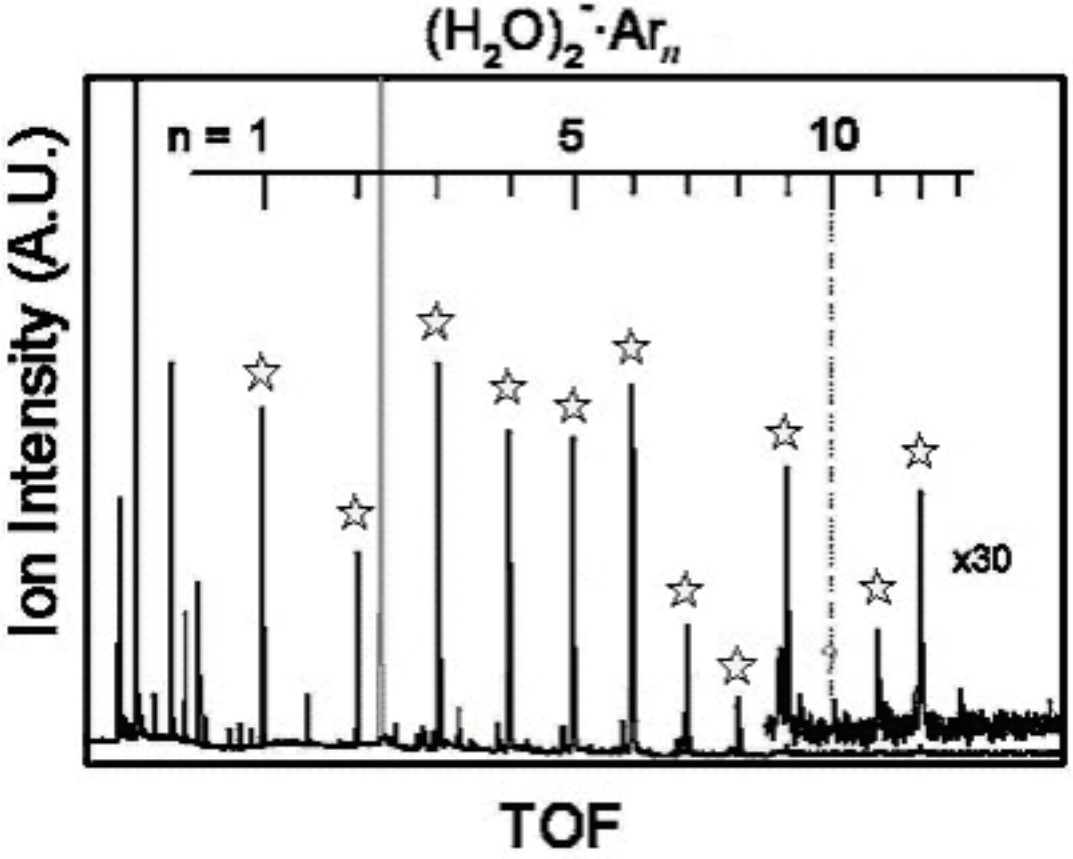

Figure 2: $(H_2O)_2^-Ar_n$ spectrum from M. A. Johnson.[52] The stars denote peaks due to $(H_2O)_2^-Ar_n$. The intense gray peak is due to I^-

In this work the potential energy minima and the finite temperature properties of the $(H_2O)_2Ar_n$ and $(H_2O)_2^-Ar_n$, $n \leq 14$, clusters are investigated theoretically. The goals of the calculations are two fold: (1) to develop a detailed understanding of how the Ar atoms impact the electron binding and (2) to determine whether certain sized clusters are especially stable energetically and whether the observed ion-intensity pattern of $(H_2O)_2^-Ar_n$ reflects the relative stabilities of either the neutral or anionic clusters. Polarization and dispersion interactions

between the excess electron and the Ar atoms necessarily act so as to enhance the electron binding. On the other hand, the presence of argon atoms in the region of space that would otherwise be "occupied" by the excess electron will tend to decrease the electron binding due to the exclusion of the excess electron from regions of space occupied by the Ar atoms (hereafter referred to as an "excluded volume" effect). With regard to the ion-intensity patterns, we recognize from the outset that factors other than energetics can influence cluster distributions. For example, the observation of a particular anion may depend on sufficiently rapid Ar evaporation (from a starting larger cluster) to suppress autoionization. Still there are many examples where it has been established that a mass spectral intensity distribution reflects primarily relative stabilities of the neutral or ionic clusters. One of the best known examples is carbon clusters, for which the fullerene members are especially intense in the positive ion mass spectrum.[54]

2.3. COMPUTATIONAL METHODOLOGY

In order to accurately describe by use of *ab initio* methods the binding of an excess electron to clusters of polar molecules, it is necessary to employ very flexible basis sets and to include electron correlations effects through high order.[46,55-57] As a result, geometry optimizations of the $(H_2O)_2^-Ar_n$, $n \geq 3$, clusters using suitable *ab initio* methods would be computationally prohibitive. In the present study, this problem is dealt with by use of a one-electron model for describing an excess electron interacting with the H_2O molecules and the Ar atoms.

2.3.1. Potential model for the neutral $(H_2O)_2Ar_n$ clusters

The neutral $(H_2O)_2Ar_n$ clusters were described by combining a Lennard-Jones potential for the Ar-Ar interactions, the Dang-Chang (DC) model[58] for the water-water interactions, and the Cohen-Saykally potential[59] for the Ar-water interactions, together with additional terms, described below, to incorporate many-body polarization.

The Lennard-Jones parameters for the Ar-Ar interactions (σ = 3.405 Å and ε = 0.996 kJ/mol)[60] were taken from the literature. The DC water model employs the experimental geometry of the gas-phase monomer (R_{OH} = 0.9572 Å, HOH angle = 104.52°), with two point charges (Q = 0.519e) located at the positions of the H atoms and a third (Q = -1.038e) on the rotational axis, displaced 0.215 Å from the O atom (toward the H atoms). This point-charge distribution gives for H_2O a dipole moment of 1.848 D, nearly identical to the experimental value of 1.825 D[61] and quadruple moment components of Q_{xx}=2.235 D·Å, Q_{yy}= -2.047 D·Å, and Q_{zz}= -0.188 D·Å, in good agreement with experimental values.[62] (Here it is assumed that the molecule is oriented in the xz plane, with the rotational axis being the z axis.) The DC model also locates an isotropic polarizable site at the same position as the negative charge, with the polarizability chosen to reproduce the experimental value. Finally, a single Lennard-Jones site is located on the O atom (σ = 3.2340 Å and ε = 0.763 kJ/mol).

The Cohen-Saykally Ar-water potential is of the form:

$$V(R,\theta,\phi) = V^{rep}(R,\theta,\phi) - \sum_{n=6}^{9} C_n^{ind}(\theta,\phi)R^{-n} - \sum_{n=6}^{9} C_n^{disp}(\theta,\phi)D_n(R)R^{-n} \quad (1)$$

where V^{rep} represents the repulsive interactions, C_n^{ind} and C_n^{disp} are the inductive and dispersion coefficients, respectively, and the D_n are damping factors. The various parameters were

determined by fitting the parameters to 37 vibration-rotation-tunneling transitions observed for the ArH_2O and ArD_2O complexes, subject to constraints to build in the correct long-range behavior.[59] This potential includes a contribution to the interaction energy from the polarization of the Ar atom by the charge distribution of the water monomer.

To include many-body polarization in the composite model described above, Drude oscillators were placed on the Ar atoms and were also substituted for the polarizable site in the DC model for the water monomer. Each Drude oscillator consists of two charges ($+q$ and $-q$) coupled harmonically through a force constant k. The polarizability of a Drude oscillator is given by q^2/k (in atomic units). For water, the k and q values were taken from Ref. [55] (k = 0.103, and q = 1, for which q^2/k value reproduces the polarizability value of the DC model). For Ar, k and q were chosen to be 0.395 and 2.086, respectively. With this choice q^2/k reproduces the experimental polarizability of Ar, and the dispersion energy of Ar_2 calculated using the Drude model closely reproduces the contribution from the R^{-6} term in the Lennard-Jones potential (over the distance range of R = 3 – 8 Å). The many-body polarization interactions were calculated using the standard approach,[53]

where

$$U^{pol} = U_{qp} + U_{pp} + U_{self}\,, \tag{2}$$

with

$$U_{qp} = -\left(\sum_{i=1}^{N_W} p_i^W \cdot E_i^0 + \sum_{k=1}^{N_{Ar}} p_k^{Ar} \cdot E_k^0 \right), \tag{3}$$

$$U_{pp} = -\frac{1}{2}\left(\sum_{i=1}^{N_W} \sum_{j=1, j\neq i}^{N_W} p_i^W \cdot T_{ij} \cdot p_j^W + \sum_{k=1}^{N_{Ar}} \sum_{l=1, k\neq l}^{N_{Ar}} p_k^{Ar} \cdot T_{kl} \cdot p_l^{Ar} \right), \tag{4}$$

$$U_{self} = \sum_{i=1}^{N_W} \frac{p_i^W \cdot p_i^W}{2\alpha_i^W} + \sum_{k=1}^{N_{Ar}} \frac{p_k^{Ar} \cdot p_k^{Ar}}{2\alpha_k^{Ar}}, \quad (5)$$

where U_{qp} describes the interaction energy between the induced dipoles and the electric fields from the permanent charges on other sites, U_{pp} is the interaction energy between the induced dipoles, and U_{self} is the energy needed to create the induced dipoles. In these expressions, E_i^0 is the electric field at polarizable site i due to the permanent charges from the other sites (the charges associated with a water monomer do not interact directly with the polarizable site associated with that monomer), α_i and p_i are, respectively, the polarizability and induced dipole associated with site i, N_W and N_{Ar} are, respectively, the number of water molecules and Ar atoms, and T_{ij} is the dipole tensor.

Because the Cohen-Saykally potential already incorporates two-body polarization interactions between water molecules and Ar atoms, one has to be careful to avoid double-counting of polarization interactions when combining it with Drude oscillators to incorporate many-body polarization. The obvious approach for avoiding the double-counting would be to eliminate the polarization contribution from the Cohen-Saykally potential. However, polarization and dispersion are not cleanly separable in that potential. For that reason, we adopted an alternative strategy of excluding from Eq. 3, the interaction of the Drude oscillators on the Ar atoms with the field due to the charges on the water molecules. We do calculate the induced dipoles on the Ar atoms due to the electric field from the water molecules and use these to include induced dipole – induced dipole interactions between Ar atoms. Although, this approach does omit a subset of the many-body interactions involving both water molecules and the Ar atoms, the errors due to the neglect of these terms should be quite small.

In order to treat the negatively charged clusters, the model potential described above was combined with the Hamiltonian:

$$H^{e} + V^{couple} \tag{6}$$

where H^e is the one-electron Hamiltonian, and V^{couple} gives the coupling between the excess electron and the Drude oscillators. The former is defined as:

$$H^{e} = -\frac{1}{2}\nabla_{e}^{2} + \sum_{i}\frac{Q_i}{r_i} + \sum_{i}\frac{\mu_i \cdot r_i}{r_i^3} + V^{exch-rep}, \tag{7}$$

where (1) the Q_i are the permanent charges associated with the water monomers, (2) the induced dipoles μ_i associated with the Ar atoms and water monomers obtained from solution of Eq. 3-5, and (3) the dispersion-type interactions between the excess electron and the Drude oscillators. $V^{exch-rep}$ describes the repulsive short-range interactions between the excess electron and the Ar atoms and water molecules. The electron-Ar repulsive potential was taken to be the three *s*-type Gaussian representation of Space *et al.*,[60] and the electron-H_2O repulsive potential was taken from a recent paper of Wang and Jordan.[63]

The electron-Drude oscillator coupling is defined as $V^{couple} = \sum_{j}\frac{q_j R_j \cdot r_j}{r_j^3} f(r_j)$ where r_j is a vector between the excess electron and the center of the j^{th} Drude oscillator, R_j is the vector locating the negative charge of the j^{th} oscillator relative to the associated positive charge, and $f(r_j)$ damps out the unphysical short range interactions, with the damping function for the coupling of the excess electron with Drude oscillators associated with the water monomers being taken from Ref. [63]and that for the coupling of the excess electron to the Drude oscillators associated with the Ar atoms being determined in this study. One electron orbitals were used by solving the one-electron Schrödinger equation using large flexible Gaussian-type orbitals to describe the excess

electron. These were used to construct a product basis set of the one-electron orbitals and harmonic oscillator functions to describe each of the Drude oscillators. The electron binding energies were then calculated using the configuration interaction (CI) method.

2.3.2. Geometry optimizations

Analytical gradients have not been worked out for the model potentials used to describe the neutral and anionic $(H_2O)_2Ar_n$ clusters. For this reason, geometries were optimized using the simulated annealing[64] and Powell algorithms[65] as described below.

The geometries of the neutral clusters were optimized for both "*cis*" and "*trans*" orientations of the water dimer as shown in Figure 1. In these calculations the geometries of the $(H_2O)_2$ portions of the mixed $(H_2O)_2Ar_n$ and $(H_2O)_2^-Ar_n$ clusters were taken from MP2 optimizations on the isolated $(H_2O)_2$ and $(H_2O)_2^-$ species, with the OH bond lengths and the HOH angles of the monomers constrained to the experimental values for an H_2O monomer.

The starting structures of the *trans*-$(H_2O)_2Ar_n$ clusters were generated by placing the Ar atoms at random locations in a sphere of radius 3.6 – 9 Å, with the size of the sphere growing with the number of atoms, and its origin being taken as the center-of-mass of the water dimer. For the *cis*-$(H_2O)_2Ar_n$ clusters, three different choices were made for the initial locations of the Ar atoms. The first choice followed the same procedure as used for the *trans*-$(H_2O)_2Ar_n$ clusters. The second placed the Ar atoms in the vicinity of the *H*-donor water molecule. The third choice restricted the initial positions of the Ar atoms to the half sphere opposite the free OH groups. This last choice was motivated by the use of the local minima of the neutral clusters for starting the anion optimizations and by the realization that the presence of Ar atoms near the free OH

groups can prevent electron binding due to an "excluded-volume" effect. To demonstrate the latter effect we consider *cis*-$(H_2O)_2^-Ar$ and *cis*-$(H_2O)_2^-Ar_2$. Drude model calculations predict the most stable forms of these two cluster anions to have structures with the Ar atoms located opposite the free OH groups and with vertical electron detachment energies of 3.2 and 3.0 kJ/mol. There are also higher-lying local minima, shown in Figure 3, with the Ar atoms on the same side of the water dimer as the free OH groups. For these isomers the vertical electron detachment energies are calculated to be only 0.6 and 0.2 kJ/mol for $(H_2O)_2^-Ar$ and $(H_2O)_2^-Ar_2$, respectively. As an increasing number of Ar atoms are located in the vicinity of the free OH groups, the excess electron becomes so weakly bound that, were corrections to the BO approximation made, the electron would cease to be bound even though the dipole moment is larger than the "critical" dipole moment.

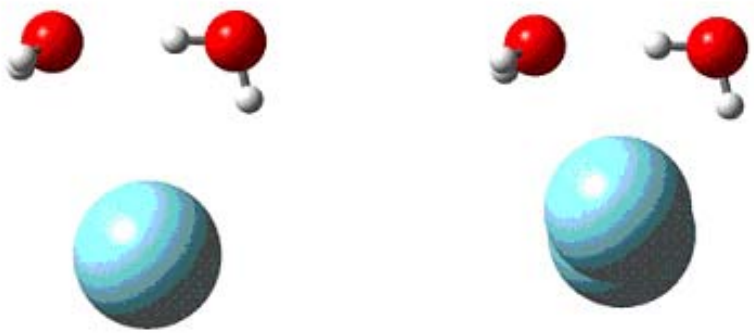

Figure 3: Second lowest-energy isomers of cis-$(H_2O)_2^-Ar$ and cis-$(H_2O)_2^-Ar_2$.

The initial temperature of the simulated annealing procedure was chosen to be 35 K which should be high enough that the barriers on the potential energy surface are readily overcome but low enough to avoid evaporation (at least for the duration of the calculations). It is relevant to observe that a recent simulation of $Ar_{12}HF$ gave two peaks in the heat capacity

curve.[66] The first peak near T = 11 K corresponds to the migration of the HF molecule from the center of the cluster to the surface, and the second peak near T = 30 K corresponds to melting of the cluster. It is anticipated, therefore, that the Ar atoms should be quite mobile at the 35 K initial temperature used to start the simulated annealing optimizations.

For each $(H_2O)_2Ar_n$ cluster with a *trans* arrangement of the water molecules 100 optimizations starting from different initial structures were carried out. For the *cis* clusters, 300 separate optimizations, 100 for each of the three ways of initially locating the Ar atoms, were carried out. The strategy for the optimizations was closely modeled after that used by Corelli *et al.*[53] in their study of $Cl^-H_2OAr_n$ clusters and proceeded as follows:

1. Starting from a given initial structure, a Monte Carlo simulation was carried out for 1000 cycles at T = 0.05 K to give compact structures to avoid evaporation in the subsequent annealing. (A cycle corresponds to one sweep through all the argon atoms.)
2. Starting with the structure obtained from step 1, the cluster was annealed from 35 K to 1 K, in 0.5 K decrements, with 1000 Monte Carlo cycles being performed at each temperature.
3. Starting at 1 K, the temperature was decreased by a factor of two every 500 cycles down to a temperature of 10^{-6} K.

The Monte Carlo steps were carried out with the Metropolis procedure,[67] with the maximum displacements being dynamically adjusted to maintain close to a 50% acceptance rate. Moves that placed Ar atoms within 2 Å of the mass center of the water dimer were rejected.

An analogous optimization approach for the anionic clusters would have been computationally prohibitive even with the use of the Drude model. For that reason we chose

instead to optimize the anionic clusters using the Powell[65] procedure starting from each unique structure obtained from the simulated annealing optimizations of the *cis*-$(H_2O)_2Ar_n$ clusters.

In addition to the geometry optimizations described above, Monte Carlo simulations in the canonical ensemble were carried out for the neutral $(H_2O)_2Ar_n$ clusters at a temperature of 35 K, which is believed to be close to that of the clusters produced experimentally.[68] Actually, clusters with an internal energies in excess of that required to evaporate an argon have finite lifetimes, which makes a rigorous characterization by temperature questionable. This problem was avoided in our simulations by imposing a constraining region comprised of two overlapping spheres centered on the O atoms. The sphere radii ranged from 6.5 Å for n = 1 to 13.5 Å for n = 14. These simulations employed frozen geometries for the water monomers and a fixed O-O distance, but allowed for *cis – trans* isomerization of the water dimer. The simulations consisted of an equilibration stage, followed by 5,000,000 production moves. The geometries were stored every 1000 moves. For each saved structure, the energy of the anion was calculated.

2.4. RESULTS

Before examining the results of the calculations, it is instructive to review the key interaction energies (see Table 1). The binding energy of Ar-H_2O is calculated to be -1.7 kJ/mol as compared with the -1.0 kJ/mol binding energy of the argon dimer, and the 3.33 kJ/mol VDE of *cis*-$(H_2O)_2^-$. Although the energy for converting $(H_2O)_2$ from its "*trans*" global minimum structure to the "*cis*" structure is calculated to be 2.0 kJ/mol, the *cis* form of $(H_2O)_2^-$ is calculated to be about 1.0 kJ/mol more stable than the *trans* form. This can be understood in terms of the enhanced dipole moment of the *cis* structure, which leads to greater electron binding.

Table 1. Relevant energies (kJ/mol).[1]

Ar – Ar binding energy	-1.00
Water – Water binding energy (*trans*)	-19.22
Ar – Water binding energy	-1.71
VDE of *cis*-$(H_2O)_2^-$	3.33
VDE of *trans*-$(H_2O)_2^-$	0.03
trans → *cis* isomerization energy of $(H_2O)_2$	2.05
trans → *cis* isomerization energy of $(H_2O)_2^-$	-0.98

[1]All results obtained using the model potentials described in the text.

To examine the quality of the model potential, we also carried out *ab initio* CCSD(T) calculations[69] of the vertical electron detachment energies of $(H_2O)_2Ar_n^-$, $n = 0 – 2$, clusters using the anion geometries optimized with the one-electron Drude model and with the water monomers held rigid in the *cis* orientation. The *ab initio* calculations were carried out using a basis set generated by adding to a modified aug-cc-pVTZ(-f) basis set,[70,71] seven diffuse *s* and seven diffuse *p* primitive Gaussian functions on the O atom of the acceptor water molecule. The exponents of the supplemental functions were in geometric ratios, ranging from 0.025 to $4*10^{-5}$ for the *s* functions and from 0.06 to $9.6*10^{-5}$ for the *p* functions. (The modification of the aug-cc-pVTZ basis set consisted of substituting for the H and O atoms, respectively, the *p* and *d* functions from the aug-cc-pVDZ basis set.[72] In addition, the *f* functions on the O atoms and the *d* functions on the H atoms, present in the full aug-cc-pVTZ basis set were excluded, hence the "-f" qualifier.) The electron binding energies are summarized in Table 2. For $(H_2O)_2^-$ and $(H_2O)_2^-$ Ar the model potential and the *ab initio* calculations give nearly identical vertical electron detachment energies, but for $(H_2O)_2^-Ar_2$, the value of the VDE obtained with the model potential is about 10% (0.4 kJ/mol) greater in magnitude than that obtained from the *ab initio* CCSD(T)

calculations. However, even in the later case the agreement between the model potential and high-level *ab initio* results is satisfactory.

Table 2. Vertical electron detachment energies (kJ/mol) and computational times for $(H_2O)_2^-Ar_n$, $n = 0 – 2$.

	cis-$(H_2O)_2^-$	*cis*-$(H_2O)_2Ar^-$	*cis*-$(H_2O)_2Ar_2^-$
	CCSD(T)		
VDE	3.20	3.63	4.24
CPU time	1.6 hrs	31.0 hrs	111.5 hrs
	Drude model		
VDE	3.33	3.62	4.62
CPU time	1.3 sec	2.1 sec	3.2 sec

2.4.1. Neutral $(H_2O)_2Ar_n$ clusters

The lowest-energy minima of the neutral *trans*-$(H_2O)_2Ar_n$ and *cis*-$(H_2O)_2Ar_n$ clusters are depicted in Figure 4-Figure **6**. For each cluster size, the *trans* isomer is 2.0 – 2.3 kJ/mol more stable than the *cis* isomer, with this energy difference being close to that associated with isomerization of the bare water dimer. The most stable forms of the *trans*-$(H_2O)_2Ar_n$, $n = 1 – 3$, clusters have the Ar atoms located on the same side of the O-O bond as the free OH group of the acceptor monomer. However, the larger *trans* clusters have Ar atoms on both sides of the O-O bond. The five Ar atoms of *trans*-$(H_2O)_2Ar_5$ form a ring around the O-O axis. This five-membered ring persists in the larger clusters. For the most stable forms of the *cis*-$(H_2O)_2Ar_n$, $n =$ 1 – 3, 5, and 6, clusters the Ar atoms are located on the side of the O-O bond opposite the free OH groups, whereas in the other *cis* clusters there are Ar atoms on both sides of the O-O bond. (Here the “sides” are defined in respect to the plane containing the two O atoms and which is

perpendicular to the plane containing the two O atoms and the free OH group of the donor water molecule.)

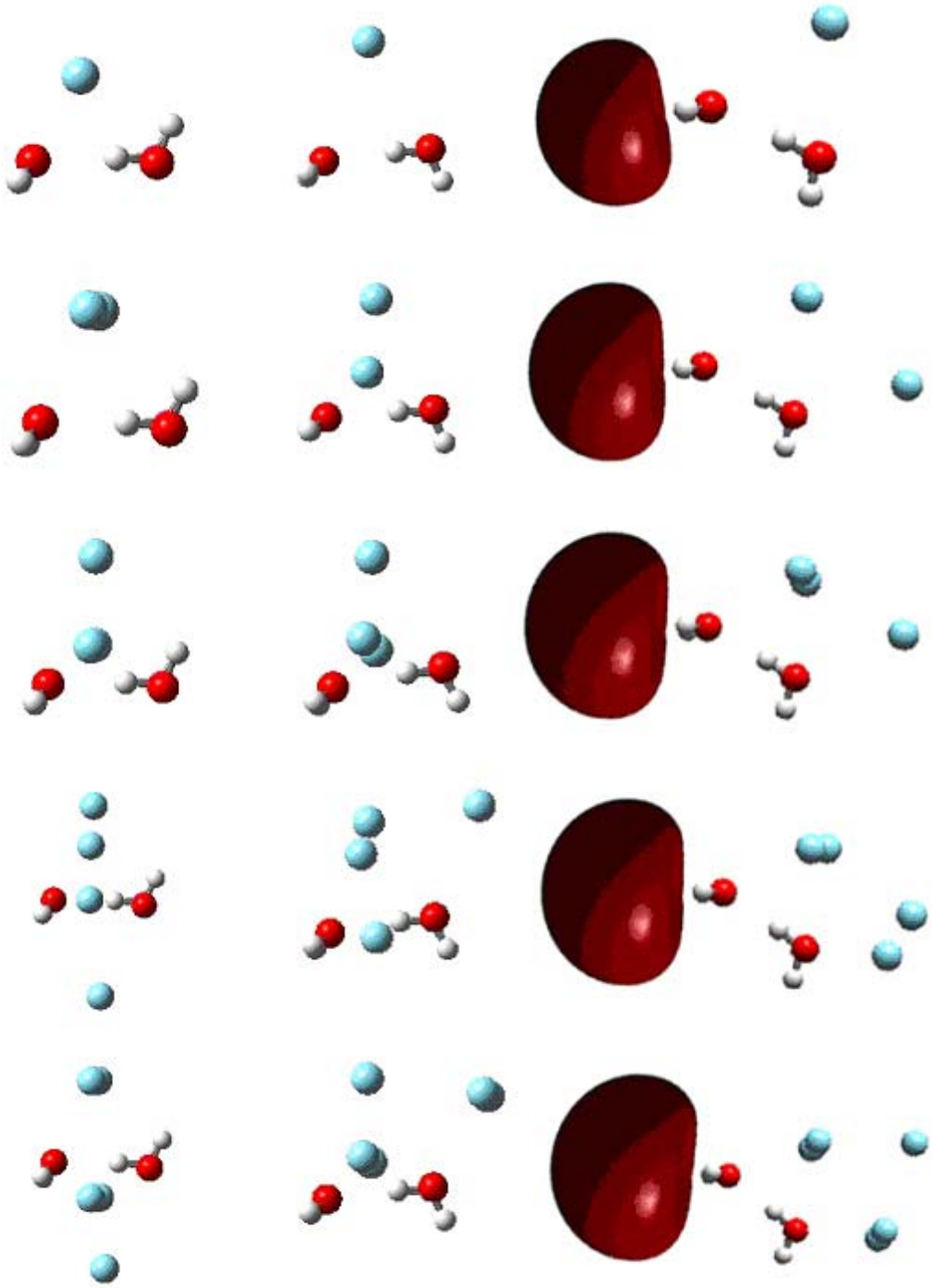

Figure 4: Lowest energy minima of the trans-$(H_2O)_2Ar_n$, cis-$(H_2O)_2Ar_n$, and $(H_2O)_2^-Ar_n$, n = 1 – 5, clusters. The neutral clusters were optimized by use of the simulated annealing procedure and the anionic clusters by means of the Powell algorithm. For the anions, the orbital occupied by the excess electron in the isolated $(H_2O)_2^-$ ion is depicted.

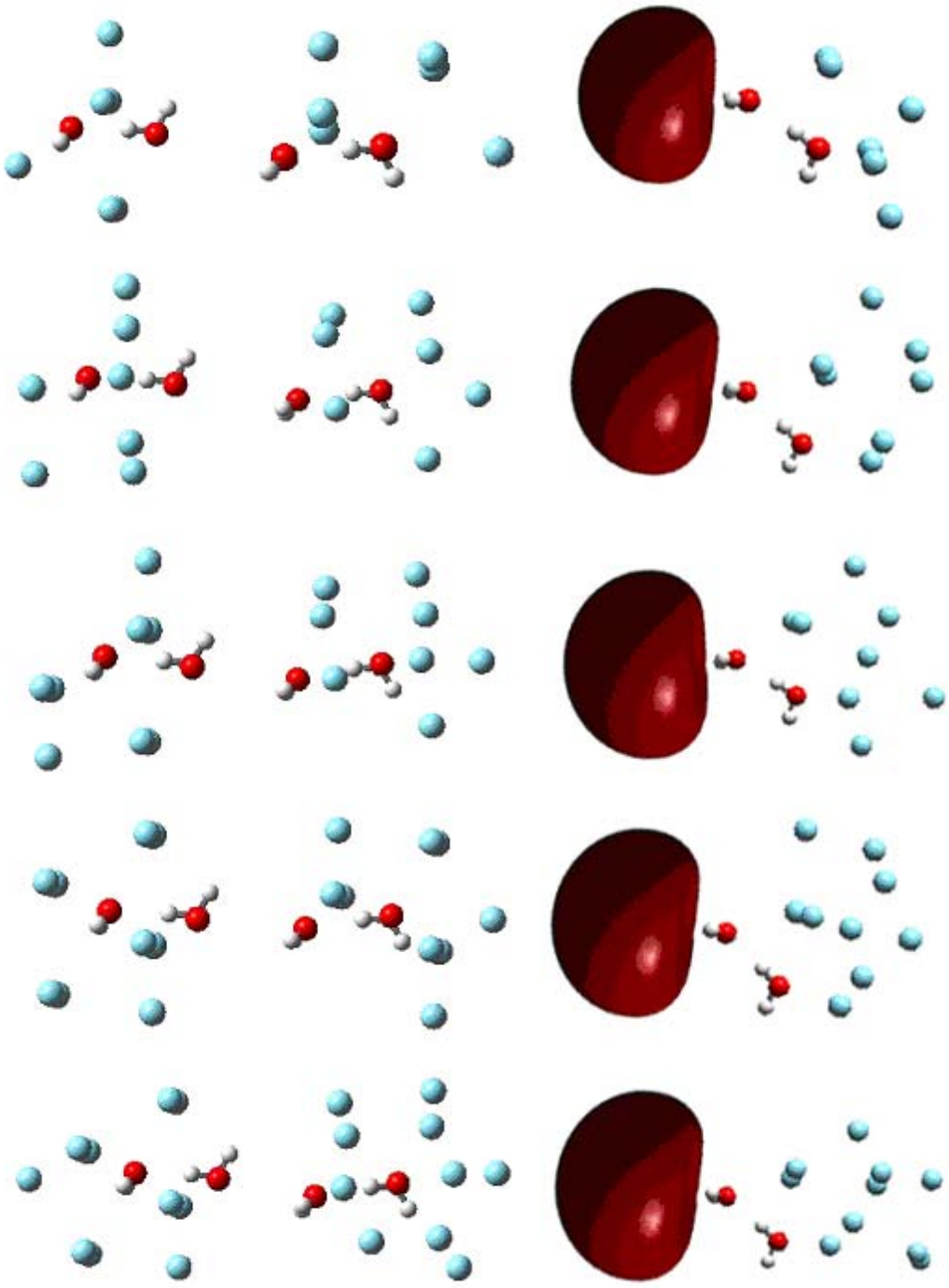

Figure 5: Lowest energy minima of the trans-$(H_2O)_2Ar_n$, cis-$(H_2O)_2Ar_n$, and $(H_2O)_2^-Ar_n$, n = 6 – 10, clusters. The neutral clusters were optimized by use of the simulated annealing procedure and the anionic clusters by means of the Powell algorithm. For the anions, the orbital occupied by the excess electron in the isolated $(H_2O)_2^-$ ion is depicted.

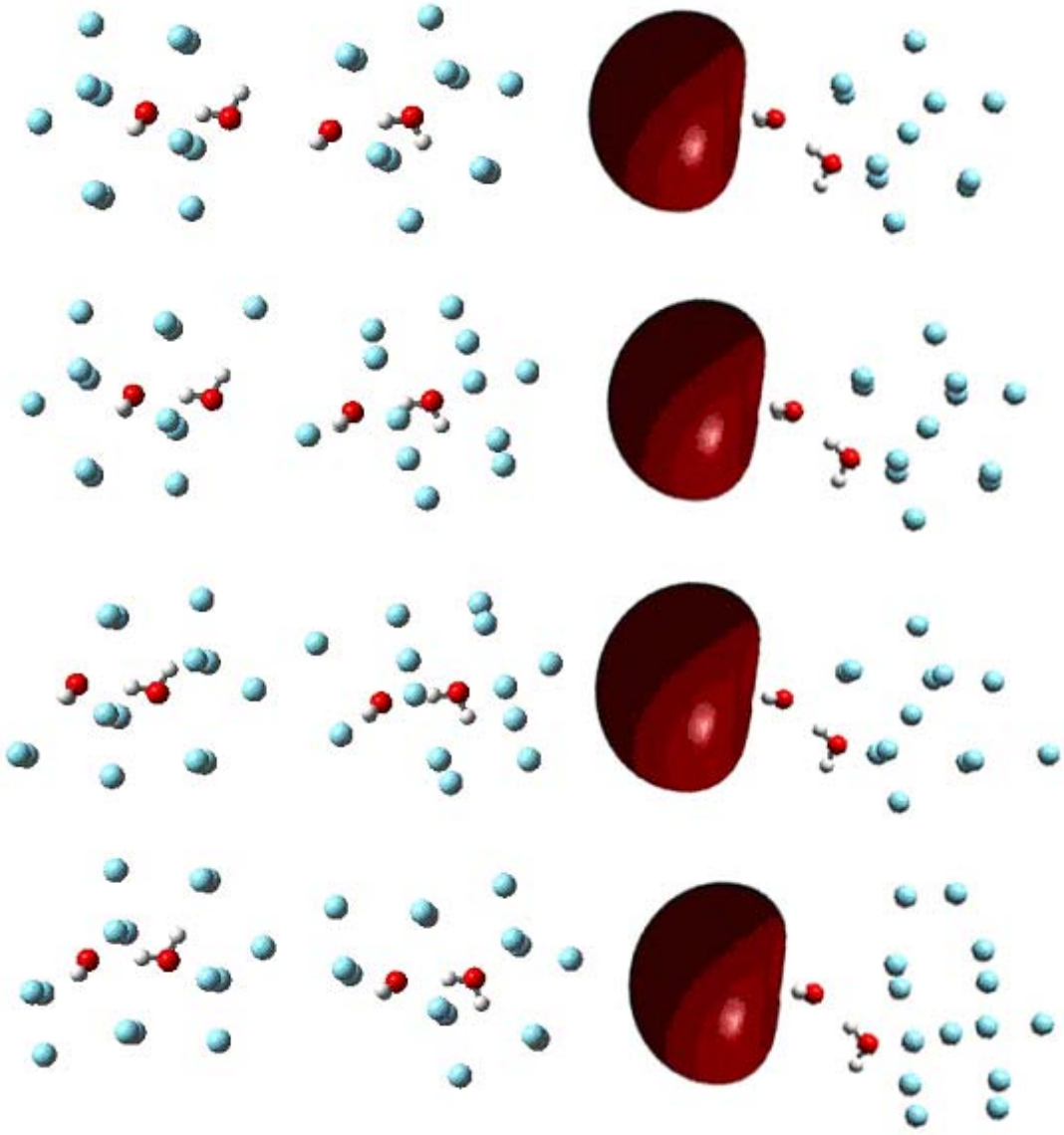

Figure 6: Lowest energy minima of the trans-$(H_2O)_2Ar_n$, cis-$(H_2O)_2Ar_n$, and $(H_2O)_2^-Ar_n$, n = 11 – 14, clusters. The neutral clusters were optimized by use of the simulated annealing procedure and the anionic clusters by means of the Powell algorithm. For the anions, the orbital occupied by the excess electron in the isolated $(H_2O)_2^-$ ion is depicted.

For both the *cis* and *trans* $(H_2O)_2Ar_n$ clusters, the incremental binding energy per Ar atom undergoes a sizable jump in magnitude in going from the $n = 10$ to the $n = 11$ cluster. (See Figure 7.) This is a consequence of the $n = 11$ cluster adopting an icosahedral-like structure, with one water molecule occupying the center site and the other a surface site of the approximate icosahedron.

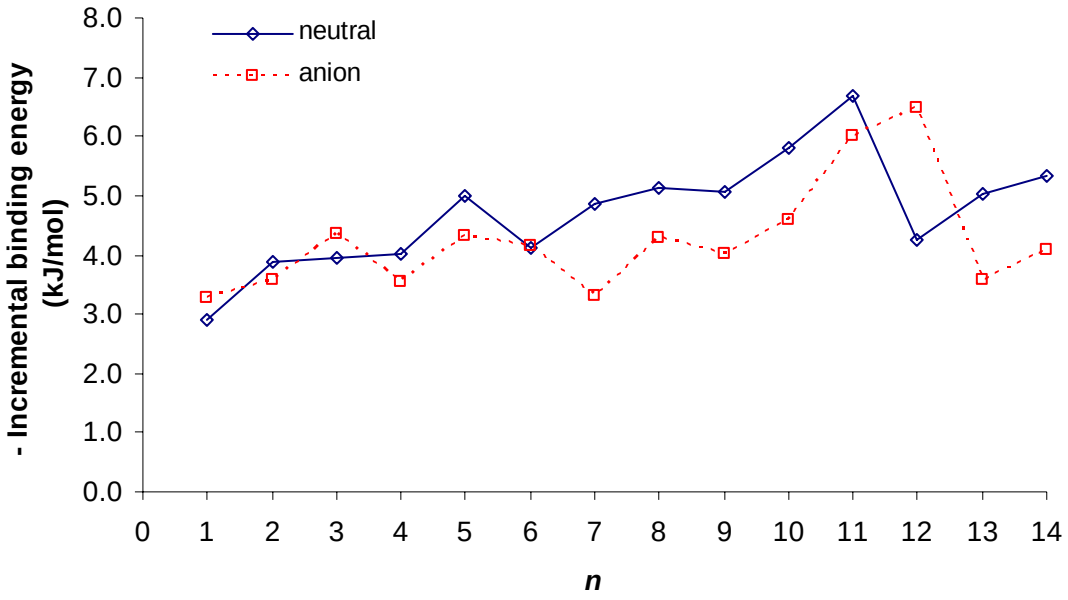

Figure 7: Incremental binding energy, $\Delta E_n^{\circ} = E[(H_2O)_2Ar_n] - E[(H_2O)_2Ar_{n-1}]$ and $\Delta E_n^{-} = E[(H_2O)_2^{-}Ar_n] - E[(H_2O)_2^{-}Ar_{n-1}]$, of the trans-$(H_2O)_2Ar_n$ and cis-$(H_2O)_2Ar_n^{-}$, n = 1 – 14, clusters.

2.4.2. $(H_2O)_2^{-}Ar_n$ clusters

Figure 4-Figure **6** also show the lowest-energy structures of the anionic clusters, and the associated binding energies are summarized in Table 3. In each anionic cluster, the water dimer is

on the surface of the argon cluster with the OH groups of the acceptor monomer (that to which the excess electron binds) pointing away from the argon cluster. The n = 11 and 12 anionic clusters display the largest incremental binding energies per Ar atom, with the change being greater for the n = 12 cluster. (See Figure 7.) The high stability of $(H_2O)_2^-Ar_{12}$ is due to its adopting an icosahedral-like-structure, with the single-donor water molecule occupying one of the sites on the surface of the icosahedron. The most stable forms of the n = 11 and 13 anionic clusters have structures closely related to that of the $(H_2O)_2^-Ar_{12}$ species. The evolution of the icosahedral structure is apparent starting at the n = 5 cluster. We note also that for the n = 13 cluster there is an isomer with an intact Ar_{13} icosahedron "attached" to the H-donor water molecule lying only 1.2 kJ/mol above the global minimum structure.

Table 3. Total energies (kJ/mol) of the most stable forms of the neutral and anionic $(H_2O)_2Ar_m$ clusters.

m	*trans*-$(H_2O)_2Ar_m$[1]		*cis*-$(H_2O)_2Ar_m$[1]		$(H_2O)_2^-Ar_m$		
	E_{tot}	ΔE_m[2]	E_{tot}	ΔE_m[2]	E_{tot}	ΔE_m[2]	VDE
0	-19.22		-17.18		-20.51		3.33
1	-22.11	-2.89	-20.16	-2.99	-23.79	-3.28	3.65
2	-25.99	-3.88	-24.05	-3.88	-27.36	-3.57	4.62
3	-29.94	-3.96	-28.04	-3.99	-31.71	-4.35	4.35
4	-33.97	-4.02	-31.94	-3.90	-35.24	-3.53	4.53
5	-38.95	-4.99	-36.73	-4.78	-39.55	-4.31	5.03
6	-43.05	-4.10	-40.83	-4.11	-43.72	-4.17	4.50
7	-47.91	-4.85	-45.66	-4.83	-47.02	-3.30	5.37
8	-53.03	-5.13	-50.77	-5.11	-51.30	-4.28	4.94
9	-58.11	-5.08	-55.91	-5.14	-55.33	-4.03	5.06
10	-63.91	-5.80	-61.82	-5.91	-59.92	-4.58	5.37
11	-70.59	-6.69	-68.48	-6.66	-65.94	-6.02	5.39
12	-74.85	-4.26	-72.69	-4.21	-72.42	-6.48	5.59
13	-79.89	-5.03	-77.74	-5.06	-76.00	-3.59	5.59
14	-85.22	-5.34	-82.89	-5.15	-80.08	-4.08	6.02

[1]The $(H_2O)_2Ar_m$ clusters were optimized by simulated annealing with the geometries of the $(H_2O)_2$ portions of the clusters kept frozen. The anionic clusters were optimized with the Powell algorithm with the geometry of the $(H_2O)_2^-$ entity frozen at that of the isolated $(H_2O)_2^-$ ion.
[2]$\Delta E_m = E_m - E_{m-1}$.

For $(H_2O)_2^-Ar_n$, $n = 0 - 6$, clusters the most stable form of the anion lies energetically below the most stable form of the neutral cluster, which implies that for these clusters the electron binding more than compensates for the energy required to isomerize the water dimer from *trans* to *cis* together with that required to rearrange the Ar atoms. On the other hand, for the larger clusters, the combined energy cost for isomerizing the water dimer and rearranging the Ar atoms exceeds the electron binding, with the consequence that the $n \geq 7$ clusters have negative adiabatic electron affinities.

2.4.3. Monte Carlo simulations

Table 4 reports for the $(H_2O)_2Ar_n$ clusters the average energies and the numbers of saved configurations from the 35 K Monte Carlo simulations that have electron binding energies greater than 0.26 kJ/mol in magnitude. Clusters with electron binding energies less than about 0.26 kJ/mol in the Born-Oppenheimer approximation are expected not to bind the electron were corrections to the BO approximation included. The number of sampled configurations capable of binding an excess electron (according to the above definition) drops off rapidly with increasing of Ar atoms, and for the $n \geq 9$ clusters, none of the sampled configurations displayed electron binding (based on the 0.26 kJ/mol threshold). Nonetheless, as may be seen from Figure 8, at T = 35 K the neutral cluster does sample configurations that expose the acceptor water molecule and with the water dimer well along the coordinate for *trans* → *cis* isomerization. Even though these structures have BO electron binding energies less than 0.26 kJ/mol, the distortions induced by the incoming electron could lead to appreciable electron binding.

Table 4. The average total energies (kJ/mol) of the neutral $(H_2O)_2Ar_m$ clusters at 35 K,[1] and the number of structures binding an excess electron.

m	average energy	number of configurations binding an excess electron[2]
0	-18.68	2752
1	-21.02	828
2	-23.97	333
3	-27.24	117
4	-30.61	27
5	-34.21	15
6	-38.01	6
7	-41.93	2
8	-46.46	3
9	-51.11	0
10	-56.21	0
11	-62.54	0
12	-66.08	0
13	-70.46	0
14	-74.39	0

[1]The simulations employed rigid water monomers and fixed O-O distances.
[2]Out of a total of 5000 configurations saved from the Monte Carlo simulation of the neutral cluster. A structure is counted as binding an excess electron if the calculated vertical electron detachment energy is $\geq$ 0.26 kJ/mol.

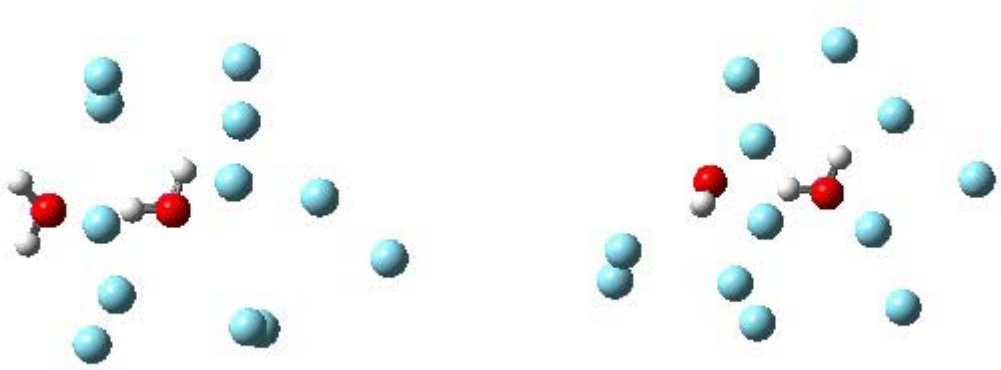

Figure 8: Snapshot configurations of $(H_2O)_2Ar_{12}$ from the T = 35 K Monte Carlo simulation. In the configuration on the left the water dimer is about halfway between the trans and cis arrangements. This configuration would require only a small rearrangement of Ar atoms to bind an excess electron. The configuration on the right would require extensive rearrangement of the Ar atoms to bind an electron.

The $(H_2O)_2^-Ar_n$ clusters observed mass spectroscopically are unlikely to derive from the "parent" $(H_2O)_2Ar_n$ clusters. This is on account of the fact that the resulting anions would be subject to rapid electron autoionization. The most likely mechanism for stabilization of the anions against electron detachment is *via* evaporative loss of an Ar atom,

$$(H_2O)_2Ar_n + e^- \rightarrow (H_2O)_2^-Ar_n \rightarrow (H_2O)_2^-Ar_{n-1} + Ar. \quad (8)$$

The energetics involved in this process can be understood from examination of Figure 9, which reports the potential energy distributions calculated for a subset of the neutral clusters at $T = 35$ K, as well as the thresholds for formation of $(H_2O)_2^-Ar_{n-1}$ and of $(H_2O)_2Ar_{n-1}$.

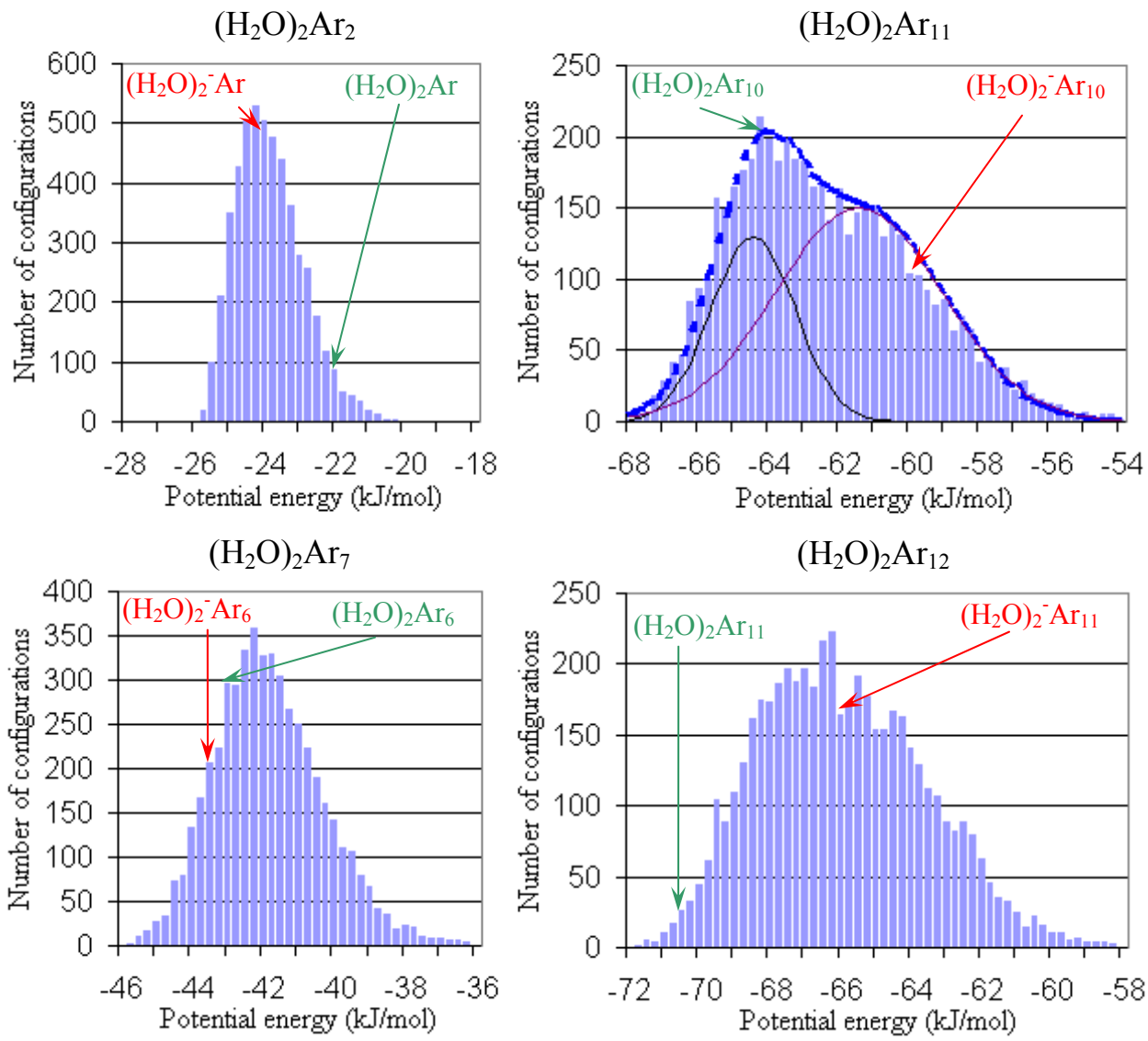

Figure 9: Potential energy distributions of the $(H_2O)_2Ar_n$, n = 2, 7, 11, 12, clusters at T = 35 K. The potential energies have been binned, with the individual bins reporting the number of saved configurations with energy between E - 0.25 and E in kJ/mol. The arrows report the threshold energies for forming the neutral and anionic n-1 clusters. For $(H_2O)_2Ar_{11}$, the net distribution has been decomposed into two overlapping gaussian distributions. The bordered columns correspond to the numbers of potential energy marked along x-axis.

Examination of the potential energy distributions reveals that in all cases the threshold for the electron capture followed by Ar atom loss (Eq. 8) occurs at an energy at which the neutral cluster has sizable population (assuming a cluster temperature of 35 K). Moreover, for the $n \geq 7$ clusters the threshold for this channel lies energetically below that for

$$(H_2O)_2Ar_n + e^- \rightarrow (H_2O)_2^-Ar_n \rightarrow (H_2O)_2Ar_{n-1} + Ar + e^-, \quad (9)$$

which is simply a consequence of the $n \leq 6$ clusters having positive electron affinities. As a result, for a subset of the $(H_2O)_2^-Ar_n$, $n \leq 6$, clusters formed by the electron capture/Ar atom evaporation channel (Eq. 7) further decay by either electron detachment or loss of a second Ar atom is not feasible energetically.

On the other hand, all $n \geq 7$ anionic clusters formed by the mechanism described by Eq. 9, are subject to electron autoionization. We believe that this explains the rapid falloff in anion intensity for the $n \geq 7$ clusters as well as the correlation between the intensity of the *n-1* ion signal in the mass spectrum and the excess energy that must be present in an $(H_2O)_2Ar_n$ cluster for accessing the threshold for formation of $(H_2O)_2^-Ar_{n-1}$. With regard to the latter, the calculations predict the largest excess energies to be for the $n = 10$ and 14 clusters, (10.7 and 9.2 kJ/mol, respectively) which is expected to cause more rapid electron autoionization and could account for the absence (or only very weak signals) for $(H_2O)_2^-Ar_{10}$ and $(H_2O)_2^-Ar_{13}$ in the mass spectrum.

The energy at which the electron capture/Ar evaporation channel opens up is potentially relevant for a second reason, namely, the greater the excess energy in a neutral cluster, the shorter its lifetime towards evaporative loss of an Ar atom. It is estimated that under the experimental conditions used to obtain the mass spectrum reported in Figure 2, the time between

formation of a neutral $(H_2O)_2Ar_n$ cluster and the initial electron capture event is on the order of microseconds.[73] Weerasinghe and Amar have studied using molecular dynamics simulations the lifetimes of the Ar_n, $12 \leq n \leq 14$, clusters as a function of excess energy.[74] These calculations give clusters lifetime on the order of nanoseconds for excess energies on the order of 20 kJ/mol. Based on the present calculations, the largest excess energy required for the opening up of the electron capture/Ar atom loss channel is 10.7 kJ/mol [in the case of $(H_2O)_2Ar_{11}$]. Molecular dynamics calculations carried out by us lead to average lifetimes of microseconds in this case. Thus, the lack of signal due of $(H_2O)_2^-Ar_{10}$ appears not to be due to the absence of $(H_2O)_2Ar_{11}$ precursor with sufficient excess energy to access the electron capture/Ar evaporation channel.

The potential energy distributions obtained from the MC simulations for $(H_2O)_2Ar_{11}$ and $(H_2O)_2Ar_{12}$ clusters are bimodal, which indicates the coexistence of solid-like and liquid-like phase at $T = 35$ K. This was an expected result, since simulations of Ar_{13} predict "solid-liquid" coexistence over a temperature range of 24 – 41 K with a pronounced peak in its heat capacity curve with a maximum at 34 K. Similar transitions have been predicted for the Ar_n, $n = 10 – 12$, clusters, but at somewhat lower temperatures.[75,76]

2.5. CONCLUSIONS

In this investigation, the neutral and anionic $(H_2O)_2Ar_n$, $n = 0 –14$, clusters have been characterized by means of model potentials, with explicit treatment of the excess electron in the case of the anionic clusters. The lowest-energy forms of $(H_2O)_2Ar_{11}$ and $(H_2O)_2^-Ar_{12}$ are predicted to be especially stable and to have icosahedral-like structures. The adiabatic EA is predicted to be positive for the $n \leq 6$ clusters, but negative for the larger clusters. Both the finite

temperature of the neutral cluster and distortions induced by the incoming electron appear to be important in the electron capture process. Moreover, we have proposed that the observed anions have one fewer Ar atom than their neutral precursors, *i.e.*, that the initial electron capture event is followed by rapid ejection of an Ar atom. This provides a mechanism for formation of $(H_2O)_2^-Ar_n$, $n \leq 6$, clusters that are stable against electron ejection or further loss of Ar atoms. On the other hand, the $(H_2O)_2^-Ar_n$, $n \geq 7$, clusters formed by this process are still subject to electron autoionization. This apparently accounts for the rapid falloff in intensity in the $(H_2O)_2^-Ar_n$ mass spectrum for $n \geq 7$. In addition, it is suggested that the absence of signal due to the $(H_2O)_2^-Ar_{10}$ and $(H_2O)_2^-Ar_{13}$ clusters could be due to the rapid autoionization rates of the precursor $(H_2O)_2^-Ar_{11}$ and $(H_2O)_2^-Ar_{14}$ clusters.

2.6. ACKNOWLEDGEMENTS

This research was carried out with support from National Science Foundation. We thank Prof. M. Johnson for making available his $(H_2O)_2Ar_n$ mass spectrum and for helpful discussions. The calculations were performed on computers in the University of Pittsburgh's Center for Molecular and Materials Simulations.

3. INFRARED PHOTODISSOCIATION SPECTROSCOPY OF $Mg^+(H_2O)Ar_n$ COMPLEXES: ISOMERS IN PROGRESSIVE MICROSOLVATION

This work was published as

Walkers, N. R.; Walters, R. S.; Tsai, M.-K.; Jordan, K. D.; Duncan, M. A. *J. Phys. Chem. A*. **2005**, *109*, 7057

3.1. ABSTRACT

Ion-molecule complexes of the form $Mg(H_2O)Ar_n^+$ (n = 1-8) are produced by laser vaporization in a pulsed-nozzle cluster source. These complexes are mass-selected and studied with infrared photodissociation spectroscopy in the O-H stretch region. The spectra are interpreted with the aid of ab initio calculations on the n =1-5 complexes, including examination of various isomeric structures. The combined spectroscopic and theoretical studies indicate the presence of multiple isomeric structures at each cluster size, as the argon atoms assemble around the $Mg^+(H_2O)$ unit. Distinct infrared resonances are measured for argon-on-metal, argon-on-OH and argon-on-two-OH isomers.

3.2. INTRODUCTION

Ion-molecule complexes provide convenient model systems for studies of fundamental molecular interactions and of the detailed potential energy surfaces that govern these. Spectroscopic studies have proven especially valuable for investigating the molecular structure, including the

role of isomeric species that may form of these complexes.[77,78] Recently, metal-containing ions have been included in these studies.[79,80] Metal ion-water complexes are particularly interesting systems with which to explore the details of solvation.[11,81-137] Mass spectrometry studies,[81-99] *ab initio* calculations,[100-111] and various spectroscopic methods[11,112-137] have explored the structures and reactions of these systems. The competition between charge-dipole interactions and the growth of hydrogen bonding networks have been investigated in several recent studies.[11,125-137] In the present paper we describe an infrared spectroscopic study of the $Mg^+(H_2O)$ complex in the OH stretch region as this system is progressively "solvated" by argon atoms. The potential around the cation-water system provides multiple binding sites for argon atoms, and the IR spectra reveal the isomeric structures that form.

Magnesium cation complexes with small molecules and rare gas atoms have been the subject of extensive studies in mass spectrometry, electronic structure calculations, and laser spectroscopy. Collision-induced dissociation methods have determined various ion-ligand bond energies.[82-90] Magnesium cation-water clusters have been studied to investigate intra-complex reactions leading to charge separation ($Mg^+ \rightarrow Mg^{2+} + e^-$) and/or hydroxide formation.[91-98,103-111,115-119] These reactive processes appear to begin when the cation is solvated by five or more water molecules. Electronic spectroscopy of several Mg^+-L complexes near the strongly allowed $3s \rightarrow 3p$ ($^2S \rightarrow ^2P$) atomic transition of Mg^+ using ultraviolet laser photodissociation spectroscopy have been reported.[113,114,138-144] A detailed study of $Mg^+(H_2O)$ determined the structure of this ion and revealed information on its excited state vibronic patterns.[113] A similar study revealed the structure of the closely related $Ca^+(H_2O)$ ion.[114] More recently, Duncan and coworkers have studied $Mg^+(CO_2)_n$ complexes with infrared photodissociation spectroscopy in the region of the CO_2 asymmetric stretch vibration.[145,146] These IR spectroscopy studies have been extended to

$M^+(H_2O)$ complexes for M=V, Fe, Co, Ni.[134,135] In a related infrared study, Inokuchi and coworkers studied the OH-stretch region of $Mg^+(H_2O)_{1-3}$ complexes, revealing the first appearance of hydrogen bonded water at $n = 3$.[136,137] The present IR spectroscopy study builds on this latter work, examining at the spectral changes that occur as argon atoms cluster around the $Mg^+(H_2O)$ system.

Rare gas adducts with ion-molecule complexes have been exploited by several research groups to enhance the measurement of photodissociation spectroscopy.[17-29,134-137,145-153] Duncan and coworkers have studied the infrared photodissociation spectroscopy of *metal* cation-molecular complexes,[134,135,145,146] which includes studies of V^+, Co^+, Ni^+ and Fe^+ complexes[134,135,153] in addition to the present Mg^+ work. In the transition metal-water system,[134,135] isomeric structures in the attachment of one or two argon atoms and one or two water molecules. Inokuchi and coworkers found similar effects for the $Mg^+(H_2O)_{1-3}Ar$ complexes.[136,137] In the present study, $Mg^+(H_2O)Ar_n$ (n = 1-8) complexes is investigated with IR photodissociation spectroscopy and *ab initio* electronic structure calculations.

3.3. EXPERIMENT

Clusters for these experiments are produced by laser vaporization in a pulsed supersonic expansion and mass analyzed in a reflectron time-of-flight mass-spectrometer (TOF-MS). The molecular beam apparatus, mass spectrometer and laser methods used for infrared spectroscopy have been described previously.[146] The third harmonic of a Nd:YAG (355nm) is used to vaporize a rotating magnesium rod, and water is added to the expansion gas *via* a few drops of liquid inserted into the gas flow at ambient conditions. Ionized $Mg^+(H_2O)Ar_n$ clusters are

produced directly from the laser vaporization process in expansions of argon using a pulsed General Valve (1 mm nozzle) at 40 psi backing pressure and a 200 μsec pulse duration. The free expansion is skimmed from the source chamber into the mass-spectrometer and the ions are extracted into the first drift region of the reflectron using pulsed acceleration voltages. Specific ions are mass-selected by pulsed deflection plates just before the reflectron field. Excitation and photodissociation occurs at the turning point in the reflectron field, where ions are overlapped with the output of the infrared laser. Parent and daughter ions are mass-analyzed in the second flight tube and mass spectra are recorded with a digital oscilloscope (LeCroy *WaveRunner* LT342). The data are transferred to a PC *via* an IEEE interface. Infrared resonance enhanced photodissociation (IR-REPD) spectra are obtained by monitoring the intensity of the fragment ions as a function of wavelength.

The infrared laser is an optical parametric oscillator (OPO/OPA) system (Laser Vision) pumped by a Continuum 9010 Nd:YAG. This has two 532 nm-pumped KTP crystals in the grating tuned oscillator section and four KTA crystals in the amplifier section. The idler output from the oscillator is combined with residual 1064 nm in the amplifier, and difference frequency generation here provides the tunable near-IR output from 2.2 to 4.9 μm (4500 to 2050 cm^{-1}). In this experiment, the OPO is unfocused to prevent power broadening. Near 3500-3700 cm^{-1}, the laser pulse energies range from 8-10 mJ/pulse with an approximate linewidth of 0.3 cm^{-1}. Typical spectra are obtained at ~1.2 cm^{-1} steps and averaged over 250 laser shots per step.

3.4. COMPUTATIONAL METHODOLOGY

Ab initio electronic structure calculations were carried out to aid in assigning the observed vibrational structure of the $Mg^+(H_2O)Ar_n$ (n = 0-5) clusters.[154] For each cluster, the geometries were optimized at the MP2 level for various possible isomers, differing in the locations of the Ar atoms. For each stationary point identified, the vibrational frequencies were calculated in the harmonic approximation again using the MP2 method. For the n = 0-3 clusters, calculations were carried out treating all electrons explicitly and using the aug-cc-pVTZ basis set.[70,155] For the n = 0-2 clusters calculations were also carried out using the aug-cc-pVQZ basis set[155,71] to examine the suitability of the smaller aug-cc-pVTZ basis set, and CCSD(T)/aug-cc-pVTZ calculations were carried out to explore the role of high-order correlation effects. Comparable all-electron calculations on the n = 4-5 clusters would be computationally prohibitive, and, therefore, to examine these species, pseudopotentials[156,157] were adopted on the Mg and Ar atoms. The pseudopotentials were employed in conjunction with contracted 4s4p3d2f and 5s5p3d2f Gaussian-type basis sets for Mg and Ar, respectively, generated by augmenting the 2s2p Mg and 4s4p3d1f Ar basis sets of Stoll *et al.*[157] with diffuse functions and, in the case of Mg, polarization functions also taken from the corresponding aug-cc-pVTZ basis sets. As in the all-electron calculations, the aug-cc-pVTZ basis set was employed for the H and O atoms. In order to establish the magnitudes of the errors introduced by the adoption of the pseudopotentials, the n = 0-3 clusters were also characterized using pseudopotentials on the Mg and Ar atoms. In the subsequent discussion the calculations carried out using pseudopotentials are referred to as MP2/PP.

Several possible isomers were considered for the n = 0-4 clusters, whereas only a single structure was considered for the n = 5 cluster. In generating the initial structures, we were

guided by the fact that the Ar atoms are expected to be able to bind to the H atoms as well as to the Mg^+ ion.

3.5. RESULTS AND DISCUSION

3.5.1. Overview of measured spectra

As described previously, infrared photodissociation processes are inefficient in small ion-molecule complexes whose bond energies are significant compared to the infrared photon energies employed to excite vibrational fundamentals. In the $Mg^+(H_2O)$ complex, the cation-water bond energy is 28.4 kcal/mol (9940 cm^{-1}),[84] and thus one-photon photodissociation is not possible in the 3500-3800 cm^{-1} region of the OH stretching vibration, the exception being the small fraction of the complexes that have adequate (about $\geq$ 6000 cm^{-1}) internal energy from incomplete cooling in the cluster growth process.[136,137] These hot clusters have broad spectra. In current experiment, the cluster source is designed for more efficient cooling, and no IR photodissociation of the isolated $Mg^+(H_2O)$ complex is detected. To improve the photodissociation yield of $Mg^+(H_2O)$, Inokuchi and coworkers employed the rare gas tagging method,[17-29,134,135,144,145,147-153] by making mixed complexes containing a single argon atom. The binding energy for the diatomic Mg^+Ar species is 1295 cm^{-1}.[139] Therefore, mixed $Mg^+(H_2O)Ar_n$ complexes dissociate by elimination of argon following absorption in the OH stretch region of the spectrum.[137] The focus here is on the changes in the spectra that take place as argon atoms are sequentially added to the $Mg^+(H_2O)$ cluster.

Figure 10 reports the IR photodissociation spectrum of the $Mg^+(H_2O)Ar$ complex under different experimental conditions. As shown in the upper trace, several bands are observed in the 3500-3800 cm^{-1} region, even though only two IR-active vibrations corresponding to the symmetric and asymmetric stretches of water are expected. The possible role of isomeric structures for these complexes is anticipated. Indeed, Inokuchi and coworkers have reported two isomers, differing in the position of the argon atom for the $Mg^+(H_2O)Ar$ complex.[137] The spectrum under different cluster source and dissociation laser conditions were therefore investigated. In the upper trace of Figure 10, the cluster source was adjusted away from its optimum settings by increasing the vaporization laser power above its normal level and moving the vaporization laser timing away from the most intense part of the pulsed gas expansion. These conditions produced clusters with incomplete cooling. The infrared laser was used at higher laser power (pulse energy approximately 20 mJ/pulse) in a "double-pass" configuration, producing a spectrum with rather broad vibrational resonances. In the center trace, the vaporization laser power and timing were adjusted to the normal settings known to produce colder clusters. The resulting spectrum contains essentially the same bands, but the lines are narrower and the intensity ratios have changed. Finally, the lower trace was obtained by reducing the laser power using only a single pass from the IR laser system (pulse energy approximately 10 mJ/pulse). The bands are again relatively narrow, but the intensity ratios have changed again. In particular, the band near 3531 cm^{-1} has dropped to a level where it is almost missing. These patterns make sense if the bands at 3579/3650 and 3531/3624 cm^{-1} correspond to two different isomeric species, with the higher energy isomer being produced more effectively at higher temperature, and its weaker lines rising in relative importance at higher IR laser power because the more intense bands from the lower energy isomer are saturated. These scans

demonstrate that care must be taken with the conditions used to record spectra. The relative intensities of different bands corresponding to different isomers in these spectra can vary significantly depending on the experimental conditions.

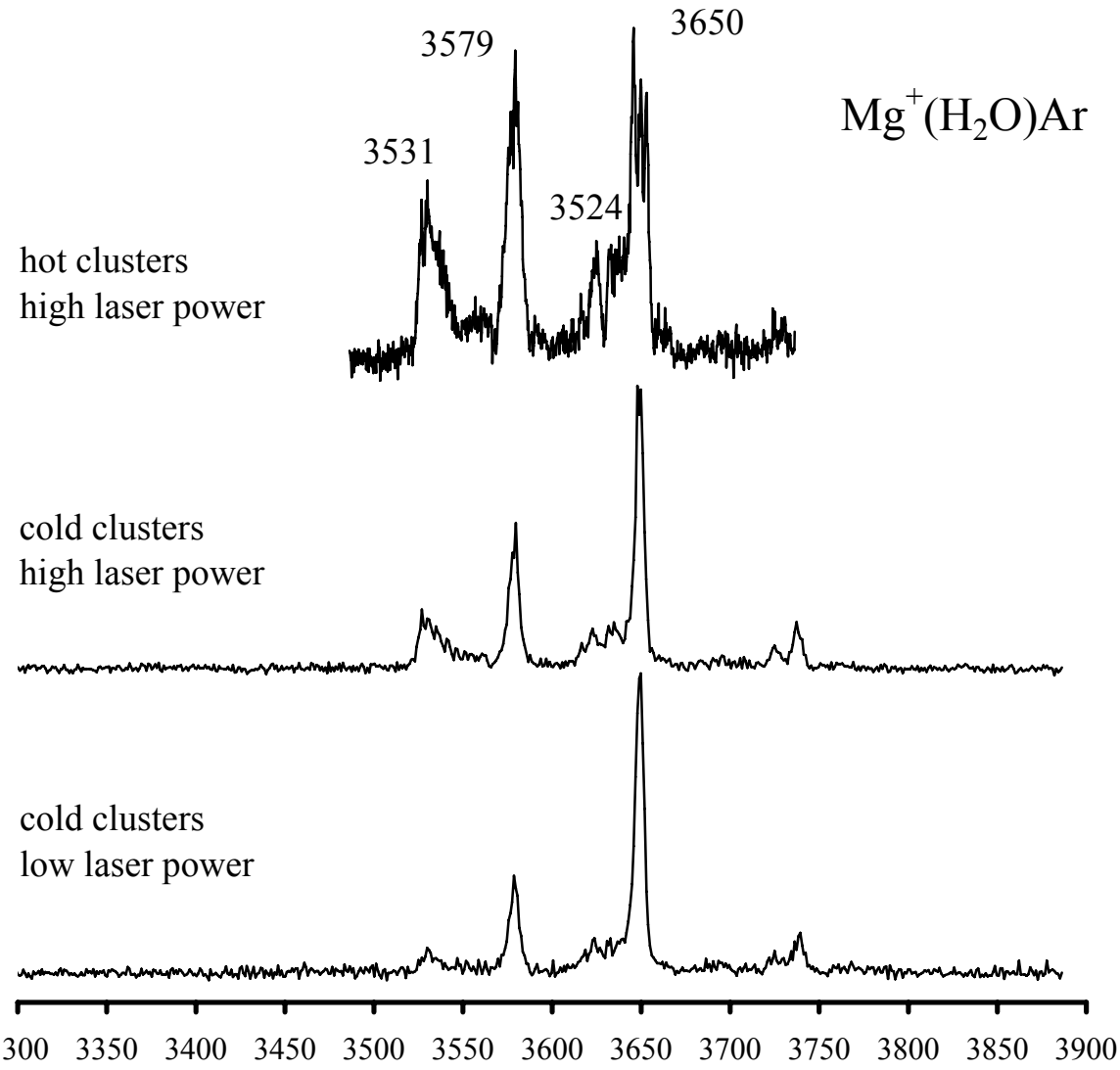

Figure 10. The IR photodissociation spectrum of the $Mg^+(H_2O)Ar$ complex under different experimental conditions.

Figure 11 shows the spectra for the $Mg^+(H_2O)Ar_n$, n = 1-4, complexes obtained from measurements done under the cold conditions described above. The spectra of the n = 1-3 clusters contain multiple bands, again suggesting the possible occurrence of isomeric structures. All of the observed bands are shifted to the red of the symmetric (3657 cm^{-1}) and asymmetric (3756 cm^{-1}) stretch vibrations in the free water molecule (indicated by dashed vertical lines). Such red shifts are expected as the binding of a water molecule to a metal cation leads to withdrawal of bonding electron density from the highest molecular orbitals of water, and this reduces the stiffness of the OH bonds.[134,135] The cation-water binding is so strong that only the C_{2v} structure is expected for the $Mg^+(H_2O)$ sub-system of the complex. Thus the multiple bands seen here arise from isomers differing in the binding sites for the argon atoms. Binding of an Ar atom to Mg^+ should not significantly perturb the OH stretch vibrations, whereas binding of an Ar atom to an OH site should lead to an additional sizable red shift to the O-H stretching vibrations.

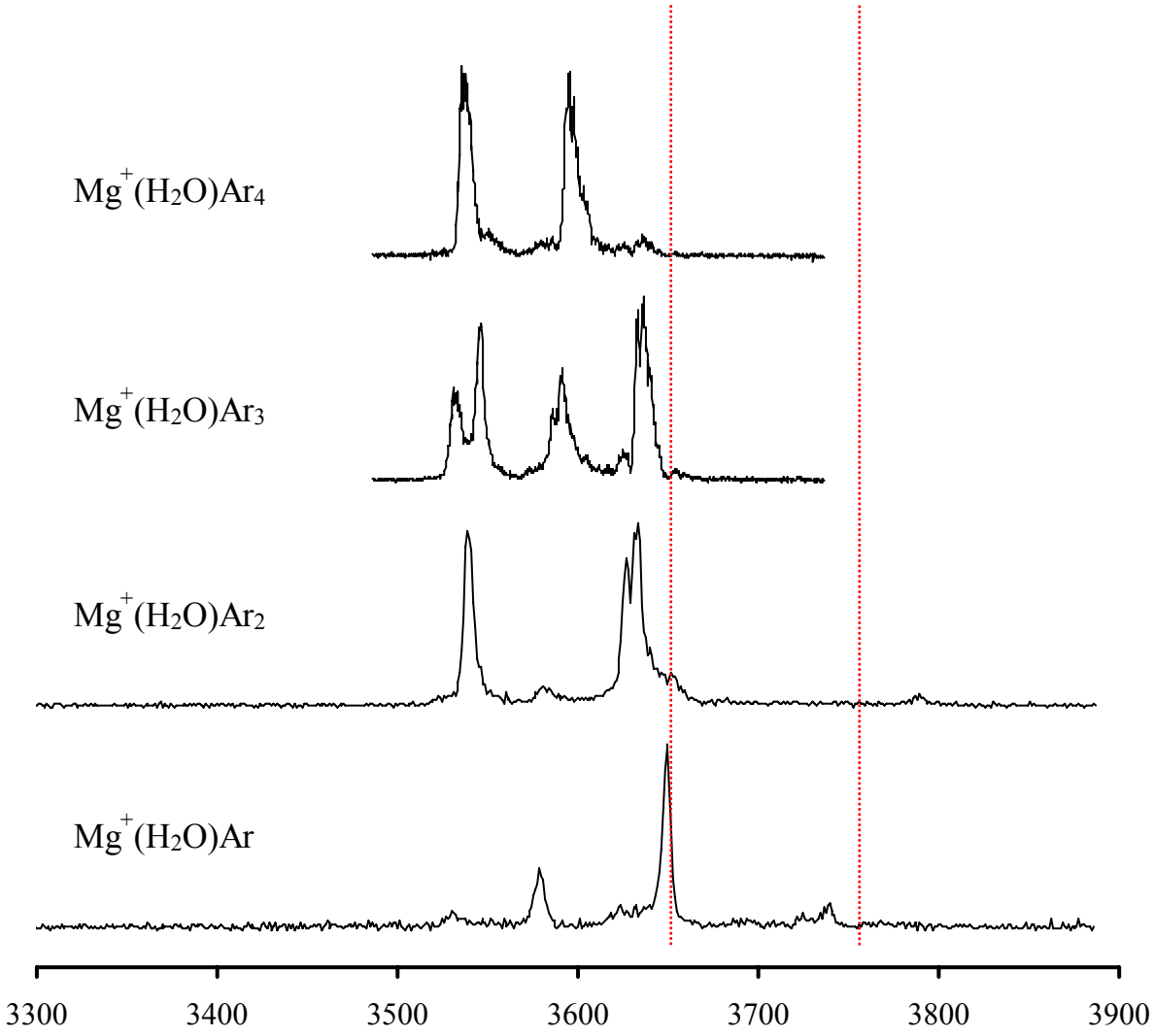

Figure 11. The IR photodissociation spectrum of the $Mg^+(H_2O)Ar_n$, n = 1-4, complexes. The multiple peaks observed in each case suggest the presence of isomeric structures.

3.5.2. Calculated structures and energetics

The low-energy isomeric structures calculated for the $Mg^+(H_2O)Ar_n$ clusters are depicted in Figure 12. The Ar-atom binding energies and the OH stretch vibrational frequencies calculated for the various isomers are summarized in Table 5 and Table 6. As seen from Figure 12, the Ar atoms can bind to the Mg^+ ion as well as to the OH groups as expected from the

previous discussion. In isomers with Ar atoms bound to the Mg^+ ion, the Ar atoms are found to be located along the side of Mg^+O axis. As we and others have discussed previously,[103-107,145] the binding of a water ligand, with the negative end of the dipole oriented toward the cation, induces a strong polarization of the 3s orbital, producing a lobe of negative charge in the region along the C_2 axis opposite the water monomer. Subsequent ligands, in this case, Ar, avoid this negative charge region and instead bind along the side of the first ligand. This backside screening of the metal ion causes bent structures to form for Mg^+-L_2 complexes and trigonal pyramid structures to form for Mg^+-L_3 complexes. This effect limits the number of argon atoms that can bind at the Mg^+ ion.

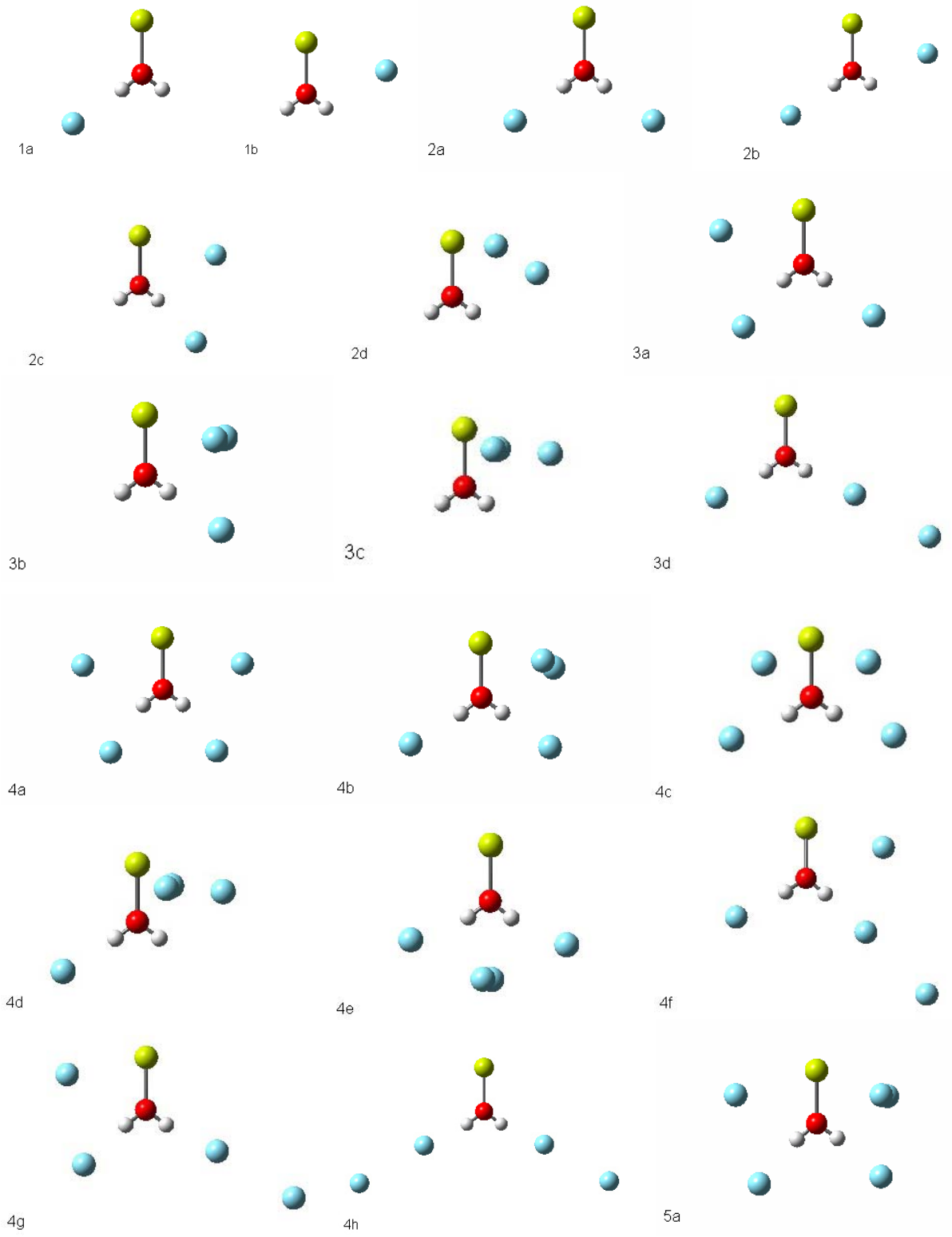

Figure 12. Geometries of the $Mg^{+}(H_2O)Ar_n$, n = 1-5, complexes, optimized using the MP2 procedure.

Table 5. Calculated binding energies (cm^{-1}) and OH stretch frequencies (cm^{-1}) and intensities of the $Mg^+(H_2O)Ar_n$, n = 0-5 clusters.[a]

Isomers	BE w/o ZPE	BE with ZPE	υ_s		υ_a	
			Freq	Int[b]	Freq	Int[b]
H_2O	**-**	**-**	**3646**	**6**	**3766**	**75**
0	**-**	**-**	**3565**	**87**	**3653**	**223**
			3565	88	3653	227
1a	**-770**	**-587**	**3515**	**368**	**3635**	**278**
	-792	-603	3509	383	3631	276
1b	**-682**	**-561**	**3571**	**78**	**3662**	**236**
	n/a	n/a	n/a	n/a	n/a	n/a
2a	**-1505**	**-1169**	**3505**	**313**	**3578**	**648**
	-1548	-1215	3500	319	3571	661
2b	**-1427**	**-1163**	**3522**	**361**	**3639**	**315**
	n/a	n/a	n/a	n/a	n/a	n/a
2c	**-1370**	**-1105**	**3528**	**310**	**3639**	**266**
	-1393	-1130	3523	322	3635	267
2d	**-1171**	**-1013**	**3575**	**78**	**3667**	**227**
	-1173	-1017	3573	78	3664	232
3a	**-2077**	**-1677**	**3515**	**331**	**3588**	**559**
	-2121	-1726	3510	336	3583	577
3b	**-1845**	**-1530**	**3531**	**280**	**3644**	**281**
	-1869	-1554	3526	290	3641	283
3c	**-1586**	**-1396**	**3578**	**76**	**3670**	**218**
	n/a	n/a	n/a	n/a	n/a	n/a
3d	**-1570**	**-1209**	**3504**	**321**	**3576**	**683**
	-1612	-1256	3499	326	3570	696
4a	-2594	-2161	3526	310	3596	440
4b	-2580	-2135	3514	305	3589	606
4c	-2468	-2056	3515	267	3592	632
4d	-2310	-1969	3527	368	3645	285
4e	-2221	-1812	3509	220	3579	557
4f	-2182	-1765	3509	340	3580	604
4g	-2183	-1765	3509	354	3581	596
4h	-1677	-1297	3498	330	3568	729
5a	-3025	-2543	3525	298	3598	490

[a] Results obtained at the MP2 level of theory, with all binding energies being corrected for BSSE by means of the counterpoise procedure. The results indicated in bold are from the all-electron calculations using the aug-cc-pVTZ basis set. The remaining results are from pseudopotential calculations. The harmonic vibrational frequencies obtained from the all-electron and pseudopotential calculations have been scaled by 0.954.

[b] Intensities are in units of KM/mole.

[c] (1b), (2b), and (3c) isomers were found to be a local minimum in the all-electron but not found in the pseudopotential calculations.

Table 6. Ar atom binding energies (cm^{-1})[a] and relative zero-point energies (cm^{-1}) for $Mg^+(H_2O)Ar_n$, n = 1-2, at different levels of theory.

Isomer	MP2/TZ[b]	MP2/QZ[c]	CCSD(T)/TZ //MP2/TZ[d]	CCSD(T)/QZ //MP2/QZ[d]	ΔZPE /TZ[e]	ΔZPE /QZ[e]	Total/ TZ[f]	Total/ QZ[f]
1a	-770	-813	-772	-810	183	175	-589	-634
TS	-682	-728	-713	-750	115	125	-599	-625
1b	-682	-737	-723	-778	121	117	-602	-661
2a	-1505	-1587	-1512	-1583	336	309	-1175	-1275
2b[g]	-1427	-1515	-1466	-1554[h]	264	252	-1202	-1302[h]
2c	-1370	-1465	-1421	-1512	265	256	-1156	-1256
2d	-1171	-1272	-1258	-1359[h]	157	158	-1100	-1201[h]

[a] All binding energies include the counterpoise correction for BSSE.

[b] From MP2/aug-cc-pVTZ optimizations

[c] From MP2/aug-cc-pVQZ optimizations.

[d] The CCSD(T) calculations were carried out at MP2/aug-cc-pVTZ or aug-cc-pVQZ optimized geometries.

[e] $\Delta ZPE = ZPE[Mg^+(H_2O)Ar] - ZPE[Mg^+(H_2O)]$ at MP2/aug-cc-pVTZ or MP2/aug-cc-pVQZ.

[f] E(Total/TZ) = E(CCSD(T)/TZ//MP2/TZ) + E(ΔZPE/TZ), and E(Total/QZ) = E(CCSD(T)/QZ//MP2/QZ) + E(ΔZPE/QZ).

[g] This non-minimum structure has one Ar atom bound near Mg^+ ion and the other bound to a H atom in a *trans*-like arrangement.

[h] Estimated values. E(CCSD(T)/QZ//MP2/QZ) is estimated by E(MP2/QZ) + E(CCSD(T)/TZ//MP2/TZ) – E(MP2/TZ).

The binding energies reported in Table 5 were obtained from MP2 energies and were calculated using

$$\text{B.E.} = E[Mg^+(H_2O)Ar_n] - E[Mg^+(H_2O)] - nE[Ar],$$

where the $Mg^+(H_2O)Ar_n$ energies include the counterpoise correction for basis set superposition error.[158,159] Table 6 reports the results of a more detailed study of the $Mg^+(H_2O)Ar_n$ (n = 1-2) complexes at different levels of theory, while Figure 13 reports the relative energies for the isomers at each cluster size.

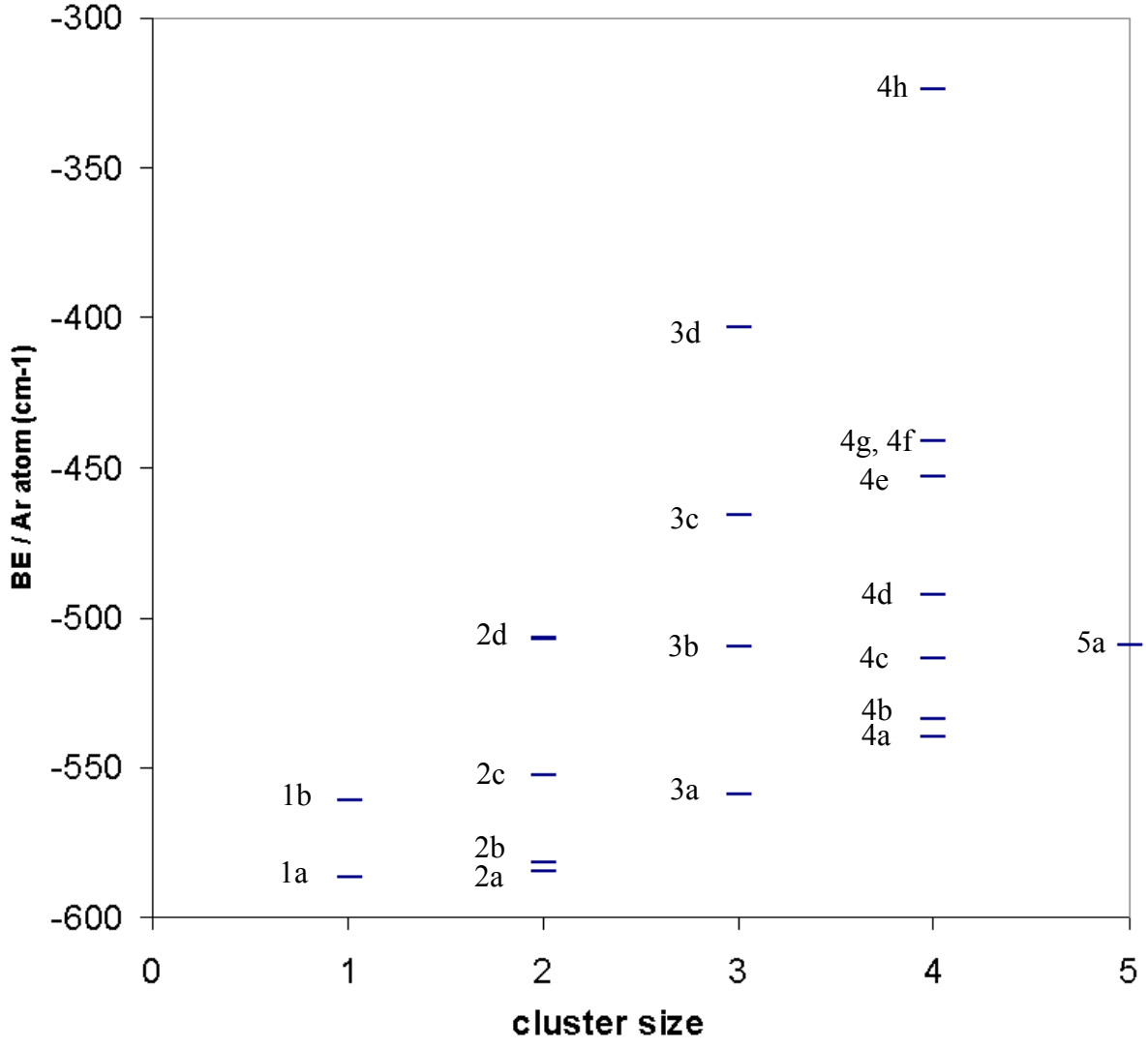

Figure 13. Relative energies of isomeric structures calculated MP2 theory level. These results for the n = 1 and 2 clusters are from all-electron MP2/aug-cc-pVTZ calculations and those for the large clusters are from MP2/PP calculations. Corrections for BBSE and for vibrational ZPE have been applied. The later corrections come from the MP2-level harmonic frequencies scaled described in the text.

In examining the trends in the calculated binding energies, we first consider results of the all-electron calculations on the *n* = 1-3 clusters. At the MP2/aug-cc-pVTZ level two isomers, both with planar structures, were identified for $Mg^+(H_2O)Ar$. One isomer (1a) has the Ar atom

bound to an H atom and the other (1b) has it bound in the vicinity of the Mg^+ ion. The ArMgO angle in (1b) is calculated to be 73.3°. This strong deviation from a linear ArMgO arrangement is due to the polarization of the Mg^+ ion by H_2O, as discussed above. Even though (1b) is referred to as Mg-bound, the Ar atom in this isomer also interacts strongly with one of the protons. The all-electron MP2/aug-cc-pVTZ calculations give Ar-atom binding energies of -770 and -682 cm^{-1} for (1a) and (1b), respectively. Both expansion of the basis set from aug-cc-pVTZ to aug-cc-pVQZ and inclusion of high-order electron correlation effects act so as to preferentially stabilize (1b) with respect to (1a), with the later correction being more important. Vibrational zero-point energy (ZPE) corrections also stabilize (1b) relative to (1a), and when the various corrections are combined, (1b) is predicted to be slightly (~27 cm^{-1}) more stable than (1a).

The transition state for conversion of (1b) to (1a) is predicted to lie energetically less than 1 cm^{-1} above (1b) at the MP2/aug-cc-pVTZ level. However at the CCSD(T)//MP2/aug-cc-pVQZ level the (1a) → (1b) and (1b) → (1a) barriers are calculated to be 60 and 28 cm^{-1}, respectively. Finally, with the inclusion of vibrational ZPE's, calculated using MP2/aug-cc-pVQZ level harmonic frequencies, the barrier for isomerization of (1a) to (1b) is calculated to be 9 cm^{-1} and that for the reverse process is calculated to be 36 cm^{-1}. The harmonic frequencies of the bending mode corresponding most closely with motion along the isomerization pathway are calculated at MP2/aug-cc-pVQZ level to be 33 and 42 cm^{-1} for (1a) and (1b), respectively. Actually, in constructing the adiabatic potentials for (1a)/(1b) isomerization, the ZPE correction should exclude that associated with the isomerization coordinate. In that case the barriers for (1a)→(1b) and (1b)→(1a) isomerization are calculated to be 25 and 57 cm^{-1} respectively, which leads us to conclude that it should be possible to observe both (1a) and (1b) experimentally.

Four isomers were characterized for the $Mg^+(H_2O)Ar_2$ cluster. Three of these, (2a), (2b) and (2c) have planar structures. Isomer (2a) has one Ar atom bound to each H atom. Isomers (2b) and (2c) have one Ar atom bound to an H atom and the other Ar atom bound near the Mg^+ ion in *trans*- and *cis*-like arrangements, respectively. Isomer (2d) can be viewed as arising from an Ar dimer bound to the side of the $Mg^+(H_2O)$ complex. In this complex, one Ar atom lies close to the approximate $Mg^+(H_2O)$ plane and the other is located out-of-plane. (2a) is calculated at the MP2/aug-cc-pVTZ level to be 78, 135 and 334 cm^{-1} more stable than (2b), (2c) and (2d), respectively. Attempts to locate a local minimum with the two Ar atoms bound on opposite sides of the Mg^+ ion failed at MP2/aug-cc-pVTZ level, *i.e.*, the optimization collapsed back to (2a). The net Ar-atom binding energies of (2a), (2b), (2c), and (2d), after allowing for basis set expansion, high-order correlation effects, and ZPE are calculated to be -1275, -1302, -1256, and -1201 cm^{-1}, respectively. The net Ar-atom binding energies in these clusters are approximately twice as large in magnitude as those for the single Ar atom of (1a) and (1b).

Four isomers were identified for $Mg^+(H_2O)Ar_3$. At the MP2/aug-cc-pVTZ level the most stable of these, (3a), has an Ar atom bound to each H atom, and the third Ar atom bound near the Mg^+ ion. The three higher-energy isomers, (3b), (3c) and (3d), are calculated at the MP2/aug-cc-pVTZ level to be about 232, 491 and 507 cm^{-1} less stable than (3a), respectively. (3b) has an Ar atom bound to one of the H atoms and an Ar dimer bound near the Mg^+ atom, with one of the Ar atoms of the dimer located above and the other below the $Mg^+(H_2O)$ plane. (3c) can be viewed as being derived from an Ar trimer bound to the side of the $Mg^+(H_2O)$ complex with the two Ar atoms closest to Mg^+ being located above and below the plane of the $Mg^+(H_2O)$ species. The high-energy isomer (3d) has an Ar atom bound to one H atom and an argon dimer bound the other H atom in an approximately linear arrangement. Attempts to optimize a planar

$Mg^+(H_2O)Ar_3$ isomer with one Ar atom bound to an H atom and the remaining two Ar atoms bound to the Mg^+ ion on opposite sides of the MgO bond proved unsuccessful as such structures were unstable with respect to collapse back to (3a).

The pseudopotential calculations give Ar-atom binding energies and vibrational frequencies for the $Mg^+(H_2O)Ar_n$, n = 1-3, clusters very close to the corresponding all-electron results. One difference is that the pseudopotential calculations fail to give a minima for isomers (1b) and (2b). This is not surprising since the all-electron MP2/aug-cc-pVTZ calculations gave a barrier of less than 1 cm^{-1} for conversion of (1b) to (1a). The barrier for isomerization of (2b)→(2a) was not calculated at the MP2/aug-cc-pVTZ level, but is probably very low. It is anticipated that with the use of a more flexible basis set and inclusion of high-order correlation effects, the pseudopotential calculations could not locate the (1b) and (2b) minima.

Eight isomers were identified for $Mg^+(H_2O)Ar_4$. All of these, with the exception of (4d), have Ar atoms bound to each H atom. The three most stable isomers, (4a), (4b), and (4c), all have one Ar atom bound to each H atom. In the most stable of these, (4a), the remaining Ar atoms are bound to Mg^+ on either side of the Mg^+O bond. The second most stable isomer of $Mg^+(H_2O)Ar_4$, (4b), has the other two Ar atoms bound as a dimer to the Mg^+ ion with one Ar above and one Ar below the $Mg^+(H_2O)$ plane. Isomer (4c) has an Ar dimer bound above the plane of the $Mg^+(H_2O)$ in the vicinity of the Mg^+. (4d) has an Ar trimer bound along the Mg^+O axis, with the fourth Ar atom being bound on the remote H atom. Isomer (4e) has one Ar atom bound to each H atom and an Ar dimer bound between two OH groups and perpendicular to the plane of $Mg^+(H_2O)$. The sixth and seventh isomers of $Mg^+(H_2O)Ar_4$ lie appreciably higher in energy and have an Ar atom bound to one H atom, an Ar dimer bound to the other H atom, and a single Ar atom bound to Mg^+. The least stable isomer identified for $Mg^+(H_2O)Ar_4$, (4h), has an

Ar dimer bound to each H atom. The only isomer characterized for $Mg^+(H_2O)Ar_5$ has an Ar atom bound to each H atom, and three Ar atoms bound near the Mg^+ ion, with two of these being located out of the $Mg^+(H_2O)$ plane.

3.5.3. Calculated vibrational spectra

In order to facilitate comparison between theory and experiment, the calculated OH stretch vibrational frequencies have been scaled by a factor of 0.954, chosen so as to bring the calculated harmonic frequencies at MP2/aug-cc-pVTZ of the OH stretch modes of water monomer into close agreement with the experimentally determined frequencies. The scaled frequencies are summarized in Table 5.

In the ensuing discussion, the scaled calculated frequencies are employed. The OH stretch frequencies of the $Mg^+(H_2O)$ complex are calculated to be 3565 (symmetric stretch) and 3653 cm^{-1} (asymmetric stretch), which are shifted to the red by 92 and 103 cm^{-1}, respectively from the measured frequencies of the OH stretch vibrations of the isolated water molecule.[160] As for the isolated water molecule, the asymmetric OH stretch vibration has the higher frequency. These red shifts are due to charge transfer from the water toward the metal.[134,135] Unfortunately, the infrared spectrum for the un-tagged $Mg^+(H_2O)$ complex has not been measured, so comparison of theory with experiment is not possible for this species.

For isomer (1a) of $Mg^+(H_2O)Ar$, the calculations predict the symmetric and asymmetric OH stretch vibrations to have additional red shifts of 50 and 18 cm^{-1}, respectively, compared to the corresponding vibrations of $Mg^+(H_2O)$. The interaction with the Ar atom causes some localization of the vibrations, making the use of the "symmetric" and "asymmetric" labels only

approximate. The more red-shifted transition is that associated with the OH stretch vibration more localized "on" the OH to which the Ar atom is attached. The binding of the Ar atom to OH causes a small increase in the length of the associated OH bond (calculated increase of 0.0036 Å), and this, in turn, is accompanied by a red shift of the associated OH stretch vibration. In contrast, for isomer (1b) of $Mg^+(H_2O)Ar$, in which the Ar atom is located near the Mg^+ ion, the calculated frequencies of the OH stretch vibrations are weakly (6-9 cm^{-1}) *blue* shifted relative to the corresponding frequencies of $Mg^+(H_2O)$. The inductive effect that causes a red shift in the OH stretch vibrations of $Mg^+(H_2O)$ relative to those of a free water molecule is partially mediated when an Ar atom is bound to the ion, thus slightly reducing the red-shifts.

The symmetric and asymmetric OH stretch frequencies of isomer (2a) of $Mg^+(H_2O)Ar_2$, with Ar atoms bound to each H atom, are predicted to be red shifted by 60 and 75 cm^{-1}, respectively, compared the corresponding vibrations of $Mg^+(H_2O)$. The calculated frequencies of OH stretch vibrations of the "*trans*" and "*cis*" isomers (2b) and (2c) are less red shifted than those of (2a) and are, in fact, close to those of (1a), which has only one Ar atom bound to OH. The symmetric and asymmetric OH stretch frequencies of isomer (2d), with two Ar atoms bound to Mg^+ ion, are predicted to be blue shifted relative to the corresponding vibrations of $Mg^+(H_2O)$ by 10 and 14 cm^{-1}, respectively.

The calculated OH stretch frequencies of isomer (3a) of $Mg^+(H_2O)Ar_3$ are close to those of (2a), again consistent with the observation that an Ar atom bound near the Mg^+ ion has little effect on frequencies of the OH stretch vibrations. Similarly, the calculated frequencies of the OH stretch vibrations of (3b) are close to those of (2c), and the calculated frequencies of (3c) are close to those of (2d). Finally, isomer (3d) has OH stretch frequencies nearly identical to those of

(2a), demonstrating that the binding of an Ar dimer to one of the OH groups (as in 3d) has nearly the same impact on the OH stretch frequencies as does the binding of an Ar atom.

The above discussion of the influence of the Ar atoms on the frequencies of the OH stretch vibrations of $Mg^+(H_2O)Ar_n$, n = 1-3, clusters was based on the results of the all-electron calculations. For these species nearly the same vibrational frequencies are obtained from the pseudopotential as from the all-electron calculations. Thus we can confidently adopt the pseudopotential procedure for discussing the trends in the vibrational frequencies for the large clusters.

The calculated OH stretch frequencies of the (4a) isomer of $Mg^+(H_2O)Ar_4$ with an Ar atom bound to each OH group and two Ar atoms bound to the Mg^+ ion fall slightly to the blue to those calculated for (3a), whereas the calculated frequencies of (4b) and (4c) are essentially identical to those of (3a). Isomers (4e), (4f), and (4g) are all predicted to have similar OH stretch vibrations, red shifted by about 17 $cm^{-1}$with respect to those of (4a), whereas (4h), with an Ar dimer bound to each H atom, has the most red shifted OH stretch vibrations of the various $Mg^+(H_2O)Ar_4$ isomers. However, the last four isomers of $Mg^+(H_2O)Ar_4$ are calculated to be about 400 cm^{-1} less stable than (4a) and are unlikely to be very important under the conditions of the experiments.

The only isomer characterized for $Mg^+(H_2O)Ar_5$, (5a), has three Ar atoms bound in the vicinity of the Mg^+ ion, and one Ar atom bound to each OH. (5a) is calculated to have nearly the same OH stretch vibrational frequencies as (4a) which also has one Ar atom bound to each H atom. The extra Ar atom bound to Mg^+ in (5a) has only a minor effect on the OH stretch frequencies. The calculated OH stretch frequencies are summarized in Figure 14, from which

the large red shifts associated with binding of Ar atoms on H atoms and the small blue shifts resulting from the binding of Ar atoms near Mg^+ are really apparent.

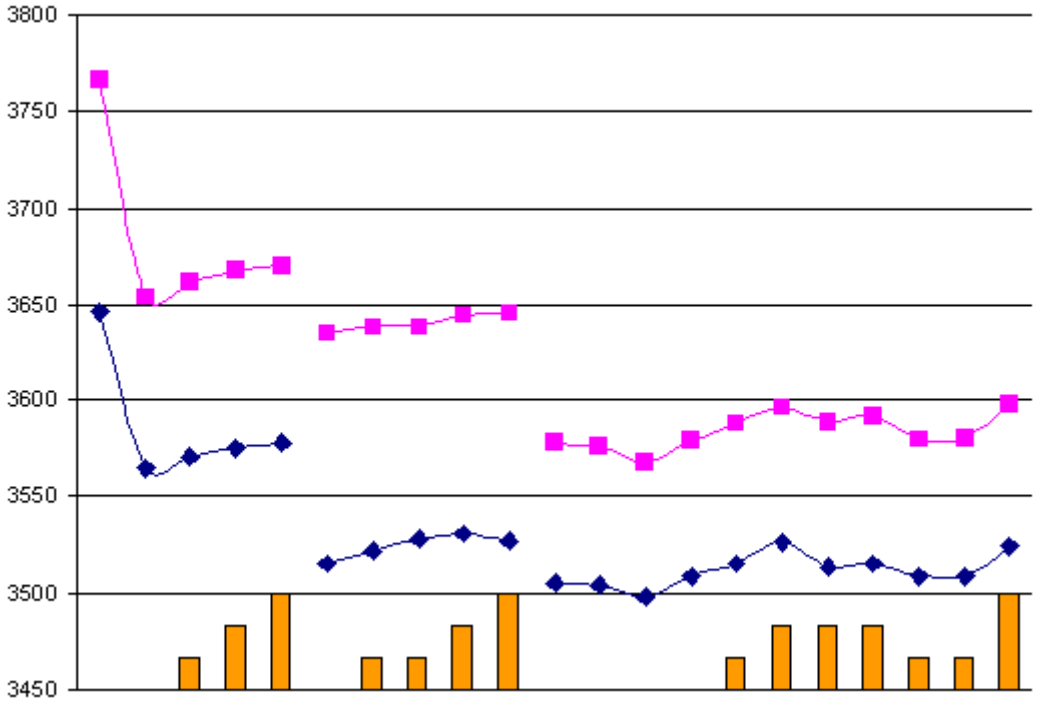

Figure 14: Summary of the calculated OH stretch frequencies of the $Mg^+(H_2O)Ar_n$ clusters. The left axis denotes the calculated OH stretch frequencies (cm^{-1}). The right axis denotes the number of Ar atoms bound to Mg^+ ion.

3.5.4. Comparison between calculated and measured vibrational spectra

3.5.4.1. $Mg^+(H_2O)Ar$

Figure 15 compares the measured vibrational spectrum of $Mg^+(H_2O)Ar$ to the calculated spectra for the (1a) and (1b) isomers. The experimental spectrum has strong vibrational transitions at 3579 and 3650 cm^{-1}, with weaker transitions at 3531, 3624 and 3739 cm^{-1}. Weak bands in the

3700-3800 cm^{-1} region are present in the vibrational spectra of many $M^+(H_2O)Ar_n$ complexes and are due to combination bands involving Ar vibrations.[134,135] Thus we conclude that the 3739 cm^{-1} feature in the spectrum of $Mg^+(H_2O)Ar$ is a combination band involving OH stretch and either Ar-H or Ar-Mg^+ stretch. In this work we are primarily interested in the assignments of the fundamentals, and will not further consider weak structure due to combination bands.

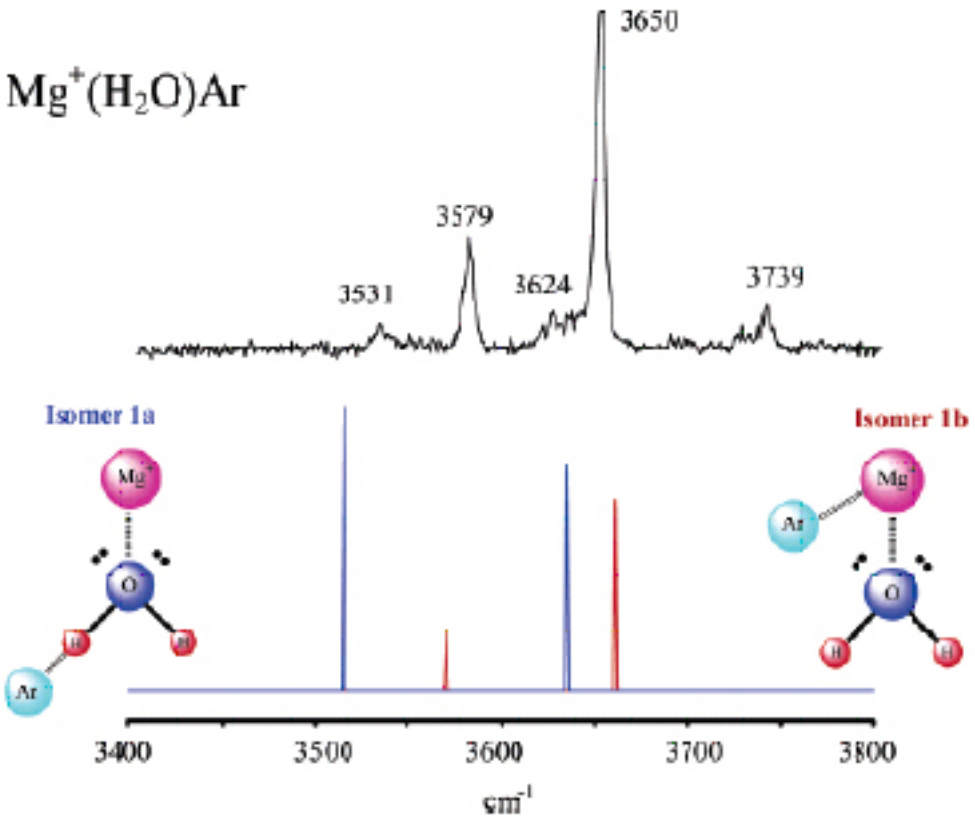

Figure 15. Comparison of calculated and measured vibrational spectra of the $Mg^+(H_2O)Ar$. The calculated spectrum of isomer (1a) is shown in blue, while that for (1b) is shown in red.

The relative intensities of the observed strong and weak transitions of $Mg^+(H_2O)Ar$ depends on the experimental conditions, as shown in Figure 10, indicating the presence of two isomers. The spectrum shown in Figure 15 is the one measured under the coldest conditions,

which is assumed to favor the most stable isomer. The calculated OH stretch frequencies of isomer (1a) (indicated by blue peaks) correspond closely to the positions of the two weak peaks in the experimental spectrum, and the calculated OH stretch frequencies of isomer (1b) (indicated in red) to the two intense peaks. Although (1a) is calculated to be 88 cm^{-1} more stable than (1b) at the MP2/aug-cc-pVTZ level of theory, expansion of the basis set (from aug-cc-pVTZ to aug-cc-pVQZ), inclusion of high-order correlation effects (at the CCSD(T) level), and correction for vibrational zero-point energy (calculated at the MP2/aug-cc-pVQZ level) act so as to stabilize (1b) relative to (1a), and, as noted above, combination of all these corrections leads to the conclusion that (1b) is about 27 cm^{-1} more stable than (1a). This conclusion is consistent with the experiment, as the two strongest peaks in the spectrum match well the predicted bands for (1b) in both position and relative intensity.

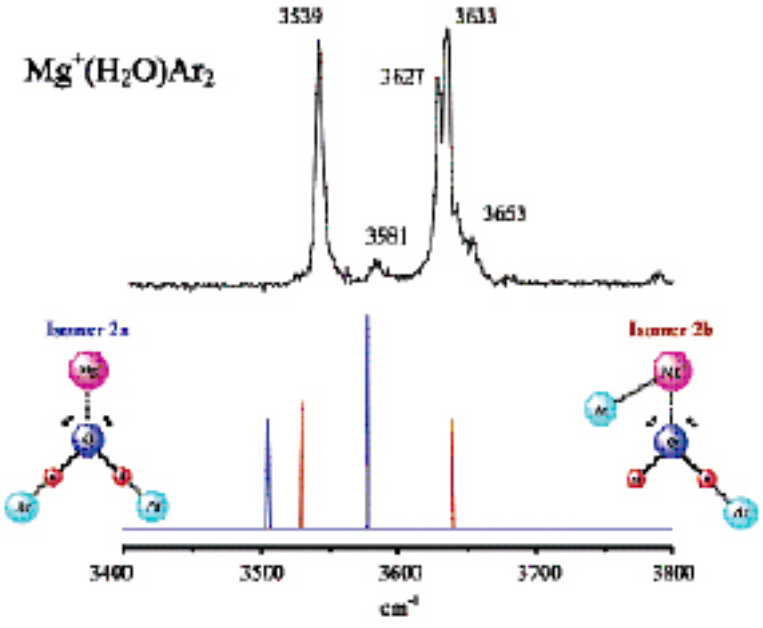

Figure 16. Comparison of calculated and measured vibrational spectra of the $Mg^{+}(H_2O)Ar_2$. The calculated spectrum of isomer (2a) is shown in blue, while that for (2b) is shown in red.

3.5.4.2. $Mg^+(H_2O)Ar_2$

The experimental and calculated spectra of $Mg^+(H_2O)Ar_2$ are compared in Figure 16. The measured spectrum has an intense peak at 3539 cm^{-1}, an intense "doublet" at 3627 and 3633 cm^{-1}, and weak features at 3581 and 3651 cm^{-1}. The intense bands fall very close to the frequencies predicted for isomers (2b) and (2c) (although, only a single line is predicted in the vicinity of the intense doublet). The doublet observed near 2630 cm^{-1}, may indicate that both the *cis* and *trans* isomers are contributing to the experimental spectrum.

The weak band observed at 3581 cm^{-1} is close to the position predicted for the higher frequency vibration of the (2a) isomer, and it is possible that the weak shoulder observed near 3540 cm^{-1} in the experimental spectrum corresponds to the lower frequency OH stretch vibration of (2a), which is calculated to occur at 3505 cm^{-1}. However, we are then left with the problem of an unassociated shoulder at 3653 cm^{-1}. This feature plus part of the intensity in the 3581 cm^{-1} band could derive from an isomer with Ar atoms bound to Mg^+ on either side of the MgO axis. Although such a species was not found to be a minimum at the MP2 level, such a species could be a local minimum at the CCSD(T) level, particularly after inclusion of vibrational ZPE corrections. This species would be expected to have OH stretch frequencies close to those of (1b), which indeed fall close to the weak bands observed near 3581 and 3651 cm^{-1}.

3.5.4.3. $Mg^+(H_2O)Ar_3$

Figure 17 compares the experimental and calculated spectra of $Mg^+(H_2O)Ar_3$. The experimental spectrum has intense peaks at 3531, 3547, 3592 and 3637 cm^{-1}. The frequencies of the two more intense peaks are close those calculated for isomer (3b), and the frequencies of the two less

intense peaks correspond closely to those calculated for isomer (3a). Although the MP2/aug-cc-pVTZ calculations predict isomer (3a) to be about 232 cm^{-1} more stable than (3b), upon inclusion of vibrational ZPE, the energy difference is calculated to be only 147 cm^{-1}. Based on results for $Mg^+(H_2O)Ar$ and $Mg^+(H_2O)Ar_2$, it is anticipated that calculations using the more flexible aug-cc-pVQZ basis set and including high-order correlation effects would predict (3b) to be slightly more stable than (3a), consistent with slightly more intense peaks associated with (3b) than (3a) in the observed spectrum. Isomers (3c) and (3d) are calculated to be 281 and 465 cm^{-1} less stable respectively than (3a) at the MP2/aug-cc-pVTZ level with ZPE corrections, and it is unlikely that either of these has appreciable population under the experimental conditions.

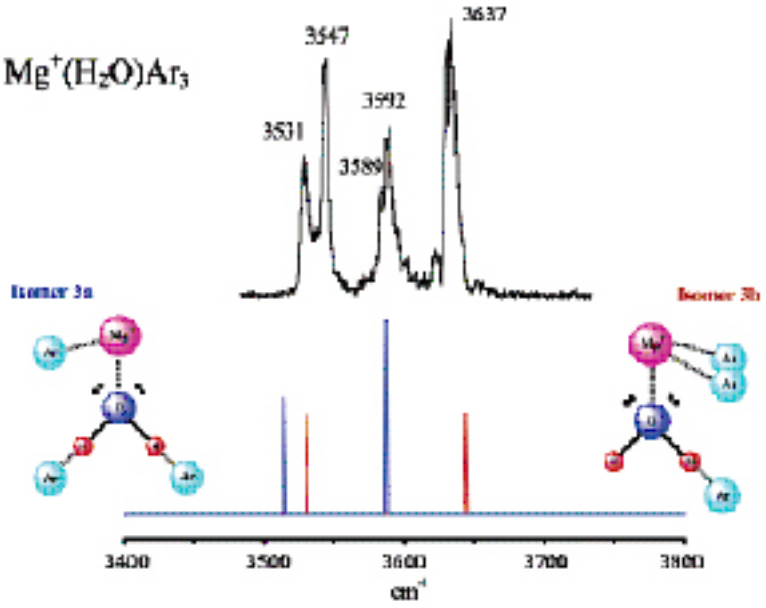

Figure 17. The comparison of the experimental spectrum for the $Mg^+(H_2O)Ar_3$ complex. The calculated spectrum of isomer (3a) is shown in blue, while (3b) is shown in red.

3.5.4.4. $Mg^+(H_2O)Ar_4$

Figure 18 compares the calculated and experimental vibrational spectra of $Mg^+(H_2O)Ar_4$. The experimental spectrum displays intense peaks near 3538 and 3596 cm^{-1}, together with weak features near 3550, 3580, and 3637 cm^{-1}. The frequencies associated with the two observed intense peaks are close to those calculated for the OH stretch vibrations of isomers (4a) and (4b), with the calculated frequencies being 3526 and 3596 cm^{-1} for (4a) and 3514 and 3589 cm^{-1} for (4b). The frequency differences between (4a) and (4b) are great enough, that were both highly populated, the experimental spectra should display two pairs of intense doublets. Since the doublets are not observed, we conclude that only one of these isomers is present in high population in the experiments. The MP2/pseudopotential calculations with the inclusion of ZPE corrections predict (4a) to be 26 cm^{-1} more stable than (4b). However, the relative stability of the two isomers could be reversed upon adoption of a more flexible basis set and inclusion of high-order correlation effects. Support for this possibility is provided by the experimental spectrum since each intense line is accompanied by a weak shoulder to the blue. Thus we favor the interpretation that the two intense lines are due to (4b), with the weak shoulders to the blue being due to (4a). The OH stretch frequencies calculated for isomer (4c) are very close to those of isomer (4b), and it is possible that this isomer is also present experimentally. The calculated OH stretch frequencies of (4d) match well with the weak bands observed at 3550 and 3637 cm^{-1}. The higher frequency OH stretch bands of (4e), (4f), and (4g) isomers are calculated to fall between 3579 and 3581 cm^{-1}, close to the observed weak band at 3580 cm^{-1}. However, the lower frequency OH stretch band of each of these isomers is predicted to fall at 3509 cm^{-1} and there is no evidence of a low energy shoulder on the observed intense line at 3538 cm^{-1}. The fact that the

3550 and 3637 bands fall very close to the positions of the bands seen for the (3b) isomer of $Mg^+(H_2O)Ar_3$, supports the interpretation that (4d) is be present at low population.

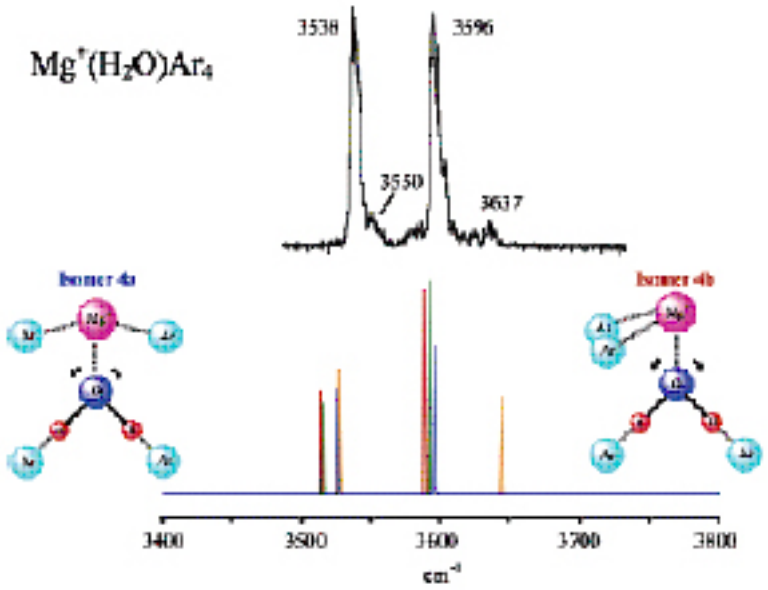

Figure 18. The comparison of the experimental spectrum for the $Mg^+(H_2O)Ar_4$ complex. The calculated spectrum of isomer (4a) is shown in blue, while that for (4b) is shown in red. Predicted spectra for (4c) and (4d) are shown in green and orange, respectively.

Theory and experiment agree that there are basically three isomer types for the $n \leq 4$ $Mg^+(H_2O)Ar_n$ clusters. Isomers with no Ar atoms bound to OH are observed for the n = 1 and 2 clusters. These species have OH frequencies that are strongly red shifted from those in the isolated water molecule. Isomers that have one argon atom bound to OH are observed for each of the n = 1-4 clusters. These are of minor importance for the n = 1 and 4 clusters and of major importance in the n = 2 and 3 clusters. The red shifts of the OH stretch vibrations of these isomers are greater than for those isomers with no Ar atoms bound to OH. The third type of isomer has Ar atoms bound to each OH group. These isomers experience significant additional red shift occurs compared to those species with only one Ar atom on OH. This type of isomer is

apparently present only as a minority species for the n = 2 cluster. However, for the n =3 cluster this isomer (3a) with Ar atoms bound to each OH group has roughly the same population as the isomer with only one Ar on OH (3b), and in the n ≥ 4 clusters, isomers with Ar atoms bound to both OH groups dominate. The binding of additional argon atoms on the metal ion has a relatively minor effect on the OH frequencies, regardless of the exact position.

It is encouraging that the electronic structure calculations identify the major isomers detected in the experiments and successfully account for the major peaks in the measured vibrational spectra. However, as the more extensive calculations on the smaller clusters illustrate, it is a major challenge to establish the correct energy orderings of the isomers. Not only are very large basis sets and inclusion of high-order correlation effects, *e.g.*, at the CCSD(T) level, required, but vibrational ZPE corrections are also important. Given the weak binding of the Ar atoms to the $Mg^+(H_2O)$ core, the ZPE energies should clearly be calculated allowing for vibrational anharmonicity, a daunting task when using *ab initio* energies.

3.5.5. Larger clusters

Figure 19 shows the IR spectra measured for the larger $Mg^+(H_2O)Ar_n$ clusters (n = 5-8). All of these spectra consist of only two vibrational bands (although the higher frequency band is split into a doublet in the n = 7 cluster) which shift to the blue with increasing number of Ar atoms. At n = 5, the two bands occur at 3543 and 3604 cm^{-1}, slightly to the blue of the positions of the corresponding bands in the spectra of the n = 4 complex at 3538 and 3596 cm^{-1}. The only isomer of $Mg^+(H_2O)Ar_5$ investigated theoretically, (5a), has vibrational bands predicted at 3525 and

3598 cm^{-1}, very close to the observed bands. (5a) has three Ar atoms bound to the metal ion and one bound to each OH site of the water molecule.

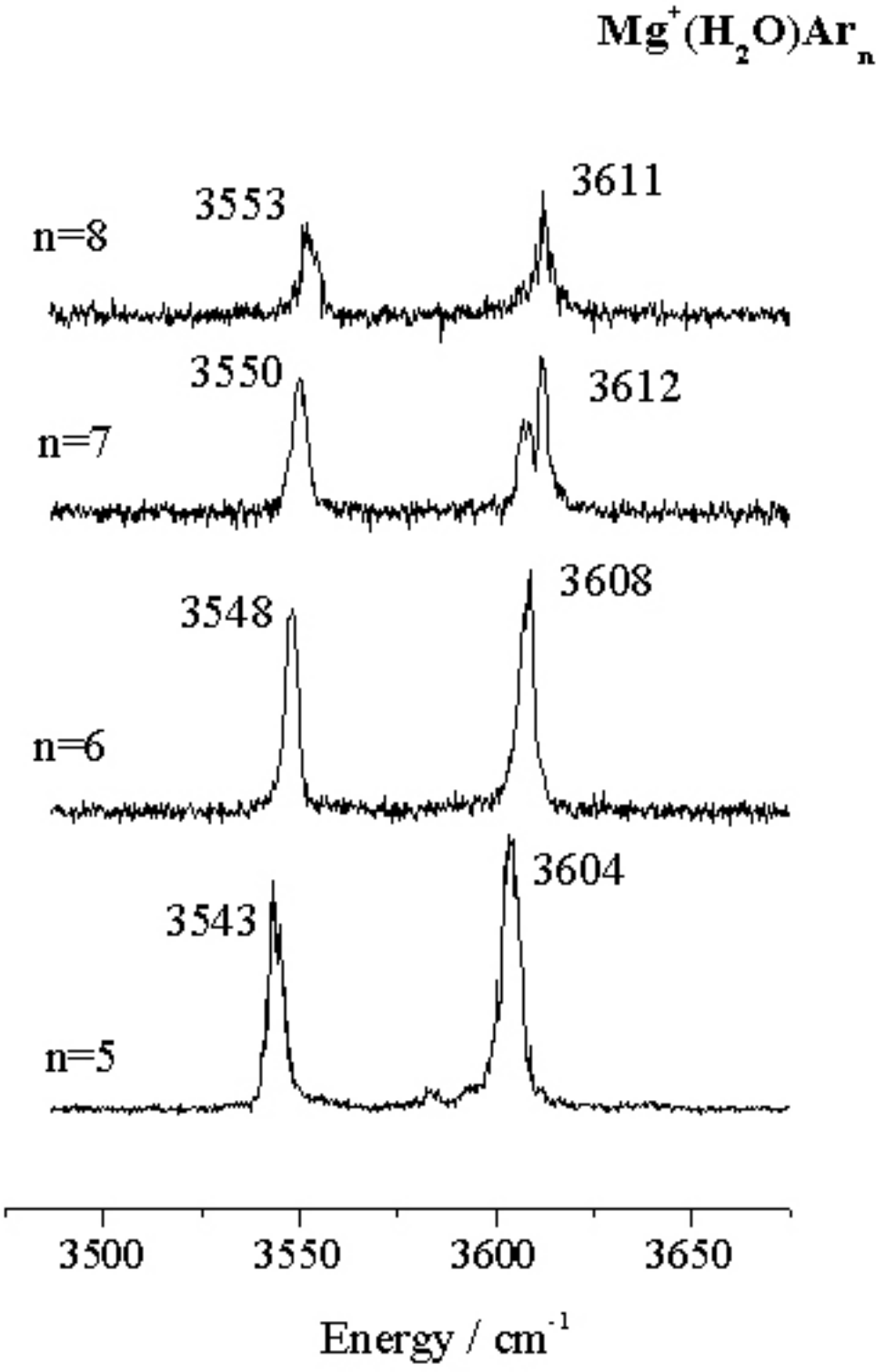

Figure 19. The variation of the spectra for the $Mg^+(H_2O)Ar_n$ complexes for n=5-8.

The similarity of the spectra for the $n \geq 4$ clusters, implies that all of these species has one Ar atom bound to each OH groups, with the remaining Ar atoms bound in the vicinity of the Mg^+ ion. The blue shifts in going from $n = 6$ to 7 and from 7 to 8 are smaller than those between $n = 4$ and 5 and between 5 and 6. This suggests that all Ar atoms in the vicinity of the Mg^+ ion are directly bound to the ion in the $n = 4$, 5, and 6 clusters, but that the additional Ar atoms in the $n = 7$ and 8 clusters are bound in a second solvent shell as would occur if they were bound as Ar_3 trimers as in (3c) and (4d). Johnson and coworkers have reported the observation of an icosahedral shell closing when 12 argon atoms enclose the $Cl^-(H_2O)$ core ion.

3.6. CONCLUSIONS

$Mg^+(H_2O)Ar_n$ complexes have been studied in detail with infrared photodissociation spectroscopy and *ab initio* electronic structure calculations. Both the vibrational predissociation spectra and the calculations indicate that there are multiple isomers differing in the attachment sites of the Ar atoms, for the $n = 1$-4 clusters. The binding energies of an Ar atom in the vicinity of the Mg^+ ion and attached to an OH group of the water molecule are very similar. The binding of Mg^+ to water leads to a red shift of the OH stretch vibrationas as a result of the ligand-metal charge transfer similar to that seen previously for other cation-water complexes. The binding of the argon atoms leads to additional shifts in the OH stretch vibrational bands. Specifically, attachment of an Ar atom to an OH site leads to a sizable red shift, while attachment of Ar atoms to the Mg^+ ion, leads to small blue shifts. The spectra are very similar in appearance over the $n =$

4 to 8 size range, consistent with these larger clusters being dominated by isomers with one Ar atom bound to each OH site, and with the remaining atoms bound in the vicinity of the Mg^+.

The electronic structure calculations correctly identify the main types of isomers present and account in a near quantitative manner for the trend in the vibrational frequencies. However, prediction of the relative energetics of the isomers is a challenging task, even for the smallest clusters. For the $Mg^+(H_2O)Ar$ and $Mg^+(H_2O)Ar_2$ species, it was shown that it is necessary to adopt large basis sets, *e.g.*, aug-cc-pVQZ, to include electron correlation effects to high order, and to include corrections for vibrational ZPE, to correctly identify the more stable isomers. The fact that the spectra calculated for various isomers of the $Mg^+(H_2O)Ar_n$ clusters successfully accounts for the features in the measured spectra indicates that the clusters produced experimentally must be quite cold (T is about $\leq$ 50K).

Rare-gas tagging is essential for the measurement of infrared photodissociation spectroscopy of species such as $Mg^+(H_2O)$ and, as a result, it is important to understand the influence of resulting isomers on the spectroscopy. It would be highly useful to have accurate model potentials for exploring the potential energy landscapes of such clusters. It is hoped that the present study will motivate the development of reliable model potentials for examining Ar-atom binding to $Mg^+(H_2O)$ and other metal ion/water cluster complexes.

3.7. ACKNOWLEDGEMENTS

We gratefully acknowledge support for this work from National Science Foundation (Duncan grant no. CHE-0244143 and Jordan grant no. CHE-0078528).

4. THEORETICAL STUDY OF INFRARED PHOTODISSOCIATION SPECTROSCOPY OF $Fe^+(H_2O)Ar_{0-2}$ COMPLEXES

4.1. ABSTRACT

Recently Duncan and coworkers have measured the vibrational spectra of the $Fe^+(H_2O)Ar_2$ complexes using Ar atom predissociation spectroscopy. In the present work, the complete active space self-consistent field (CASSCF)[161] and the unrestricted open-shell Møller-Plesset perturbation theory (UMP2) electronic structure methods are used to characterize the $Fe^+(H_2O)Ar_n$, $n = 0$-2, complexes.

4.2. INTRODUCTION

The solvation of metal cations by water molecules is an important subject throughout chemistry and biology, and has been studied in the condensed phase for several decades.[162] Recently, gas phase experiments for studying these complexes have become available.[79,80] The binding energies between water and metal ions and other ligands have been measured by means of collision-induced dissociation experiments,[82,86,89,90,163-165] and the structures and energetics of these systems have been calculated with various quantum chemical methods.[166-169] Lessen *et al.* measured the electronic photodissociation spectrum of $V^+(H_2O)$.[112] Faherty *et al.* investigated doubly charged $Co^{2+}(H_2O)$ complexes with a similar method.[120] Walters and Duncan have measured the IR photodissciation spectrum of $V^+(H_2O)$ and $Fe^+(H_2O)_{1,2}$.[134,135]

Transition-metal-related systems are especially challenging theoretically due to the partial occupation of the 3d atomic orbital of the transition metal atoms. Multi-configurational character in the resulting electronic state can cause single reference based methods such as HF, CI, and DFT to be inappropriate. Complete-active-space self-consistent-field (CASSCF) or comparable multi-reference methods have to be used in order to obtain proper electronic wavefunctions in such case.

4.3. METHODOLOGY

In this work CASSCF method was applied to establish the electronic ground state of $Fe^+(H_2O)Ar_m$, m = 0-2. The aug-cc-pVTZ basis set was used for the H_2O molecule and the Ar atoms,[70,155] and the triple-ζ quality TZVP+G(3df,2p) basis set was used for the transition metal atom. The latter basis set, taken from Schäfer *et al.*,[170] was supplemented with a diffuse *s* function (with an exponent 0.33 times that of the most diffuse *s* function on the original basis set), two sets of *p* functions optimized by Wachters[171] for the excited state, one set of diffuse *d* function (optimized by Hay),[172] and three sets of uncontracted *f* functions, including both tight and diffuse exponents, as recommended by Raghavachari and Trucks.[173]

In this work the possible initial guess for the electronic configurations of $Fe^+(H_2O)Ar_{0-2}$ were determined by considering the various electron occupations in the 3d and 4s orbitals of Fe^+. Only one electronic configuration was calculated for all sextet states and $^4A_1$ state. Two configurations were considered for $^4B_1$, $^4B_2$, and $^4A_2$ states represented by the unpaired electron occupation in the parentheses, *i.e.* $^4B_1(a_1\ b_2\ a_2)$, $^4B_1(a_1\ a_1\ b_1)$, $^4B_2(a_1\ b_1\ a_2)$, $^4B_2(a_1\ a_1\ b_2)$, $^4A_2(a_1\ a_1\ a_2)$, and $^4A_2(a_1\ b_1\ b_2)$.

Four active spaces, designated (7, 6), (7, 9), (13, 9), and (13, 12), were applied to $Fe^+(H_2O)$. The first number in the parentheses represents the number of electrons and the second number denotes the number of orbitals in the active space. The (7, 6) CASSCF calculations include the 3d and 4s orbitals of Fe^+ ion in the active space, while the (7, 9) calculations include 3d, 4s, and 4p orbitals of Fe^+ ion. The (13, 9) and (13, 12) CASSCF calculations include 2p orbitals of water in addition to the active orbitals in the (7, 6) and (7, 9) calculations, respectively. Three different active spaces, (7, 6), (13, 12), and (19, 15), were used for the CASSCF calculations of $Fe^+(H_2O)Ar$. The first two active spaces were the same as those employed for $Fe^+(H_2O)$, whereas the (19, 15) active space includes the 3p orbitals of the argon atom as well. Only the (7, 6) active space was used for $Fe^+(H_2O)Ar_2$.

The CASSCF optimized geometries and electronic configurations were used as initial guesses for UMP2 calculations of the geometries and harmonic vibrational frequencies. Ideally, the CASMP2 procedure[174] would have been used to calculate the frequencies. However, due to the lack of analytical first and second derivatives with this approach, its use in frequency calculations is not feasible. It was for this reason that the UMP2 calculations were carried out. The UMP2 results should be reliable in those cases that the wavefunction is dominated by a single configuration. Density functional theory calculations using B3LYP functional[175] were also carried out to compare with the MP2 results. The calculated frequencies are scaled by 0.954 and 0.963 for UMP2 and DFT calculations, respectively. The scaling factors are chosen by the mean of the scale factors needed to bring the calculated frequencies of the symmetric and asymmetric stretch frequencies of H_2O into agreement with experiment.

The CASSCF and CASMP2 calculations were carried out with using MOLPRO.[176] The UMP2 and DFT calculations were carried out using Gaussian 03. [154]

4.4. RESULTS

The results of the CASSCF calculations are very sensitive to the construction of the active space. Based on the molecular orbitals of H_2O, Fe^+, and $Fe^+(H_2O)$, shown in Figure 20-Figure **21**, it is expected that it may be necessary to include the 3d, 4s, and 4p orbitals of Fe atom and the 2p orbitals of H_2O into the active space in order to accuarately describe the low energy states of $Fe^+(H_2O)$. Three smaller active spaces were also considered for comparison.

The molecular orbitals of $Fe^+(H_2O)Ar$ are shown in Figure 23. The 3p orbitals of Ar should be included in the active space because they overlap energetically with the 2p orbitals of water and the 3d orbitals of Fe^+. However, the active space for the $Fe^+(H_2O)Ar_2$ species was constrained to the 3d, 4s orbitals of Fe^+ because CASSCF calculations including the 3p orbitals on two Ar atoms would have been prohitive.

The optimized structures of $Fe^+(H_2O)Ar_n$, n = 0-2, at UMP2 level are shown in Figure 22.

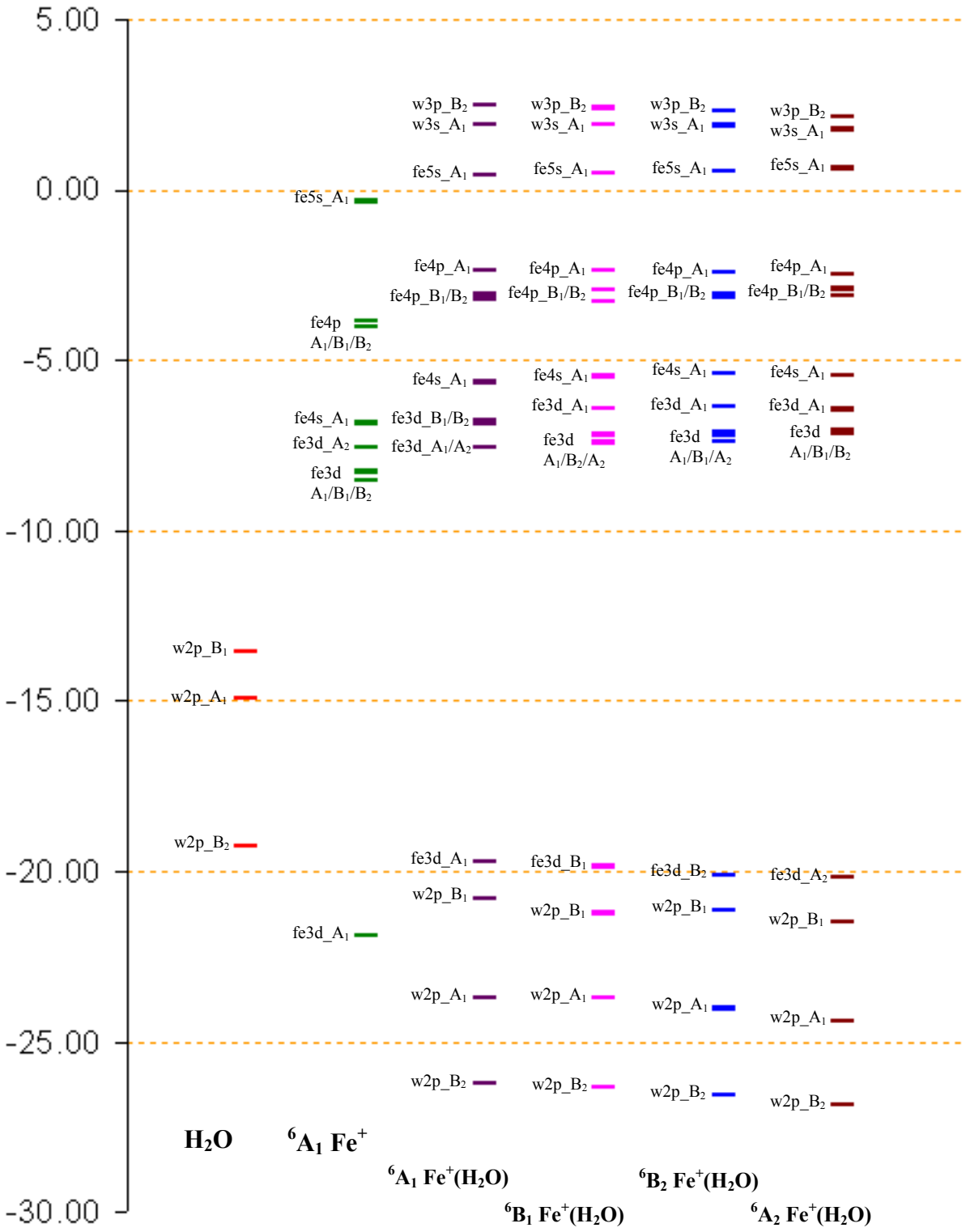

Figure 20. Atomic/molecular orbital energy distribution (in eV) of ROHF/6-31g calculations for H_2O, $^6A_1$ Fe^+, and all sextet states of $Fe^+(H_2O)$.

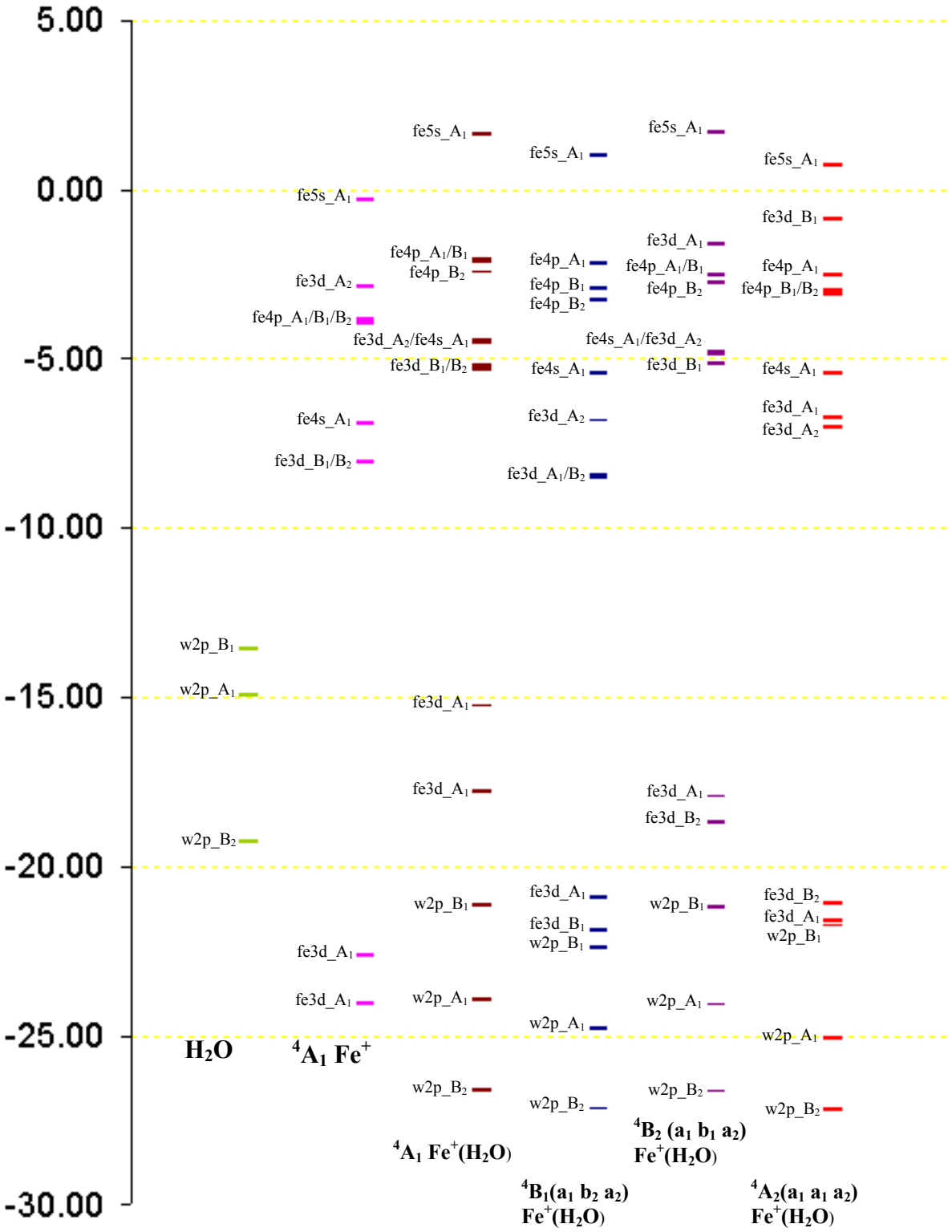

Figure 21. Atomic/molecular orbital energy distribution (in eV) of ROHF/6-31g calculations for H_2O, $^4A_1$ Fe^+, and all quartet states of $Fe^+(H_2O)$.

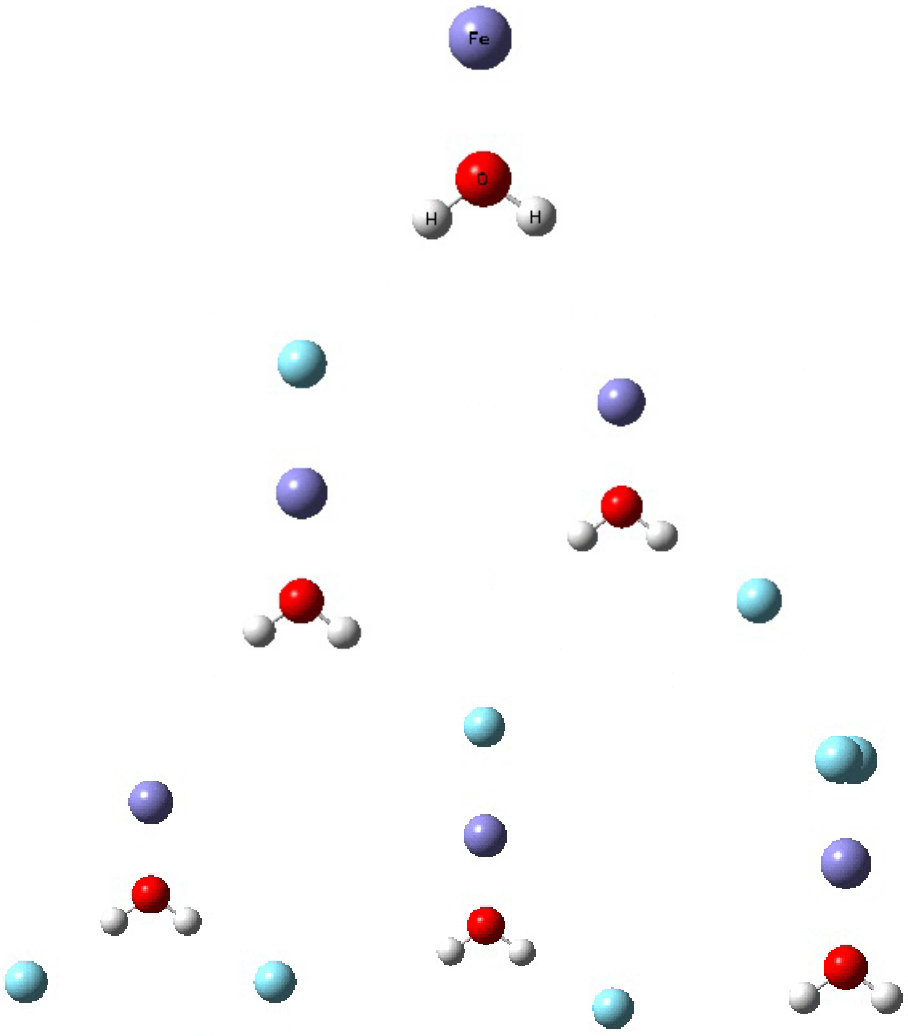

Figure 22. $Fe^{+}(H_2O)\ Ar_n$, n = 0-2, structures. The upper row represent $Fe^{+}(H_2O)$. The middle row represents $Fe^{+}(H_2O)$ Ar with Ar attached to Fe^{+} ion and OH group. The bottom row represents $Fe^{+}(H_2O)Ar_2$ with Ar attached to each OH group, one to Fe^{+} ion and one to OH group, and both to Fe^{+} ion.

4.4.1. $Fe^+(H_2O)$

4.4.1.1. Multiple Reference Calculations

The occupied orbitals from the various CASSCF calculations on $Fe^+(H_2O)$ are tabulated in Appendix A with graphical representations of the occupation of the 3d/4s orbitals. The quartet states are found to be separated from the sextet states by at least 15 kcal/mol, with the lowest quartet state being $^4A_1$ state as shown in Table 7. The (7, 6) CASSCF calculations give relative energies similar to those from the UHF calculations, with the exception of the $^4A_2$ states. On the other hand, the (7, 9) calculations give relative energies that different appreciably from those of the (7, 6) CASSCF calculations. This is due to the electron excitations from the inner shell orbitals to molecular orbitals derived mainly from the 4d orbitals of Fe^+. The detailed orbital occupations for the (7, 9) calculations are tabulated in Table 20-Table **27**. As shown in Figure 20 and Figure 21, the 2p type MO's of water are well separated from the 3d orbitals of Fe^+ atom for all sextet states but not for some of the quartet states. Therefore, expansion of the active space to include the 2p orbitals of water should be considered. The inclusion of the 2p orbitals of water together with the 3d and 4s orbitals of Fe^+ extends the active space to 13 electrons and 9 orbitals. The sextet states and $^4A_1$ state as determined by the (13, 9) CASSCF calculations show similar pattern in relative energies as obtained from the (7, 6) CASSCF calculations, but the relative energies of these states and the other quartet states differ appreciably in the two CASSCF spaces. That is due to the slightly larger fractional occupation on the first virtual orbital in some of the quartet states as described with the (13, 9) active space. For the (13, 12) CASSCF calculations, the $^6A_1$ state is found to involve excitation into MO's derived from the 4f orbitals of Fe^+. This

causes a shift in the relative energies of the higher lying states when using the (13, 12) active space.

Table 7. Calculated relative energies (kcal/mol) of various states $Fe^+(H_2O)$ at different levels of theory.

Electronic State	UHF[a]	(7, 6)	(7, 9)	(13, 9)	(13, 12)
$^6A_1$	0.00	0.00	0.00	0.00	0.00
$^6B_1$	4.20	4.17	3.25	4.18	5.52
$^6B_2$	2.67	2.72	1.68	2.72	4.05
$^6A_2$	0.59	0.01	11.04	0.02	1.62
$^4A_1$	**16.27**[c]	19.52	7.31	19.44	19.32
$^4B_1(a_1\ b_2\ a_2)$	40.25	31.58	7.40	35.40	32.67
$^4B_1(a_1\ a_1\ b_1)$	45.94	**38.91**[b]			
$^4B_2(a_1\ b_1\ a_2)$	38.96	30.43	5.88	34.35	31.55
$^4B_2(a_1\ a_1\ b_2)$	47.84	**40.49**[b]			
$^4A_2(a_1\ a_1\ a_2)$	49.68	**27.75**[b]	10.20	40.30	
$^4A_2(a_1\ b_1\ b_2)$	69.14	19.54			21.35

a. The UHF calculations used UMP2 optimized geometry.
b. The relative energy was estimated by two-state average CASSCF calculations.
c. Spin-contaminated.

Different configurations are found for lowest $^4A_2$ state as described with different size active spaces. The $^4A_2(a_1\ b_1\ b_2)$ configuration is found for the (7, 6) and (13, 12) calculations and the $^4A_2(a_1\ a_1\ a_2)$ configuration for the (7, 9) and (13, 9) calculations. Three excited states, *i.e.* $^4B_1(a_1\ a_1\ b_1)$, $^4B_2(a_1\ a_1\ b_2)$, and $^4A_2(a_1\ a_1\ a_2)$, were also considered in the (7, 6) calculations using the state-averaged CASSCF method. All sextet states and the $^4B_1(a_1\ b_2\ a_2)$ and $^4B_2(a_1\ b_1\ a_2)$ states are found to have nearly single-reference characteristic as shown in Table 8. Only the $^4A_1$, $^4B_1(a_1\ a_1\ b_1)$, $^4B_2(a_1\ a_1\ b_2)$ states, and the two $^4A_2$ states are multi-reference in nature.

Table 8. Calculated configurations of $Fe^{+}(H_2O)$ for the various electronic states at UHF and CASSCF levels.

Electronic State	UHF[a]	(7, 6)	(7, 9)	(13, 9)	(13, 12)
$^6A_1$	2++ + + +	2++ + + + (100%)	2++0 +0 +0 + (99%)	22++ 2+ 2+ + (100%)	22++0 2+0 2+0 + (97%)
$^6B_1$	+++ 2 + +	+++ 2 + + (100%)	+++0 20 +0 + (99%)	2+++ 22 2+ + (100%)	2+++0 220 2+0 + (97%)
$^6B_2$	+++ + 2 +	+++ + 2 + (100%)	+++0 +0 20 + (99%)	2+++ 2+ 22 + (100%)	2+++0 2+0 220 + (97%)
$^6A_2$	+++ + + 2	+++ + + 2 (100%)	+++0 +0 +0 2 (100%)	2+++ 2+ 2+ 2 (100%)	2+++0 2+0 2+0 2 (97%)
$^4A_1$	220 + + +	220 + + + (49%) 202 + + + (20%)	2200 +0 +0 + (97%)	2220 2+ 2+ + (48%) 2202 2+ 2+ + (20%)	22200 2+0 2+0 + (49%) 22020 2+0 2+0 + (19%)
$^4B_1$ (a_1 b_2 a_2)	2+0 2 + +	2+0 2 + + (99%)	2+00 20 +0 + (97%)	22+0 22 2+ + (99%)	22+00 220 2+0 + (96%)
$^4B_1$ (a_1 a_1 b_1)	++0 + 2 2	***++0 + 2 2 (85%) +20 2 + + (14%)***			
$^4B_2$ (a_1 b_1 a_2)	2+0 + 2 +	2+0 + 2 + (99%)	2+00 +0 20 + (97%)	22+0 2+ 22 + (99%)	22+00 2+0 220 + (96%)
$^4B_2$ (a_1 a_1 b_2)	++0 2 + 2	***++ 2 + 2 (82%) +20 + 2 + (17%)***			
$^4A_2$ (a_1 a_1 a_2)	++0 2 2 +	***++0 2 2 + (77%) +20 + + 2 (22%)***	++00 20 20 + (89%) 2+00 +0 +0 2 (9%)	2++0 22 22 + (85%) 22+0 2+ 2+ 2 (14%)	
$^4A_2$ (a_1 b_1 b_2)	2+0 + + 2	2+0 + + 2 (49%) 0+2 + + 2 (20%)			22+00 2+0 2+0 2 (67%) 20+20 2+0 2+0 2 (20%)

a. The UHF calculations used UMP2 optimized geometry.
b. The configurations in bold italic were calculated by two-state average CASSCF(7, 6) calculations.

We expected that the (13, 12) active space would be the most appropriate of those considered for $Fe^+(H_2O)$. However, the CASSCF calculations with this active space experienced fractional electron excitation from inner shell electrons and the fractional electron population of high-lying virtual orbitals. For this reason we scaled back to the smaller space, *i.e.* 7 electrons and 6 orbitals, for the CASMP2 calculations.

CASMP2(7, 6) numerical optimizations were carried out to investigate the relative energetics for the various electronic states of $Fe^+(H_2O)$. The results shown in Table 9 are in good agreement with the UMP2 calculations for the sextet states but different for the quartet states. The $^6A_1$, $^6A_2$, and $^4A_2$(a1 a1 a2) states are predicted to be almost degenerate, while the $^4B_2$(a1 b1 a2) state is calculated to be only 1.14 kcal/mol higher than the ground state. The $^6A_1$ state is found as the ground state for both CASSCF and CASMP2 calculations, which is in agreement with the calculations of Rosi and Bauschlicher at the SCF level.[168]

Table 9. Calculated OH stretch frequency (cm^{-1}) and relative energies (kcal/mol) for $Fe^{+}(H_2O)$ at UHF, UMP2, and CASSCF(7, 6) level.

Electronic State	UMP2 frequency[a]		UHF[b]	UMP2	CASSCF(7, 6)	CASMP2(7, 6)
$^6A_1$	3559	3652	0.00	0.00	0.00	0.00
$^6B_1$	3574	3668	4.20	4.37	4.17	4.58
$^6B_2$	3567	3662	2.67	2.22	2.72	2.32
$^6A_2$	3560	3652	0.59	0.02	0.01	0.02
$^4A_1$	3560	3654	**16.27**[c]	**12.70**[c]	19.52	17.81
$^4B_1(a_1\ b_2\ a_2)$	3609	3701	40.25	-0.06	31.58	3.28
$^4B_1(a_1\ a_1\ b_1)$	3602	3691	45.94	3.52	38.91[d]	
$^4B_2(a_1\ b_1\ a_2)$	3602	3691	38.96	-2.15	30.43	1.14
$^4B_2(a_1\ a_1\ b_2)$	3612	3702	47.84	6.78	40.49[d]	
$^4A_2(a_1\ a_1\ a_2)$	3612	3701	49.68	7.33	27.75[d]	0.004
$^4A_2(a_1\ b_1\ b_2)$	3594	3691	69.14	23.56	19.54	

a. The calculated frequencies are scaled by 0.954, the mean of the scale factors needed to bring the calculated frequencies of the symmetric and asymmetric stretch frequencies of H_2O into agreement with experiment.
b. All states were optimized at UMP2 level.
c. Spin contaminated calculations.
d. The relative energy was estimated by two-state average CASSCF calculations.

4.4.1.2. UMP2 calculations

The patter of relative energies pattern for the sextet states is very similar in both the UHF and UMP2 calculations. However, the UMP2 calculations significantly reduce the energy gap between the sextet and quartet states. Indeeded, with the UMP2 calculations two of the quartet states, *i.e.* $^4B_1(a_1\ b_2\ a_2)$ and $^4B_2(a_1\ b_1\ a_2)$, are lower in energy than $^6A_1$ state by 0.06 and 2.15 kcal/mol, respectively. UMP2 calculations were also carried out for the $^4B_1(a_1\ a_1\ b_1)$, $^4B_2(a_1\ a_1\ b_2)$, and $^4A_2(a_1\ b_1\ b_2)$ states.

The optimized geometries of the various states of $Fe^+(H_2O)$ are summarized in Table 10. The FeO bond length is 0.03 – 0.15 Å longer in the sextet than in the quartet states, and the OH bond lengths are about 0.004 Å longer in the sextet than in the quartet states.

Table 10. Calculated $Fe^+(H_2O)$ structures at UMP2 level

Electronic State	rFeO	rOH	aHOH
$^6A_1$	2.096	0.969	126.73
$^6B_1$	2.164	0.968	127.04
$^6B_2$	2.111	0.968	126.87
$^6A_2$	2.096	0.969	126.74
$^4A_1$	2.014	0.969	126.27
$^4B_1(a_1\ b_2\ a_2)$	2.055	0.965	126.80
$^4B_1(a_1\ a_1\ b_1)$	2.013	0.965	126.79
$^4B_2(a_1\ b_1\ a_2)$	2.018	0.965	126.92
$^4B_2(a_1\ a_1\ b_2)$	2.069	0.965	126.96
$^4A_2(a_1\ a_1\ a_2)$	2.046	0.965	127.01
$^4A_2(a_1\ b_1\ b_2)$	2.027	0.966	126.59

a. The unit of bond length is in Å.
b. The unit of HOH angle is in degree.

4.4.1.3. UMP2 calculated frequency and DFT calculations

The calculated OH stretch frequencies at the UMP2 level show significant differences between the sextet and quartet states. The OH stretch frequencies of the sextet states are red shifted at about 100 cm^{-1} from the experimental values for the isolated water monomer, while those of the quartet states are red-shifted by only about 50 cm^{-1}. Charge density distributions of the various states, calculated with using Mulliken analysis and Hartree-Fock single-reference wavefunctions are shown in Table 11. The charge density is more delocalized in the sextet states

than in the $^4B_1(a_1\ b_2\ a_2)$ and $^4B_2(a_1\ b_1\ a_2)$ quartet states. In other words, more electron density is withdrawn from the OH bond to Fe^+ ion for the sextet states than for the two quartet states. As a consequence, the more "deficient" OH bond leads to more red-shifted OH stretch frequencies.

Table 11. Mulliken charge analysis of $Fe^+(H_2O)$ for several single-reference electronic state.

Electronic State	O	Fe	H
$^6A_1$	-0.843	0.879	0.482
$^6B_1$	-0.828	0.887	0.471
$^6B_2$	-0.831	0.882	0.474
$^6A_2$	-0.843	0.879	0.482
$^4B_1(a_1\ b_2\ a_2)$	-0.906	0.909	0.498
$^4B_2(a_1\ b_1\ a_2)$	-0.907	0.910	0.499

a. The Mulliken charge analysis was calculated at UMP2/6-31G with using UMP2/ TZVP+G(3df,2p) geometries.

The $^4A_1$ state displayed sizable spin contamination at the UMP2 level. As a result we also investigated the various states using density functional theory for which less spin contamination is less problematical. Although the DFT calculations predicted the quartet states to be lower in energy than the sextet states, all quartet states still were found to have similar OH stretch frequencies well separated from those of the sextet states. Thus the UMP2 OH stretch frequencies of the $^4A_1$ state are expected to be close to those of other quartet states were the spin contamination removed.

Table 12. Calculated $Fe^+(H_2O)$ energies (kcal/mol) and OH stretching frequencies (cm^{-1}) at DFT level.

Electronic State	UDFT frequency[a]		UDFT
$^6A_1$	3552	3634	0.00
$^6B_1$	3577	3659	4.90
$^6B_2$	3562	3645	2.27
$^6A_2$	3551	3633	-0.01
$^4A_1$	3604	3680	-8.81
$^4B_1(a_1\ b_2\ a_2)$	3620	3696	-6.62
$^4B_1(a_1\ a_1\ b_1)$	3605	3676	-3.81
$^4B_2(a_1\ b_1\ a_2)$	3607	3662	-8.87
$^4B_2(a_1\ a_1\ b_2)$	<u>3623</u>[b]	<u>3697</u>[b]	<u>-0.22</u>[b]
$^4A_2(a_1\ a_1\ a_2)$	3621	3692	-0.27
$^4A_2(a_1\ b_1\ b_2)$	3604	3678	-8.82

a. The calculated frequencies are scaled by 0.963, the mean of the scale factors needed to bring the calculated frequencies of the symmetric and asymmetric stretch frequencies of H_2O into agreement with experiment.
b. The underlined denotes the state with negative frequency found in the frequency calculation.

As seen from Table 13 the geometries calculated at the DFT level show the same trends as those from of the UMP2 calculations, namely the FeO and OH bond lengths are longer for the sextet states than for the quartet states.

Table 13. calculated $Fe^+(H_2O)$ structures at DFT level

Electronic State	rFeO	rOH	aHOH
$^6A_1$	2.089	0.970	126.17
$^6B_1$	2.166	0.968	126.46
$^6B_2$	2.107	0.969	126.32
$^6A_2$	2.091	0.970	126.19
$^4A_1$	1.995	0.967	125.96
$^4B_1(a_1\ b_2\ a_2)$	2.040	0.966	126.09
$^4B_1(a_1\ a_1\ b_1)$	1.995	0.966	126.18
$^4B_2(a_1\ b_1\ a_2)$	1.999	0.966	126.30
$^4B_2(a_1\ a_1\ b_2)$	2.053	0.965	126.29
$^4A_2(a_1, a_1, a_2)$	2.029	0.965	126.30
$^4A_2(a_1, b_1, b_2)$	1.996	0.967	125.96

a. The unit of bond length is in Å.
b. The unit of HOH angle is in degree.

4.4.2. $Fe^+(H_2O)Ar$

Two geometrical isomers of $Fe(H_2O)^+Ar$ are found at UMP2 level. The first one has the argon atom bound to the Fe^+ ion along the C_{2v} axis of $Fe(H_2O)^+$. The second one has the argon atom bound to an OH group.

4.4.2.1. Type I isomer: Ar bound on the Fe^+ ion

Preliminary calculations on isomer I at the ROHF/6-31G level (see Figure 23) show that the double occupied *d* orbitals of Fe^+, the *3p* orbitals of Ar, and the *2p* orbitals of water overlap in energy. Three sizes of active spaces were considered, and the results are shown in Table 14. Similar relative energies are found in the (7, 6) CASSCF and UHF calculations. However, the

$^4A_2(a_1\ a_1\ a_2)$ state, predicted to be the lowest energy $^4A_2$ state at the UMP2 level is not predicted to be the lowest energy $^4A_2$ state by all the CASSCF calculations. In particular the $(a_1\ b_1\ b_2)$ configuration of $^4A_2$ state is predicted to be 13.90 kcal/mol lower than the $(a_1\ a_1\ a_2)$ configuration in the (7, 6) CASSCF calculations. The other two sets of CASSCF calculations do not agree well with that of (7, 6) calculations, due to the same problems experienced in the $Fe^+(H_2O)$ system, *i.e.* fractional excitation from the inner shell and fractional electron population in high energy virtual orbitals. The detailed orbital energies are tabulated in Table 28-Table **35**.

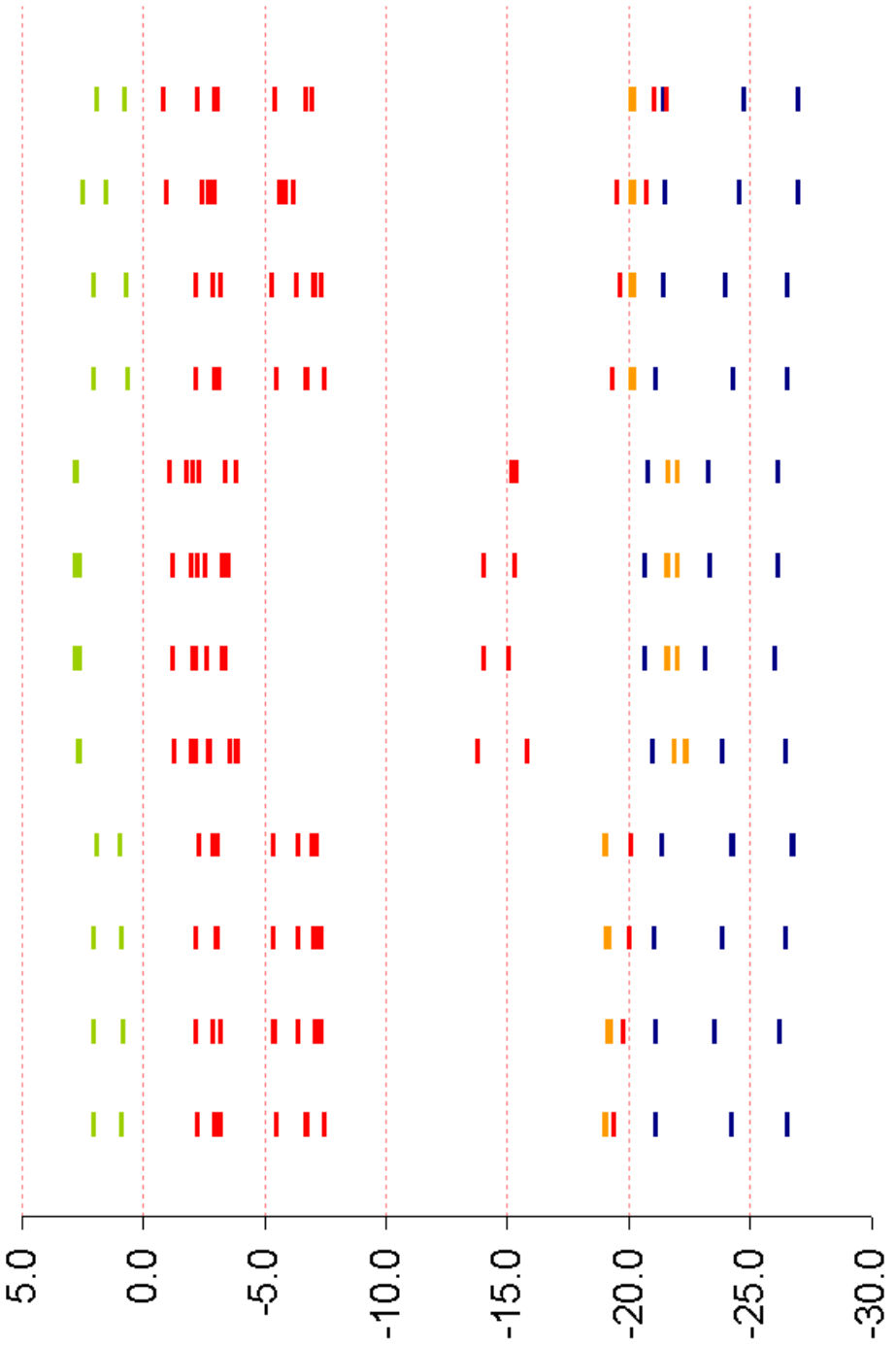

Figure 23. Orbital energy of $Fe^{+}(H_2O)Ar$ for various structures and electronic states, Fe_$^{6}A_1$, Fe_$^{6}B_1$, Fe_$^{6}B_2$, Fe_$^{6}A_2$, Fe_$^{4}A_1$, Fe_$^{4}B_1(a_1\ b_2\ a_2)$, Fe_$^{4}B_2(a_1\ b_1\ a_2)$, Fe_$^{4}A_2(a_1\ b_1\ b_2)$, OH_$^{6}A'$, OH_$^{6}A''$, OH_$^{4}A'$, and OH_$^{4}A''$, respectively. The first symbol denotes the attachment location of argon atom and the second denotes the electronic state. The red marks denote the molecular orbitals mainly resulted from by the 3d, 4s, and 4p Fe^{+} orbitals. The orange marks denote those resulted from 3p of Ar and the blue for 2p resulted from 2p of water. The greens denote other orbitals.

Table 14. Calcuated energies (kcal/mol) and OH stretch frequencies (cm^{-1}) of $Fe^{+}(H_2O)Ar$.

Electronic State	UMP2 frequency		UMP2	BE[a]	UHF[b]	(7, 6)	(13, 12)	(19, 15)
$^6A_1$	3560	3654	0.00	-0.67	0.00	0.00	0.00	0.00
$^6B_1$	3574	3670	4.25	-0.78	4.22	4.14	8.75	11.08
$^6B_2$	3567	3663	2.15	-0.73	2.74	2.70	7.40	9.12
$^6A_2$	3560	3654	0.02	-0.67	0.01	0.01	1.01	0.04
$^4A_1$	**3595**	**3689**	**5.02**	**-8.03**	**25.19**	19.49	8.46	11.94
$^4B_1$ (a_1 b_2 a_2)	3612	3705	-8.43	-8.53	37.79	31.32	20.37	11.08
$^4B_1$ (a_1 a_1 b_1)	3604	3693	-4.49	-8.19	43.08	38.99[e]		
$^4B_2$ (a_1 b_1 a_2)	3604	3693	-10.53	-8.55	36.55	26.65	9.02	9.12
$^4B_2$ (a_1 a_1 b_2)	3615	3706	-0.99	-7.94	44.93	37.09[e]		
$^4A_2$ (a_1 a_1 a_2)	3614	3703	-1.11	-8.58	47.25	33.37[e]		
$^4A_2$ (a_1 b_1 b_2)	**3595**	**3690**	**5.02**	**n/a**	**25.18**	19.47	25.82	20.38
$^6A'$	3517	3611	-2.07	-2.33	-0.79	-0.89	-0.88	-1.12
$^6A''$	3517	3611	-2.04	-2.33	-0.78	-0.87	-0.83	-3.14
$^4A'$	3545	3658	-2.85	-1.06	39.34	29.68	17.89	
$^4A''$	3577	3669	-1.68	n/a	39.29	18.61	22.30	18.13

a. Argon atom binding energy at UMP2 level with base set superposition error correction
b. UHF energy with UMP2 optimized geometry.
c. The calculated frequencies are scaled by 0.9542 which is resulted from by fitting calculated H_2O frequency to experiment.
d. The underlined denotes the isomer is optimized at the UMP2 level but the following frequency calculation found the negative frequency. The bold denotes spin contaminated UMP2 calculations.
e. The relative energy was estimated by two-state average CASSCF(7, 6) calculations.

The type I isomer is not a minimum for the sextet states or for the $^4B_2(a_1\ b_1\ a_2)$ and $^4B_2(a_1\ a_1\ b_2)$ states, as confirmed by the negative frequencies found at the UMP2 frequency calculations as shown in Table 14. Only the $^4A_1$, $^4B_1$, and $^4A_2$ states are predicted to exist to have type I

minima at the UMP2 level. We note that the $^4A_1$ and $^4A_2(a_1\ b_1\ b_2)$ states have sizable spin contamination. After including the counterpoise correction for basis set superposition error, the argon atom binding energies of the quartet states are much stronger than those of sextet states as shown in Table 14. It is shown in Table 15 that all the sextet states, and the $^4B_2(a_1\ b_1\ a_2)$ and $^4B_2(a_1\ a_1\ b_2)$ states are single-reference in nature, while the other states are multi-reference in nature and experience spin contamination problems in the UMP2 calculations.

Table 15. Calculated configurations of $Fe^+(H_2O)Ar$ where argon atom is bound on Fe^+ for the various electronic states at UHF and CASSCF levels.

Electronic State	UHF[a]	(7, 6)	(13, 12)	(19, 15)
$^6A_1$	2++ + + +	2++ + + +(100%)	22++0 2+0 2+0 +(99%)	222++0 22+0 22+0 +(99%)
$^6B_1$	+++ 2 + +	+++ 2 + +(100%)	2+++0 220 2+0 +(99%)	22+++0 2220 22+0 +(99%)
$^6B_2$	+++ + 2 +	+++ + 2 +(100%)	2+++0 2+0 220 +(99%)	22+++0 22+0 2220 +(99%)
$^6A_2$	+++ + + 2	+++ + + 2(100%)	2+++0 2+0 2+0 2(99%)	22+++0 22+0 22+0 2(99%)
$^4A_1$	220 + + +	220 + + +(75%) 202 + + +(11%)	22200 2+0 2+0 +(96%)	222200 22+0 22+0 +(88%)
$^4B_1$ (a_1 b_2 a_2)	2+0 2 + +	2+0 2 + +(99%)	22+00 220 2+0 +(97%)	222+00 2220 22+0 +(97%)
$^4B_1$ (a_1 a_1 b_1)	++0 + 2 2	***++0 + 2 2(85%)*** ***+20 2 + +(14%)***		
$^4B_2$ (a_1 b_1 a_2)	2+0 + 2 +	2+0 + 2 +(99%)	22+00 2+0 220 +(97%)	222+00 22+0 2220 +(97%)
$^4B_2$ (a_1 a_1 b_2)	++0 2 + 2	***++0 2 + 2(82%)*** ***+20 + 2 +(17%)***		
$^4A_2$ (a_1 a_1 a_2)	++0 2 2 +	***++0 2 2 +(79%)*** ***+20 + + 2(21%)***		
$^4A_2$ (a_1 b_1 b_2)	2+0 + + 2	2+0 + + 2(75%) 0+2 + + 2(11%)	22+00 2+0 2+0 2(76%) 20+20 2+0 2+0 2(10%)	222+00 22+0 22+0 2(74%) 220+20 22+0 22+0 2(10%)

a. The configurations in bold italic were calculated by two-state average CASSCF(7, 6) calculations.

The optimized structures of $Fe(H_2O)^+Ar$ show significant differences between the sextet and quartet states as shown in Table 16. The argon atom in the sextet states is bound about at least 3.7 Å from the Fe^+ ion, while in the quartet state the Fe^+Ar distance is only 2.4 Å. The distance between Fe^+ ion and O atom is 0.1 Å longer in the sextet than in the quartet states``. The OH bond lengths of the sextet states are about 0.004 Å longer than those of the quartet states.

Table 16. $Fe^+(H_2O)Ar$ structures optimized at UMP2 level. The argon atom is attached to Fe atom.

Electronic State	rArFe	rFeO	rOH	aHOH
$^6A_1$	3.904	2.102	0.968	126.74°
$^6B_1$	3.763	2.173	0.968	127.05°
$^6B_2$	3.814	2.118	0.968	126.88°
$^6A_2$	3.904	2.102	0.969	126.75°
$^4A_1$	2.381	1.960	0.966	126.16°
$^4B_1(a_1\ b_2\ a_2)$	2.423	2.029	0.965	126.65°
$^4B_1(a_1\ a_1\ b_1)$	2.443	1.995	0.965	126.70°
$^4B_2(a_1\ b_1\ a_2)$	2.423	1.992	0.965	126.82°
$^4B_2(a_1\ a_1\ b_2)$	2.450	2.051	0.965	126.87°
$^4A_2(a_1\ a_1\ a_2)$	2.414	2.023	0.964	126.89°
$^4A_2(a_1\ b_1\ b_2)$	2.382	1.960	0.966	126.16°

a. The bond length is in Å.

4.4.2.2. Type II isomer: Ar bound to OH group

The (7, 6) CASSCF calculations on the type II isomers are in close agreement with UHF calculations, while the (13, 12) and (19, 15) CASSCF calculation are not. The $^4A''$ state has multi-reference character while the other three states are dominated by single configurations as shown in Table 17. All type II isomers are close in energy at the UMP2 level as shown in Table 14. The argon atom binding energies of the $^6A'$ and $^6A''$ states are almost identical at 2.33 kcal/mol, whereas for the $^4A'$ the argon atom binding energy is only 1.06 kcal/mol. The argon atom binding energies of the various type II isomers are expected to be similar since the Ar atom is bound onto the OH group and less influenced by the electronic configuration of the metal ion.

Table 17. Calculated configurations of $Fe^+(H_2O)Ar$ where argon atom is bound onto OH for the various electronic states at UHF and CASSCF levels.

Electronic State	UHF[a]	(7, 6)	(13, 12)	(19, 15)
$^6A'$	2+++ ++	2+++ ++(100%)	222+++00 2++0(99%)	22222+++00 22++0(99%)
$^6A''$	++++ 2+	++++ 2+(100%)	22++++00 22+0(99%)	2222++++00 222+0(98%)
$^4A'$	22+0 ++	22+0 ++(99%)	2222+000 2++0(97%)	222222+000 22++0(97%)
$^4A''$	2++0 2+	2++0 2+(49%) 0++2 2+(20%)	222++000 22+0(67%) 220++200 22+0(12%)	n/a

4.4.2.3. Calculated OH stretching frequencies of $Fe^+(H_2O)$ and $Fe^+(H_2O)Ar$

When the argon atom is bound to an OH group as for the $^6A'$ state of $Fe^+(H_2O)Ar$, the OH stretch frequencies are red shifted about 40 cm^{-1} from those of the $^6A_1$ state of $Fe^+(H_2O)$. On the other hand, if the argon atom is bound to the Fe^+ ion, it has a smaller impact on the OH stretch frequencies. Only small blue shifts of about 3 cm^{-1} are predicted in the OH stretch frequencies in going from $Fe^+(H_2O)$ to $Fe^+(H_2O)$ Ar (this is for the $^4B_1(a_1\ b_2\ a_2)$ state). The sensitivity of the frequency shifts to the binding position of the argon atoms aids in assigning the infrared photodissociation spectra.

4.4.3. $Fe^+(H_2O)\ Ar_2$

There are three types of isomers for $Fe^+(H_2O)\ Ar_2$. The first type has argon atoms bound to each OH group. The second type has one argon atom bound to Fe^+ ion and the other argon atom bound to an OH group. The third type has two argon atoms bound to Fe^+ ion, on opposite sides of the $Fe^+(H_2O)$ plane.

4.4.3.1. Type I isomer of $Fe^+(H_2O)Ar_2$: Ar bound to each OH group

The sextet states and the $^4B_1(a_1\ b_2\ a_2)$ and $^4B_2(a_1\ b_1\ a_2)$ states, are determined to have single-reference character in the CASSCF(7, 6) calculations while other states are multi-reference in nature. All sextet states are found to have type I local minimum in the UMP2 calculations as shown in Table 18. The $^6A_1$ state is the lowest energy state of sextet state at the UMP2 level. Only three quartet states are found to have type I minima at the UMP2 level, *i.e.* $^4A_1$, $^4B_1(a_1\ a_1$

b_1), and $^4A_2(a_1\ b_1\ b_2)$. The $^4A_1$ state is spin-contaminated. The argon atom binding energies of the type I isomers of $Fe^+(H_2O)Ar_2$ are larger for the sextet states than for the quartet states as shown in Table 18.

Table 18. Calcuated energies (kcal/mol) and OH stretch frequencies (cm^{-1}) of $Fe^+(H_2O)Ar_2$.

Electronic State	UMP2 frequency		UMP2	B.E.[a]	UHF	CASSCF(7, 6)
Argons on OH						
$^6A_1$	3487	3564	0.00	-4.60	0.00	0.00
$^6B_1$	3516	3597	4.96	-4.07	4.44	4.47
$^6B_2$	3506	3587	2.60	-4.24	2.93	2.94
$^6A_2$	3488	3564	0.03	-4.60	0.01	0.01
$^4A_1$	**3482**	**3559**	**12.52**	**-4.72**	**15.67**	9.43
$^4B_1(a_1\ b_2\ a_2)$	3555	3636	0.82	-3.76	40.45	32.17
$^4B_1(a_1\ a_1\ b_1)$	3550	3628	4.36	-3.80	46.04	39.48[c]
$^4B_2(a_1\ b_1\ a_2)$	3550	3628	-1.33	-3.82	39.10	30.97
$^4B_2(a_1\ a_1\ b_2)$	3560	3639	7.72	-3.73	47.96	41.09[c]
$^4A_2(a_1\ a_1\ a_2)$	3564	3644	8.38	-3.61	49.91	28.09
$^4A_2(a_1\ b_1\ b_2)$	3530	3616	24.19	-3.99	69.12	19.46
Argons on OH and Fe^+						
$^6A'$	3501	3629	2.08	-2.95	0.71	0.86
$^6A''$	3501	3629	2.11	-2.95	0.72	0.87
$^4A'$	3565	3675	-8.61	-11.95	37.95	20.46
$^4A''$	3567	3678	-6.83	-11.42	37.58	31.70[d]
Argons on Fe^+						
$^4A_1$	3640	3708	-7.00	-10.61	38.79	31.68[d]
$^4B_1(a_1\ b_2\ a_2)$	3608	3699	-8.72	-10.99	36.34	27.71
$^4B_1(a_1\ a_1\ b_1)$			n/a			39.26[c]
$^4B_2(a_1\ b_1\ a_2)$	3598	3691	-1.89	-7.72	39.45	31.83[d]
$^4B_2(a_1\ a_1\ b_2)$	3610	3700	-4.38	-10.87	42.71	36.95[c]
$^4A_2(a_1\ a_1\ a_2)$	3621	3712	4.81	-14.93	48.46	21.05
$^4A_2(a_1\ b_1\ b_2)$	3601	3696	14.17	-14.60	66.00	29.45[c]

a. Argon atom binding energy including basis set superposition error correction.
b. The underlined denotes the isomer is optimized at the UMP2 level but the following frequency calculation found the negative frequency. The bold denotes spin contaminated UMP2 calculations.
c. Two-state average CASSCF(7, 6) calculations
d. Single point CASSCF(7, 6) calculations with using UMP2 optimized structures.

4.4.3.2. Type II isomer of $Fe^+(H_2O)Ar_2$: Ar bound Fe^+ ion and OH group

The sextet states of the type II isomers are predicted to have single-reference character in the CASSCF(7, 6) calculations, while the corresponding quartet states are multi-reference in nature. Only the quartet states of the type II isomers are local minima at UMP2 level. The argon atom binding energies are about five times larger in the quartet than the sextet states. This follows from the results for the $Fe^+(H_2O)Ar$ clusters, where the Ar atom is bound about 1.5 Å closer to the Fe^+ ion in the quartet than in the sextet states.

4.4.3.3. Type III isomer of $Fe^+(H_2O)Ar_2$: Ar bound to Fe^+ ion

Two argon atoms cannot bind to the Fe^+ ion in any of the sextet states as treated at the UMP2 level. This can be understood by the fact that the argon atom of $Fe^+(H_2O)Ar$ is bound far away from the Fe^+ ion, *i.e.* at least 3.7 Å. It is anticipated that the barrier for rotating an argon atom from the Fe^+ binding site to the OH binding site is very small. Only the $^4B_1(a_1\ b_2\ a_2)$, $^4B_2(a_1\ a_1\ b_2)$, and $^4A_2(a_1\ b_1\ b_2)$ states of $Fe^+(H_2O)Ar_2$ are found to have type III local minima. The $^4A_2(a_1\ b_1\ b_2)$ state is found to have strongest net argon atom binding energy at -14.60 kcal/mol, while the $^4B_1(a_1\ b_2\ a_2)$ and $^4B_2(a_1\ a_1\ b_2)$ states have net Ar atom binding energies of -11.00 kcal/mol. Only the $^4B_1(a_1\ b_2\ a_2)$ and $^4B_2(a_1\ b_1\ a_2)$ states are predicted to be well described by single-reference wavefunctions.

4.4.3.4. OH stretch frequency comparison between experiment and theory

Walters and Duncan have measured the IR spectrum of $Fe^+(H_2O)Ar_2$, but experimental IR spectra of $Fe^+(H_2O)$ and $Fe^+(H_2O)Ar$ are not available.[135] The experimental spectrum of $Fe^+(H_2O)Ar_2$ (Figure 24) displays two intense peaks at 3554 and 3661 cm^{-1} and two weak peaks at 3615 and 3684 cm^{-1}. The calculated OH stretch spectrum of the type I and type III isomers of $Fe^+(H_2O)Ar_2$ do not match with the intense pair of peaks observed experimentally. We therefore assign the intense pair of peaks to the $^4A'$ and $^4A''$ states of the type II isomer of $Fe^+(H_2O)\ Ar_2$ in which argon atoms are bound to the Fe^+ ion and one of the OH groups. Although the $^4A'$ state of the type II isomer is predicted to have multi-reference character as shown in Table 19, it is expected the frequencies calculated at the UMP2 level should actually be close to those of CASMP2 calculations, were it possible to carry out the latter calculations.

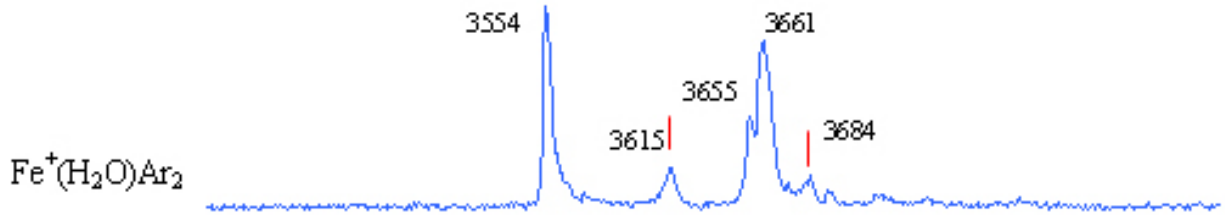

Figure 24. The IR spectra of $Fe^+(H_2O)\ Ar_2$ complex in the OH stretching region.[135]

The OH stretch frequencies of the quartet state of the type III isomer of $Fe^+(H_2O)\ Ar_2$ are close to the weak pair of peaks. The $^4A_2(a_1\ b_1\ b_2)$ state is predicted to have the with highest net argon atom binding energy at -14.60 kcal/mol, whereas the net binding energy of the argon atoms in the $^4B_1(a_1\ b_2\ a_2)$ and $^4B_2(a_1\ a_1\ b_2)$ states is calculated to be at -10.99 and -10.87 kcal/mol, respectively. Although the calculated OH stretch frequencies of the $^4B_1(a_1\ b_2\ a_2)$ and

$^4B_2(a_1\ a_1\ b_2)$ states are slightly closer to the experimental weak pair, *i.e.* 3615 and 3684 cm^{-1}, the $^4A_2(a_1\ b_1\ b_2)$ state could be the dominant configuration due to its greater stability.

Table 19. Calculated configurations of $Fe^+(H_2O)Ar_2$ at UHF and CASSCF levels.

Electronic State	UHF[a]	(7, 6)	Electronic State	UHF[a]	(7, 6)
Argons on OH			Argons on OH and Fe^+		
$^6A_1$	2++ + + +	2++ + + + (100%)	$^6A'$	2+++ ++	2+++ ++ (100%)
$^6B_1$	+++ 2 + +	+++ 2 + + (100%)	$^6A''$	++++ 2+	++++ 2+ (100%)
$^6B_2$	+++ + 2 +	+++ + 2 + (100%)	$^4A'$	22+0 ++	22+0 ++ (75%) 20+2 ++ (11%)
$^6A_2$	+++ + + 2	+++ + + 2 (100%)	$^4A''$	2++0 2+	2++0 2+ (99%)
			Argons on Fe^+		
$^4A_1$	220 + + +	220 + + + (49%) 202 + + + (20%)	$^4A_1$	220 + + +	220 + + + (71%) 202 + + + (12%)
$^4B_1$ (a_1 b_2 a_2)	2+0 2 + +	2+0 2 + + (99%)	$^4B_1$ (a_1 b_2 a_2)	2+0 2 + +	2+0 2 + + (99%)
$^4B_1$ (a_1 a_1 b_1)	++0 + 2 2	***++0 + 2 2 (85%)*** ***+20 2 + + (14%)***	$^4B_1$ (a_1 a_1 b_1)	n/a	***++0 + 2 2 (80%)*** ***+20 2 + + (19%)***
$^4B_2$ (a_1 b_1 a_2)	2+0 + 2 +	2+0 + 2 + (99%)	$^4B_2$ (a_1 b_1 a_2)	2+0 + 2 +	2+0 + 2 + (99%)
$^4B_2$ (a_1 a_1 b_2)	++0 2 + 2	***++0 2 + 2 (82%)*** ***+20 + 2 + (17%)***	$^4B_2$ (a_1 a_1 b_2)	++0 2 + 2	***++0 2 + 2 (88%)*** ***+20 + 2 + (12%)***
$^4A_2$ (a_1 a_1 a_2)	++0 2 2 +	***++0 2 2 + (77%)*** ***+20 + + 2 (22%)***	$^4A_2$ (a_1 a_1 a_2)	++0 2 2 +	***++0 2 2 + (77%)*** ***+20 + + 2 (22%)***
$^4A_2$ (a_1 b_1 b_2)	2+0 + + 2	2+0 + + 2 (49%) 0+2 + + 2 (20%)	$^4A_2$ (a_1 b_1 b_2)	2+0 + + 2	2+0 + + 2 (51%) 0+2 + + 2 (20%)

a. The configurations in bold italic were calculated by two-state average CASSCF(7, 6) calculations.

4.5. CONCLUSIONS

The sextet states and the $^4B_1(a_1\ b_2\ a_2)$ and $^4B_2(a_1\ b_1\ a_2)$ states are found to be well described by a single configuration with or without argon atoms attached to the cluster while the other quartet states are multi-configurational in nature. Although the CASSCF calculations of $Fe^+(H_2O)Ar_{1,2}$ predict the quartet states to lie much higher in energy than the sextet states, the inclusion of dynamic electron correlation should stabilize the quartet states much more than the sextet states, as seen from the CASMP2 calculations on $Fe^+(H_2O)$.

It has been shown that the calculated OH stretch frequencies of the quartet states of the type II isomer of $Fe^+(H_2O)Ar_2$, in which argon atoms are bound to both the Fe^+ ion and the OH group, matches the intense pair of peaks (3554/3661 cm^{-1}). In addition, the vibrational spectrum calculated for the quartet states of the type III isomer of $Fe^+(H_2O)Ar_2$ matches the weak pair of observed peaks (3615/3684 cm^{-1}). We note also that the UMP2 calculations predict the most stable isomers of $Fe^+(H_2O)Ar_2$ to have quartet spin multiplicity.

4.6. ACKNOWLEDGEMENTS

This research was carried out with support from National Science Foundation. We thank Prof. M. Duncan for making available his $Fe^+(H_2O)\ Ar_2$ photodissociation spectrum and for helpful discussions. The calculations were performed on computers in the Center for Molecular and Materials Simulations in University of Pittsburgh.

APPENDIX A

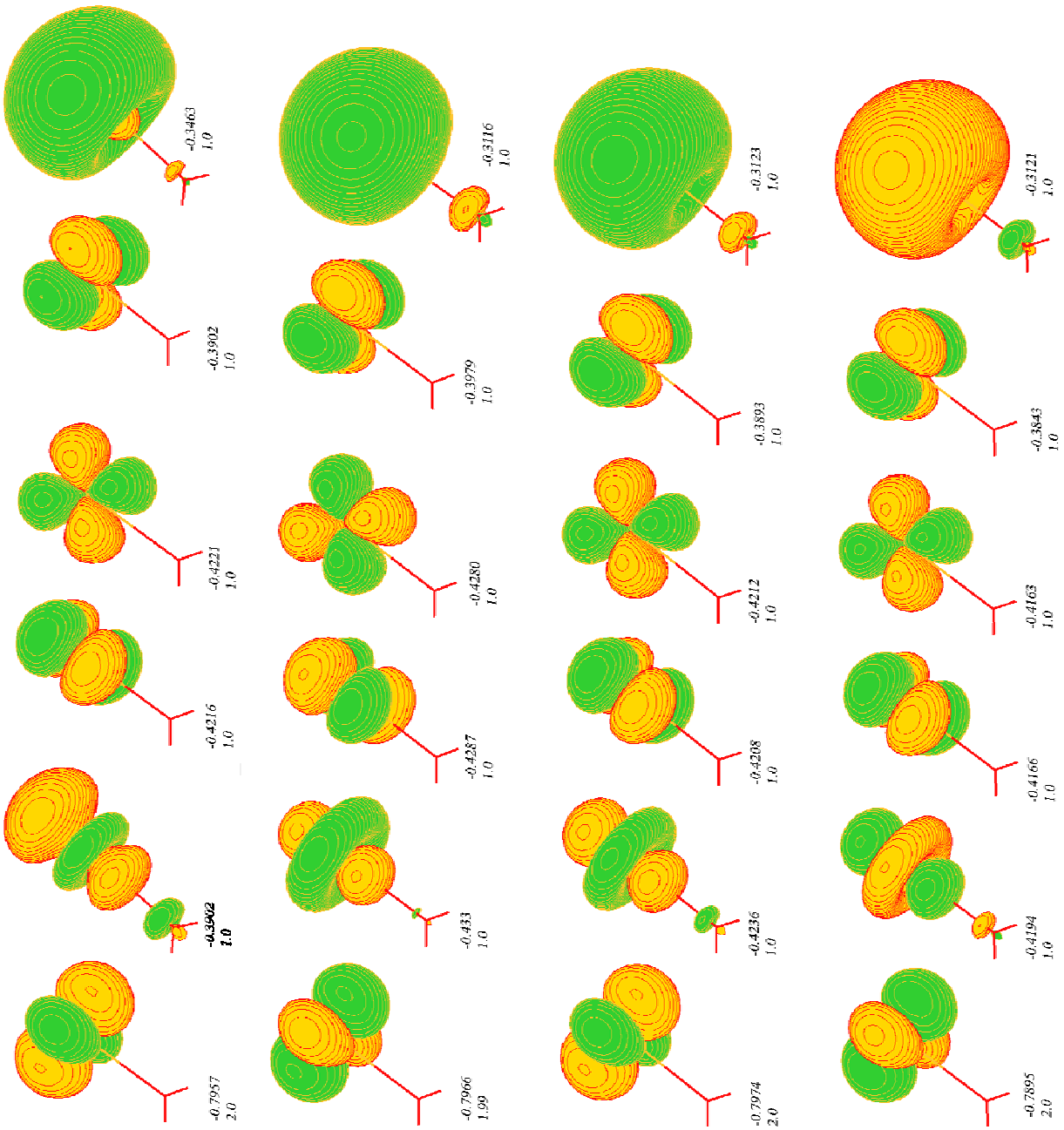

Figure 25. The ground state 3d/4s orbitals energy and occupation number of $^6A_1$ $Fe^+(H_2O)$ for (7, 6), (7, 9), (13, 9), and (13, 12) CASSCF calculations.

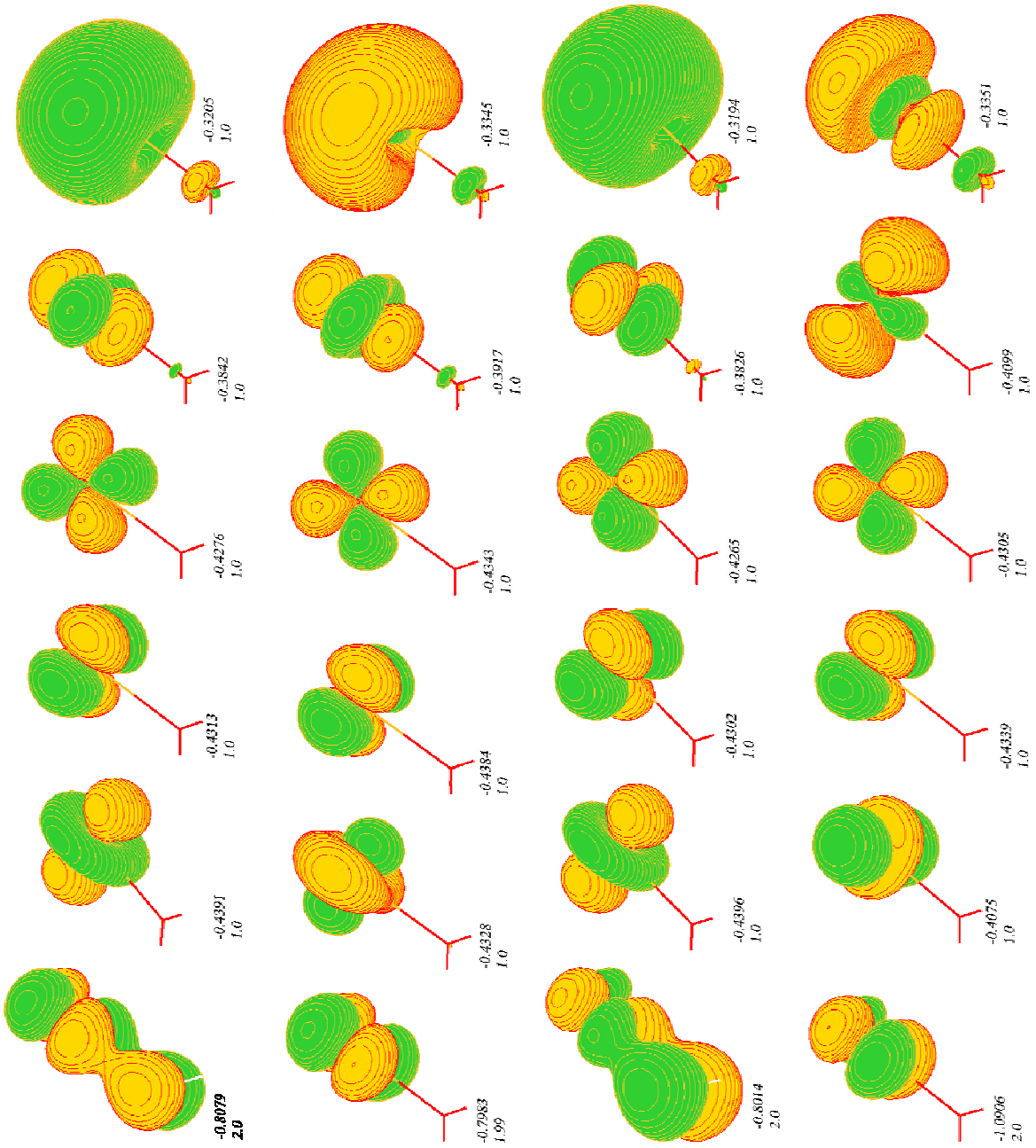

Figure 26. The ground state 3d/4s orbitals energy and occupation number of $^6B_1$ $Fe^+(H_2O)$ for (7, 6), (7, 9), (13, 9), and (13, 12) CASSCF calculations.

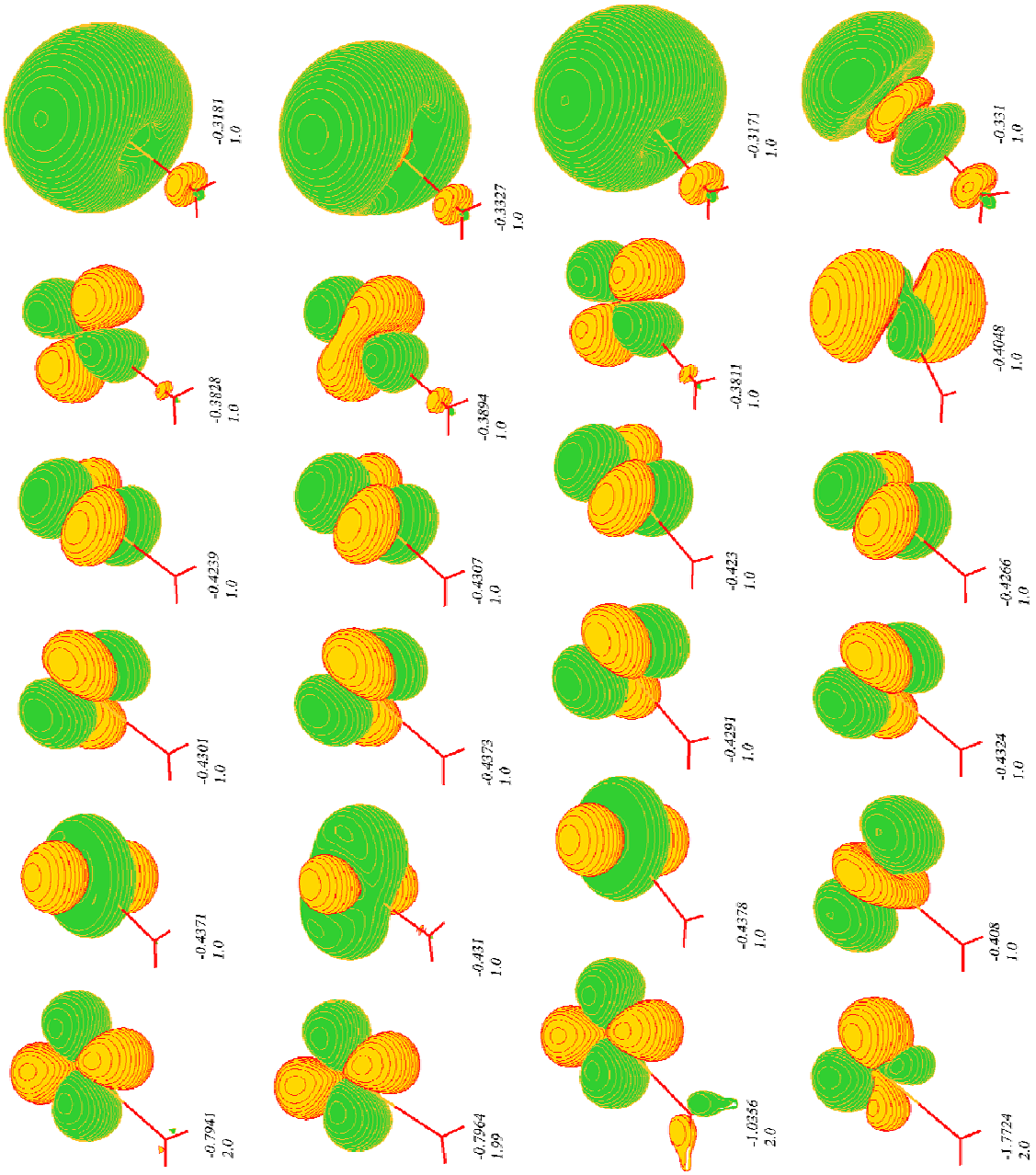

Figure 27. The ground state 3d/4s orbitals energy and occupation number of $^{6}B_2$ $Fe^{+}(H_2O)$ for (7, 6), (7, 9), (13, 9), and (13, 12) CASSCF calculations.

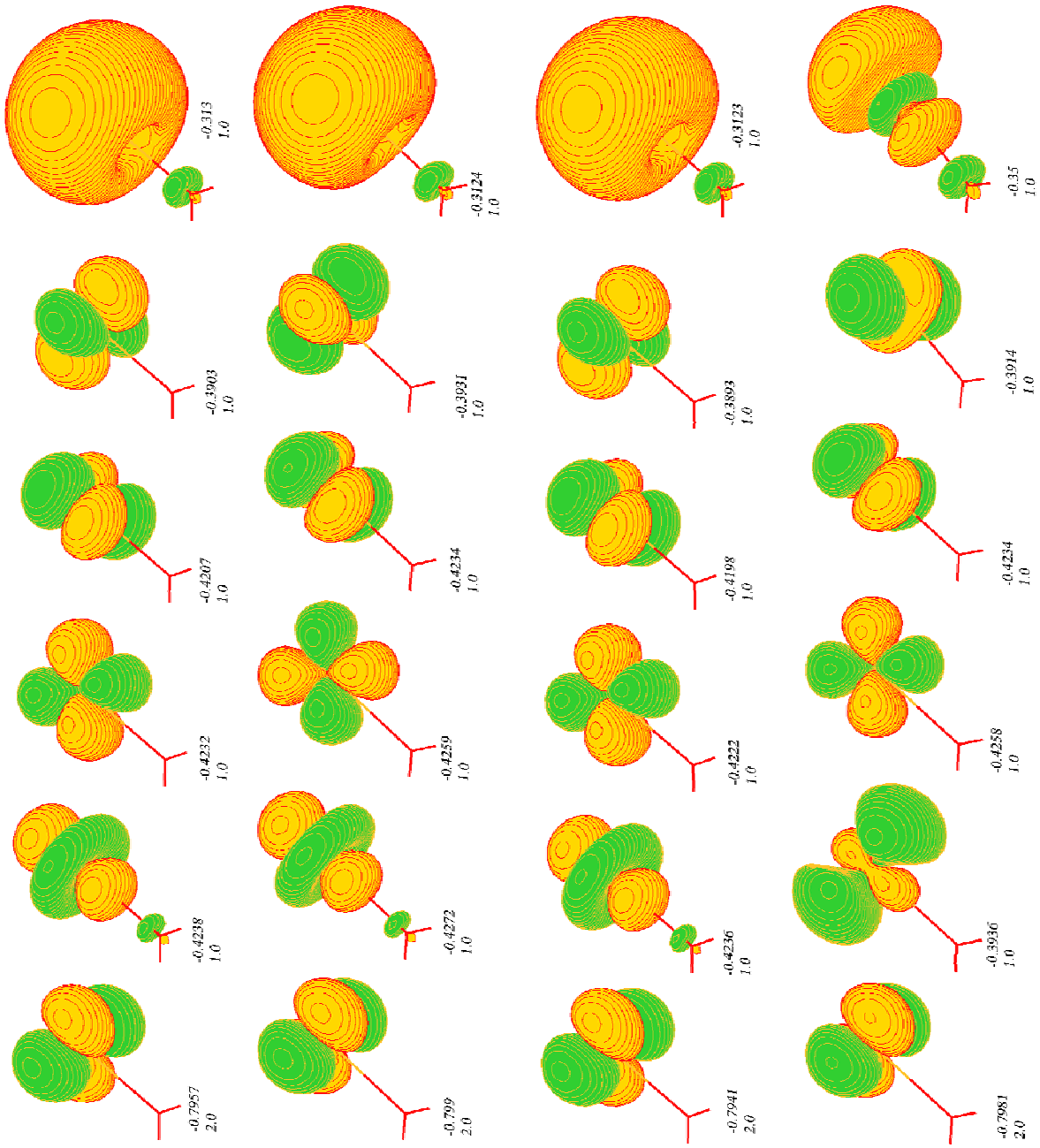

Figure 28. The ground state 3d/4s orbitals energy and occupation number of $^6A_2$ $Fe^+(H_2O)$ for (7, 6), (7, 9), (13, 9), and (13, 12) CASSCF calculations.

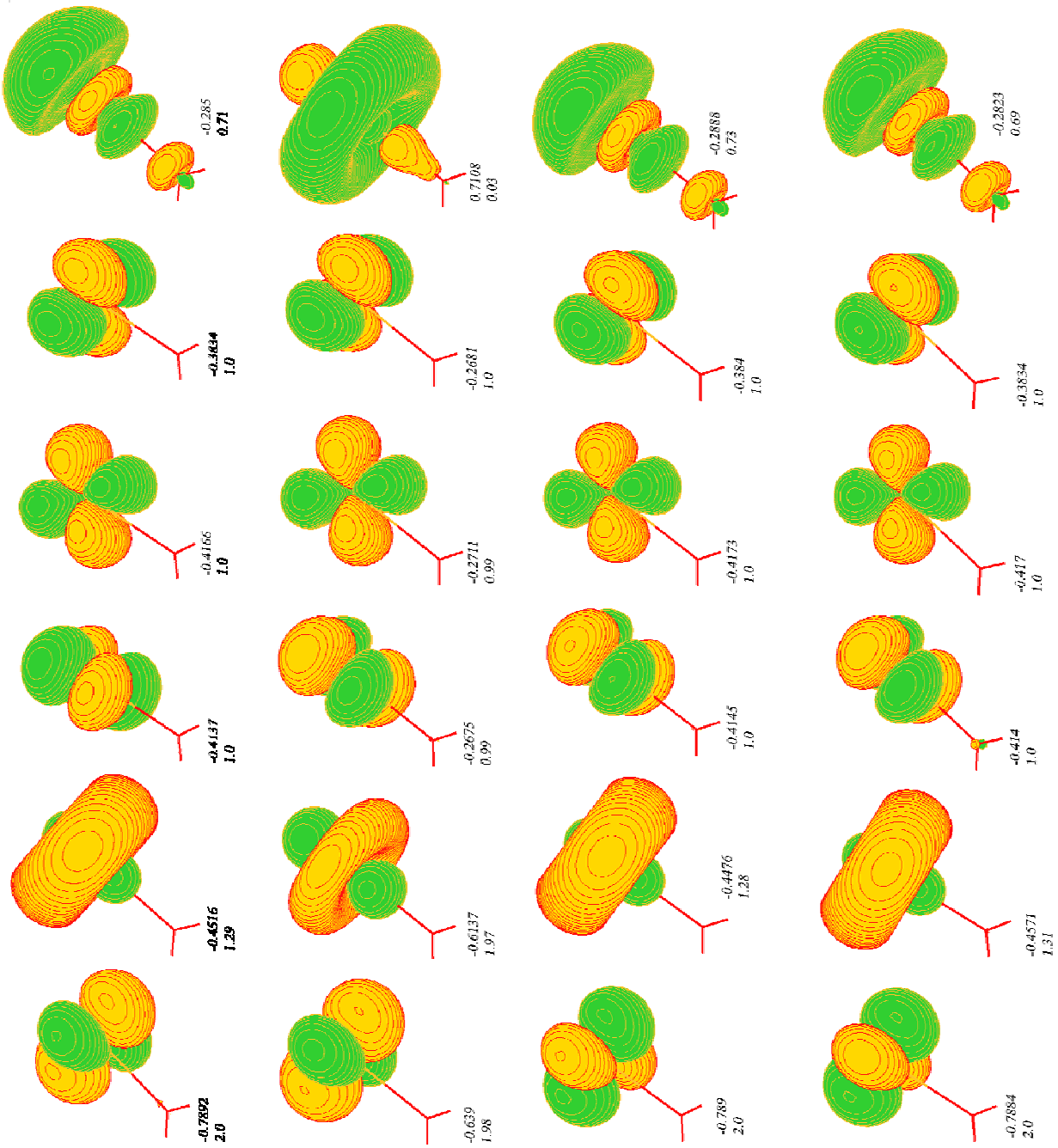

Figure 29. The ground state 3d/4s orbitals energy and occupation number of $^4A_1$ $Fe^+(H_2O)$ for (7, 6), (7, 9), (13, 9), and (13, 12) CASSCF calculations.

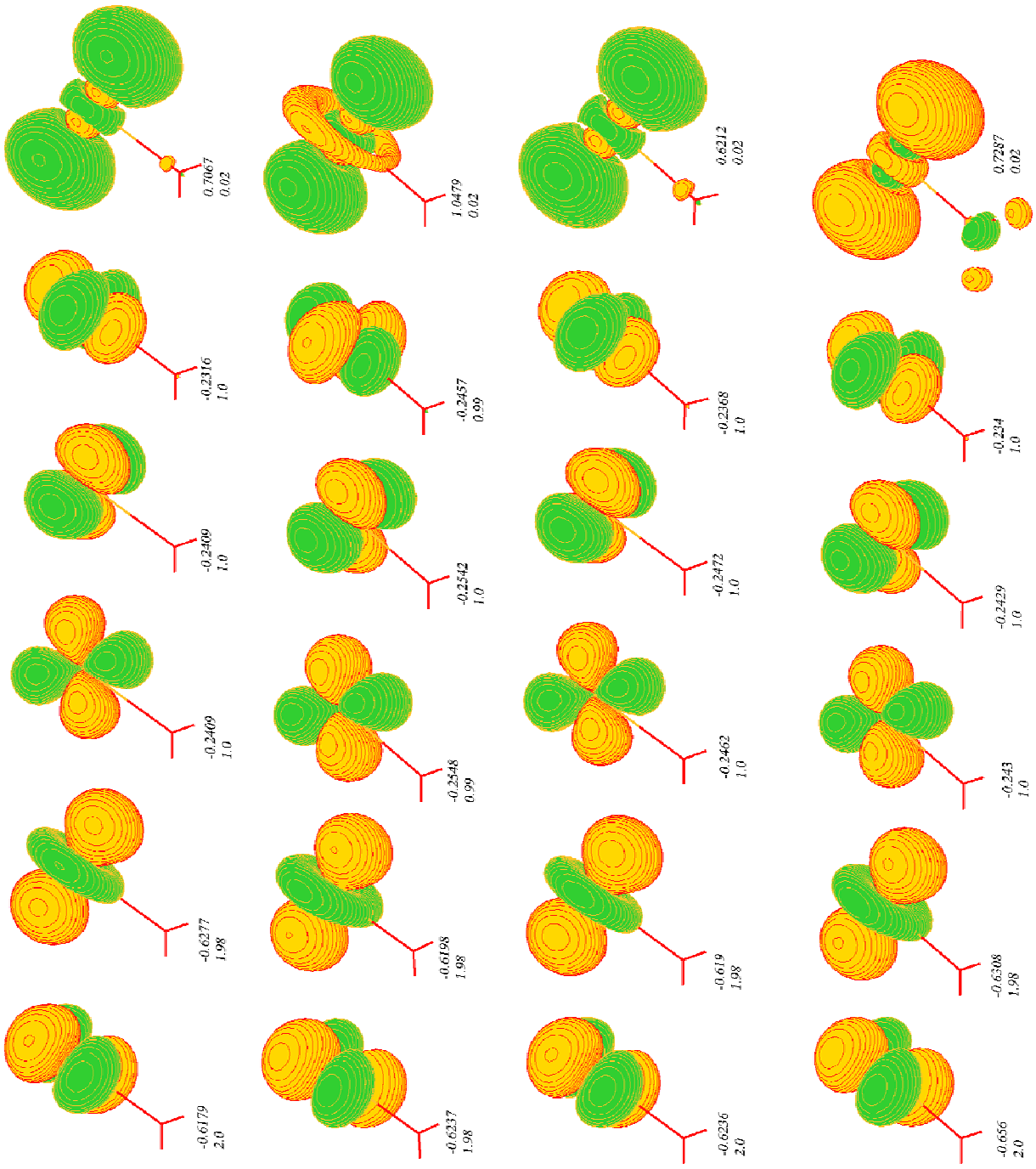

Figure 30. The ground state 3d/4s orbitals energy and occupation number of $^4B_1$ $Fe^+(H_2O)$ for (7, 6), (7, 9), (13, 9), and (13, 12) CASSCF calculations.

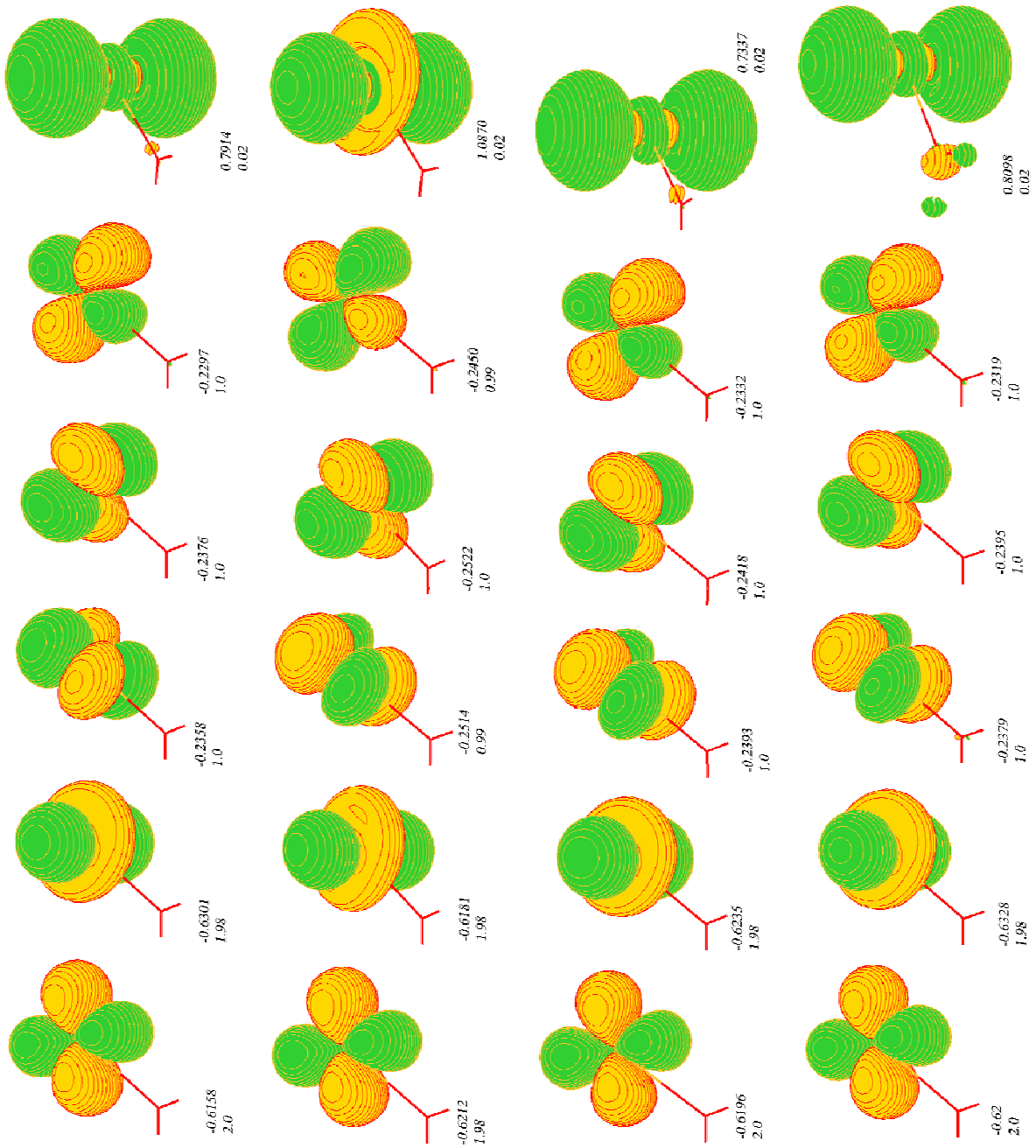

Figure 31. The ground state 3d/4s orbitals energy and occupation number of $^4B_2$ $Fe^+(H_2O)$ for (7, 6), (7, 9), (13, 9), and (13, 12) CASSCF calculations.

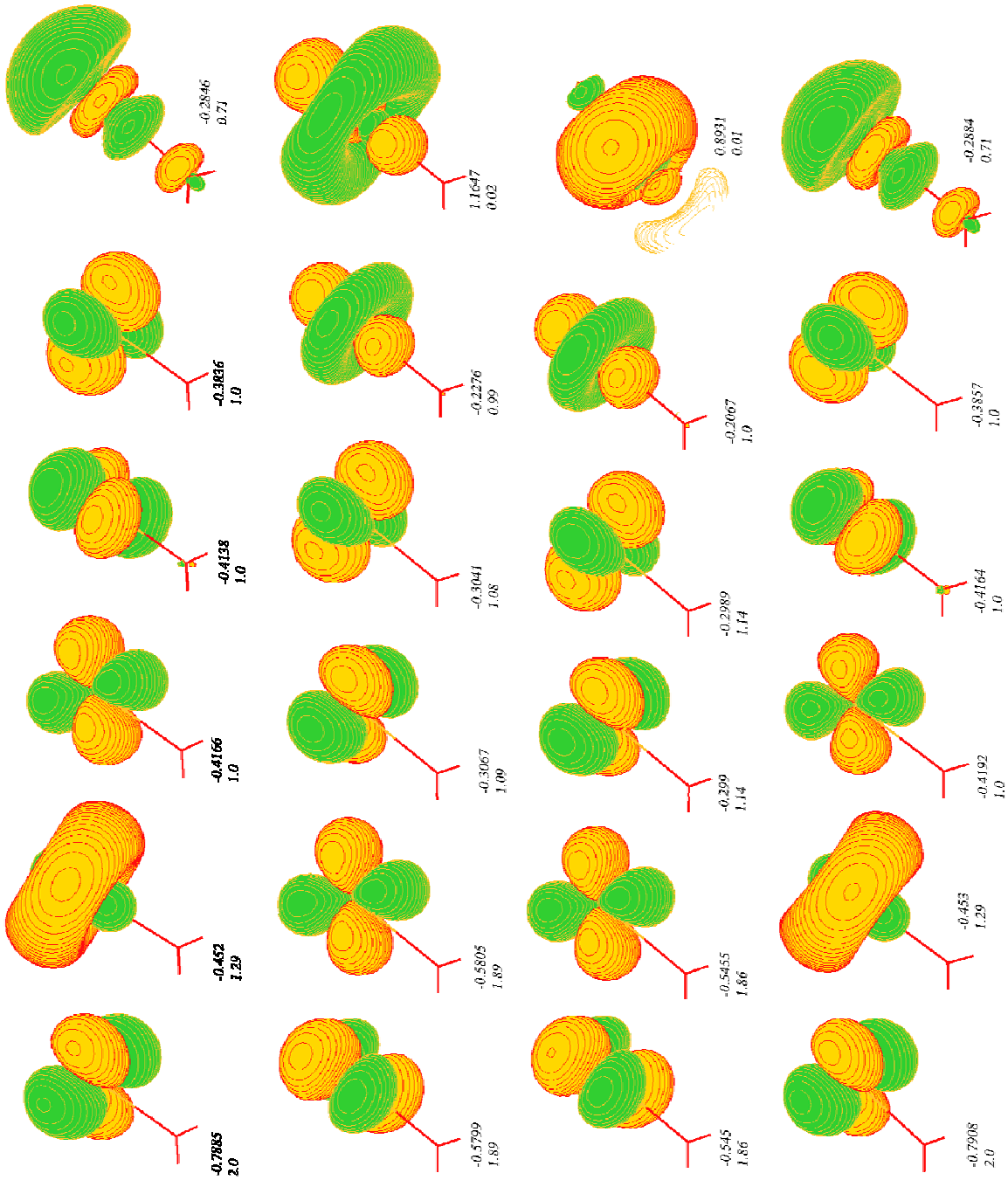

Figure 32. The ground state 3d/4s orbitals energy and occupation number of $^4A_2Fe^+(H_2O)$ for (7, 6), (7, 9), (13, 9), and (13, 12) CASSCF calculations.

Table 20. Orbital symmetry, occupation number, and orbital energy (in hartree) of $^6A_1$ $Fe^+(H_2O)$ for various CASSCF calculations.

(7,6)			(7,9)			(13,9)			(13,12)		
sym	**Occ**	**Energy**	**sym**	**Occ**	**Energy**	**sym**	**Occ**	**Energy**	**sym**	**Occ**	**Energy**
a1	2.000	-261.6138	a1	2.000	-261.6221	a1	2.000	-261.6107	a1	2.000	-261.6057
a1	2.000	-32.1740	a1	2.000	-32.1836	a1	2.000	-32.1416	a1	2.000	-32.1643
a1	2.000	-27.6643	a1	2.000	-27.6736	b1	2.000	-27.5780	a1	2.000	-27.5666
b1	2.000	-27.6481	b1	2.000	-27.6578	b2	2.000	-27.5776	b2	2.000	-27.5532
b2	2.000	-27.6474	b2	2.000	-27.6567	a1	2.000	-27.4056	b1	2.000	-27.5530
a1	2.000	-20.8369	a1	2.000	-20.8374	a1	2.000	-20.8364	a1	2.000	-20.8366
a1	2.000	-4.4075	a1	2.000	-4.4160	a1	2.000	-4.6093	a1	2.000	-4.3996
a1	2.000	-2.9898	a1	2.000	-2.9979	a1	1.997	-3.0491	a1	1.996	-3.0664
b1	2.000	-2.9807	b1	2.000	-2.9890	b1	1.998	-3.0457	b1	1.997	-3.0582
b2	2.000	-2.9803	b2	2.000	-2.9882	b2	1.998	-3.0453	b2	1.997	-3.0565
a1	2.000	-1.6346	a1	2.000	-1.6351	a1	2.000	-1.6444	a1	2.000	-1.6213
b2	2.000	-1.0009	b2	2.000	-1.0015	b2	2.000	-1.0005	b2	2.000	-0.9808
a1	2.000	-0.9055	a1	2.000	-0.9062	a1	2.000	-0.9116	a1	2.000	-0.9020
a1_3d	**2.000**	**-0.7956**	**a1_3d**	**1.990**	**-0.7966**	**a1_3d**	**2.000**	**-0.7974**	**a1_3d**	**1.995**	**-0.7895**
b1	2.000	-0.7924	b1	2.000	-0.7929	b1	2.000	-0.7920	b1	2.000	-0.7867
b2	**1.000**	**-0.4221**	**a1**	**1.000**	**-0.4330**	**a1**	**1.002**	**-0.4236**	**a1**	**1.003**	**-0.4194**
b1	**1.000**	**-0.4216**	**b1**	**0.997**	**-0.4287**	**b2**	**1.002**	**-0.4212**	**b1**	**1.002**	**-0.4166**
a1	**1.000**	**-0.3902**	**b2**	**0.997**	**-0.4280**	**b1**	**1.002**	**-0.4208**	**b2**	**1.002**	**-0.4163**
a2	**1.000**	**-0.3902**	**a2**	**1.000**	**-0.3979**	**a2**	**1.001**	**-0.3893**	**a2**	**1.001**	**-0.3843**
a1	**1.000**	**-0.3463**	**a1**	**1.000**	**-0.3116**	**a1**	**1.000**	**-0.3123**	**a1**	**1.000**	**-0.3121**
			a1_4d	0.010	1.3867				a1_4f	0.003	4.4961
			b2_4d	0.003	1.5711				b2_4f	0.003	4.5048
			b1_4d	0.003	1.5946				b1_4f	0.003	4.5114

a. The first section represents the inner shells, *i.e.* Fe_1s, Fe_2s, Fe_2p, w_1s, Fe_1s, Fe_3s orbitals. The second section represents Fe_3p orbitals. The last section represents all the other orbitals within the active space.

Table 21. Orbital symmetry, occupation number, and orbital energy (in hartree) of $^6B_1$ $Fe^+(H_2O)$ for various CASSCF calculations.

(7, 6)			(7, 9)			(13, 9)			(13, 12)		
sym	**Occ**	**Energy**	**sym**	**Occ**	**Energy**	**sym**	**Occ**	**Energy**	**sym**	**Occ**	**Energy**
a1	2.000	-261.6178	a1	2.000	-261.6262	a1	2.000	-261.6155	a1	2.000	-261.6209
a1	2.000	-32.1778	a1	2.000	-32.1876	a1	2.000	-32.1748	a1	2.000	-32.1808
b2	2.000	-27.6689	b2	2.000	-27.6782	b2	2.000	-27.5984	b2	2.000	-27.6719
b1	2.000	-27.6514	b1	2.000	-27.6610	a1	2.000	-27.5814	a1	2.000	-27.6539
a1	2.000	-27.6509	a1	2.000	-27.6607	b1	2.000	-26.6544	b1	2.000	-27.6474
a1	2.000	-20.8176	a1	2.000	-20.8181	a1	2.000	-20.8173	a1	2.000	-20.8087
a1	2.000	-4.4119	a1	2.000	-4.4208	a1	2.000	-4.4097	a1	2.000	-4.4148
b2	2.000	-2.9971	b2	2.000	-3.0053	b2	1.997	-3.0615	b2	2.000	-2.9998
b1	2.000	-2.9843	b1	2.000	-2.9912	b1	1.998	-3.0481	a1	2.000	-2.9850
a1	2.000	-2.9819	a1	2.000	-2.9902	a1	1.998	-3.0428	b1	2.000	-2.7043
a1	2.000	-1.6148	a1	2.000	-1.6153	**b1_3d**	**2.000**	**-1.6926**	a1	2.000	-1.3484
b2	2.000	-0.9817	b2	2.000	-0.9822	a1	2.000	-1.6150	a1	1.980	-1.1294
a1	2.000	-0.8792	a1	2.000	-0.8798	b2	2.000	-0.9815	**b1_3d**	**2.000**	**-1.0906**
b1_3d	**2.000**	**-0.8079**	**b1_3d**	**1.990**	**-0.7983**	a1	2.000	-0.8819	b2	1.978	-0.9616
b1_w2px	2.000	-0.7600	b1_w2px	2.000	-0.7727	b1_w2px	2.000	-0.8014	b1_w2px	1.983	-0.7616
a1	**1.000**	**-0.4391**	**a2**	**1.000**	**-0.4384**	**a1**	**1.002**	**-0.4396**	**a2**	**1.000**	**-0.4339**
a2	**1.000**	**-0.4313**	**b2**	**0.997**	**-0.4343**	**a2**	**1.002**	**-0.4302**	**b2**	**1.000**	**-0.4305**
b2	**1.000**	**-0.4276**	**a1**	**1.000**	**-0.4328**	**b2**	**1.002**	**-0.4265**	**a1**	**1.000**	**-0.4099**
a1	**1.000**	**-0.3843**	**a1**	**0.997**	**-0.3917**	**a1**	**1.001**	**-0.3826**	**a1**	**1.000**	**-0.4075**
a1	**1.000**	**-0.3204**	**a1**	**1.000**	**-0.3345**	**a1**	**1.000**	**-0.3194**	**a1**	**1.000**	**-0.3351**
			b1_4d	0.010	1.4439				a1_w3pz	0.021	0.6441
			b2_4d	0.003	1.5928				b2_w3py	0.021	0.6497
			a1_4d	0.004	1.6520				b1_w3px	0.017	0.8674

a. The first section represents the inner shells, *i.e.* Fe_1s, Fe_2s, Fe_2p, w_1s, Fe_1s, Fe_3s orbitals. The second section represents Fe_3p orbitals. The last section represents all the other orbitals within the active space.

Table 22. Orbital symmetry, occupation number, and orbital energy (in hartree) of $^6B_2$ $Fe^+(H_2O)$ for various CASSCF calculations.

(7, 6)			(7, 9)			(13, 9)			(13, 12)		
sym	**Occ**	**Energy**	**sym**	**Occ**	**Energy**	**sym**	**Occ**	**Energy**	**sym**	**Occ**	**Energy**
a1	2.000	-261.6165	a1	2.000	-261.6250	a1	2.000	-261.6142	a1	2.000	-261.6193
a1	2.000	-32.1767	a1	2.000	-32.1866	a1	2.000	-32.1738	a1	2.000	-32.1794
b1	2.000	-27.6677	b1	2.000	-27.6771	b1	2.000	-27.5972	b1	2.000	-27.6704
b2	2.000	-27.6504	b2	2.000	-27.6602	a1	2.000	-27.5803	a1	2.000	-27.6525
a1	2.000	-27.6497	a1	2.000	-27.6598	b2	2.000	-27.3389	b2	2.000	-27.6442
a1	2.000	-20.8244	a1	2.000	-20.8255	a1	2.000	-20.8242	a1	2.000	-20.8161
a1	2.000	-4.4106	a1	2.000	-4.4197	a1	2.000	-4.4085	a1	2.000	-4.4133
b1	2.000	-2.9954	b1	2.000	-3.0038	b1	1.997	-3.0598	b1	2.000	-2.9979
b2	2.000	-2.9835	b2	2.000	-2.9914	b2	1.998	-3.0475	a1	2.000	-2.9834
a1	2.000	-2.9807	a1	2.000	-2.9890	a1	1.998	-3.0407	b2	2.000	-2.0211
a1	2.000	-1.6214	a1	2.000	-1.6223	a1	2.000	-1.6217	**b2_3d**	**2.000**	**-1.7724**
b2	2.000	-0.9889	b2	2.000	-0.9891	**b2_3d**	**2.000**	**-1.0356**	a1	2.000	-1.3556
a1	2.000	-0.8877	a1	2.000	-0.8891	b2_w2py	2.000	-0.9880	a1	1.980	-1.1383
b2_3d	**2.000**	**-0.7941**	**b2**	**1.990**	**-0.7964**	a1	2.000	-0.8914	b2_w2py	1.978	-0.9676
b1	2.000	-0.7790	b1	2.000	-0.7801	b1	2.000	-0.7789	b1	1.982	-0.7712
a1	**1.000**	**-0.4370**	**a2**	**1.000**	**-0.4373**	**a1**	**1.002**	**-0.4378**	**a2**	**1.000**	**-0.4324**
a2	**1.000**	**-0.4301**	**a1**	**1.000**	**-0.4310**	**a2**	**1.002**	**-0.4291**	**b1**	**1.000**	**-0.4266**
b1	**1.000**	**-0.4239**	**b1**	**0.997**	**-0.4307**	**b1**	**1.002**	**-0.4230**	**a1**	**1.000**	**-0.4080**
a1	**1.000**	**-0.3828**	**a1**	**0.996**	**-0.3894**	**a1**	**1.001**	**-0.3811**	**a1**	**1.000**	**-0.4048**
a1	**1.000**	**-0.3181**	**a1**	**1.000**	**-0.3327**	**a1**	**1.000**	**-0.3171**	**a1**	**1.000**	**-0.3331**
			b2_4d	0.010	1.4133				a1_w3pz	0.021	0.6404
			b1_4d	0.003	1.6071				b2_w3py	0.021	0.6470
			a1_4d	0.004	1.6442				b1_w3px	0.017	0.8587

a. The first section represents the inner shells, *i.e.* Fe_1s, Fe_2s, Fe_2p, w_1s, Fe_1s, Fe_3s orbitals. The second section represents Fe_3p orbitals. The last section represents all the other orbitals within the active space.

Table 23. Orbital symmetry, occupation number, and orbital energy (in hartree) of $^6A_2$ $Fe^+(H_2O)$ for various CASSCF calculations.

(7, 6)			(7, 9)			(13, 9)			(13, 12)		
sym	**Occ**	**Energy**	**sym**	**Occ**	**Energy**	**sym**	**Occ**	**Energy**	**sym**	**Occ**	**Energy**
a1	2.000	-261.6139	a1	2.000	-261.6177	a1	2.000	-261.612	a1	2.000	-261.617
a1	2.000	-32.1741	a1	2.000	-32.1785	a1	2.000	-32.1712	a1	2.000	-32.1767
a1	2.000	-27.6644	a1	2.000	-27.6689	a1	2.000	-27.5941	a1	2.000	-27.6671
b2	2.000	-27.6479	b2	2.000	-27.6521	b2	2.000	-27.5778	b2	2.000	-27.6505
b1	2.000	-27.6478	b1	2.000	-27.6520	b1	2.000	-27.5776	b1	2.000	-27.6504
a1	2.000	-20.8367	a1	2.000	-20.8372	a1	2.000	-20.8363	a1	2.000	-20.828
a1	2.000	-4.4076	a1	2.000	-4.4114	a1	2.000	-4.4055	a1	2.000	-4.4102
a1	2.000	-2.9899	a1	2.000	-2.9934	a1	1.997	-3.0492	a1	2.000	-2.9926
b2	2.000	-2.9808	b2	2.000	-2.9842	b2	1.998	-3.0458	b2	2.000	-2.9833
b1	2.000	-2.9803	b1	2.000	-2.9838	b1	1.998	-3.0453	b1	2.000	-2.9828
a1	2.000	-1.6343	a1	2.000	-1.6347	a1	2.000	-1.6346	a1	2.000	-1.368
b2	2.000	-1.0007	b2	2.000	-1.0012	b2	2.000	-1.0004	a1	1.980	-1.1555
a1	2.000	-0.9050	a1	2.000	-0.9057	a1	2.000	-0.9092	b2	1.979	-0.9812
a2	**2.000**	**-0.7957**	**a2**	**1.999**	**-0.7990**	**a2**	**2.000**	**-0.7941**	**a2**	**2.000**	**-0.7981**
b1	2.000	-0.7921	b1	2.000	-0.7926	b1	2.000	-0.7920	b1	1.983	-0.7841
b2	**1.000**	**-0.4232**	**a1**	**0.998**	**-0.4272**	**a1**	**1.002**	**-0.4236**	**b2**	**1.000**	**-0.4258**
b1	**1.000**	**-0.4207**	**b2**	**0.998**	**-0.4259**	**b2**	**1.002**	**-0.4222**	**b1**	**1.000**	**-0.4234**
a1	**1.000**	**-0.4129**	**b1**	**0.998**	**-0.4234**	**b1**	**1.002**	**-0.4198**	**a1**	**1.000**	**-0.3936**
a1	**1.000**	**-0.4003**	**a1**	**1.000**	**-0.3931**	**a1**	**1.001**	**-0.3893**	**a1**	**1.000**	**-0.3914**
a1	**1.000**	**-0.3138**	**a1**	**1.000**	**-0.3124**	**a1**	**1.000**	**-0.3123**	**a1**	**1.000**	**-0.3500**
			b2_4d	0.002	1.6183				a1_w3pz	0.021	0.6362
			b1_4d	0.002	1.6382				b2_w3py	0.021	0.6426
			a1_4d	0.003	1.6834				b1_w3px	0.017	0.8611

a. The first section represents the inner shells, *i.e.* Fe_1s, Fe_2s, Fe_2p, w_1s, Fe_1s, Fe_3s orbitals. The second section represents Fe_3p orbitals. The last section represents all the other orbitals within the active space.

Table 24. Orbital symmetry, occupation number, and orbital energy (in hartree) of $^4A_1$ $Fe^+(H_2O)$ for various CASSCF calculations.

(7, 6)			(7, 9)			(13, 9)			(13, 12)		
sym	**Occ**	**Energy**	**sym**	**Occ**	**Energy**	**sym**	**Occ**	**Energy**	**sym**	**Occ**	**Energy**
a1	2.000	-261.6048	a1	2.000	-261.4590	a1	2.000	-261.604	a1	2.000	-261.6052
a1	2.000	-32.1611	a1	2.000	-31.9982	a1	2.000	-32.1595	a1	2.000	-32.1616
a1	2.000	-27.6494	b2	2.000	-27.4827	a1	2.000	-27.5786	a1	2.000	-27.6502
b2	2.000	-27.6372	b1	2.000	-27.4820	b2	2.000	-27.5682	b2	2.000	-27.6374
b1	2.000	-27.6371	a1	2.000	-27.4786	b1	2.000	-27.5681	b1	2.000	-27.6373
a1	2.000	-20.8452	a1	2.000	-20.8143	a1	2.000	-20.8453	a1	2.000	-20.7802
a1	2.000	-4.1615	a1	2.000	-4.2367	a1	2.000	-4.0537	a1	2.000	-4.3991
a1	2.000	-2.9833	a1	2.000	-2.8344	a1	1.997	-3.0467	a1	2.000	-2.9855
b2	2.000	-2.9727	b2	2.000	-2.8290	b2	1.998	-3.0402	b2	2.000	-2.9727
b1	2.000	-2.9723	b1	2.000	-2.8285	b1	1.998	-3.0393	b1	2.000	-2.9722
a1	2.000	-1.5893	a1	2.000	-1.6102	a1	2.000	-1.5847	a1	1.998	-1.4553
a1	2.000	-1.2102	b2	2.000	-0.9785	a1	2.000	-1.3292	a1	1.980	-1.1511
b2	2.000	-1.0102	a1	2.000	-0.8683	b2	2.000	-1.0104	b2	1.979	-0.9921
b1	2.000	-0.8015	b1	2.000	-0.7682	b1	2.000	-0.8023	b1	1.982	-0.7952
a1	**2.000**	**-0.7892**	**a1**	**1.981**	**-0.6390**	**a1**	**2.000**	**-0.7890**	**a1**	**2.000**	**-0.7884**
a1	**1.291**	**-0.4516**	**a1**	**1.975**	**-0.6137**	**a1**	**1.275**	**-0.4476**	**a1**	**1.309**	**-0.4571**
b2	**1.000**	**-0.4166**	**b2**	**0.993**	**-0.2711**	**b2**	**1.002**	**-0.4173**	**b2**	**1.000**	**-0.4170**
b1	**1.000**	**-0.4137**	**a2**	**1.000**	**-0.2681**	**b1**	**1.002**	**-0.4145**	**b1**	**1.000**	**-0.4140**
a2	**1.000**	**-0.3834**	**b1**	**0.993**	**-0.2675**	**a2**	**1.001**	**-0.3840**	**a2**	**1.000**	**-0.3834**
a1_3d/4s	0.710	-0.2850	a1_4d/4s	0.026	0.7108	a1_3d/4s	0.727	-0.2888	a1_3d/4s	0.692	-0.2823
			a1_4d	0.018	1.1164				b2_w3py	0.022	0.6268
			b2_4d	0.007	1.2864				a1_w3pz	0.021	0.6371
			b1_4d	0.007	1.3207				b1_w3px	0.017	0.8493

a. The first section represents the inner shells, *i.e.* Fe_1s, Fe_2s, Fe_2p, w_1s, Fe_1s, Fe_3s orbitals. The second section represents Fe_3p orbitals. The last section represents all the other orbitals within the active space.

Table 25. Orbital symmetry, occupation number, and orbital energy (in hartree) of $^4B_1$ $Fe^+(H_2O)$ for various CASSCF calculations.

(7, 6)			(7, 9)			(13, 9)			(13, 12)		
sym	**Occ**	**Energy**	**sym**	**Occ**	**Energy**	**sym**	**Occ**	**Energy**	**sym**	**Occ**	**Energy**
a1	2.000	-261.4259	a1	2.000	-261.4403	a1	2.000	-261.432	a1	2.000	-261.4280
a1	2.000	-31.9592	a1	2.000	-31.9764	a1	2.000	-31.9662	a1	2.000	-31.9611
b2	2.000	-27.4469	b2	2.000	-27.4622	b1	2.000	-27.3509	b2	2.000	-27.4487
b1	2.000	-27.4417	a1	2.000	-27.4588	a1	2.000	-27.3456	b1	2.000	-27.4436
a1	2.000	-27.4414	b1	2.000	-27.4585	b2	2.000	-27.3134	a1	2.000	-27.4434
a1	2.000	-20.7991	a1	2.000	-20.8022	a1	2.000	-20.8011	a1	2.000	-20.7922
a1	2.000	-4.1775	a1	2.000	-4.2196	a1	2.000	-4.1893	a1	2.000	-4.1792
a1	2.000	-2.7962	a1	2.000	-2.8127	b2	1.998	-2.9405	a1	2.000	-2.7984
b1	2.000	-2.7962	b2	2.000	-2.8114	b1	1.999	-2.8994	b2	2.000	-2.7968
b2	2.000	-2.7947	b1	2.000	-2.8103	a1	1.999	-2.8973	b1	2.000	-2.7665
a1	2.000	-1.5959	a1	2.000	-1.5988	a1	2.000	-1.5986	a1	2.000	-1.3262
b2	2.000	-0.9642	b2	2.000	-0.9672	b2	2.000	-0.9668	a1	1.980	-1.1105
a1	2.000	-0.8523	a1	2.000	-0.8562	a1	2.000	-0.8606	b2	1.978	-0.9458
b1	2.000	-0.7539	b1	2.000	-0.7567	b1	2.000	-0.7563	b1	1.983	-0.7432
b1	**2.000**	**-0.6179**	**b1**	**1.982**	**-0.6237**	**b1**	**2.000**	**-0.6236**	**b1**	**2.000**	**-0.6560**
a1	**1.982**	**-0.6277**	**a1**	**1.981**	**-0.6198**	**a1**	**1.979**	**-0.6190**	**a1**	**1.983**	**-0.6308**
b2	**1.000**	**-0.2409**	**a2**	**1.001**	**-0.2542**	**a2**	**1.001**	**-0.2472**	**b2**	**1.000**	**-0.2430**
a2	**1.000**	**-0.2409**	**b2**	**0.994**	**-0.2548**	**b2**	**1.001**	**-0.2462**	**a2**	**1.000**	**-0.2429**
a1	**1.000**	**-0.2316**	**a1**	**0.993**	**-0.2457**	**a1**	**1.001**	**-0.2368**	**a1**	**1.000**	**-0.2340**
a1_3d/4s	0.018	0.7067	a1_4d/4s	0.019	1.0479	a1_3d/4s	0.023	0.6212	a1_3d/4s	0.022	0.6515
			b1_4d	0.017	1.1917				b2_w3py	0.021	0.665
			a1_4d	0.007	1.2705				a1_w3pz	0.017	0.7287
			b2_4d	0.007	1.3485				b1_w3px	0.017	0.8766

a. The first section represents the inner shells, *i.e.* Fe_1s, Fe_2s, Fe_2p, w_1s, Fe_1s, Fe_3s orbitals. The second section represents Fe_3p orbitals. The last section represents all the other orbitals within the active space.

Table 26. Orbital symmetry, occupation number, and orbital energy (in hartree) of $^4B_2$ $Fe^+(H_2O)$ for various CASSCF calculations.

(7, 6)			(7, 9)			(13, 9)			(13, 12)		
sym	**Occ**	**Energy**	**sym**	**Occ**	**Energy**	**sym**	**Occ**	**Energy**	**sym**	**Occ**	**Energy**
a1	2.000	-261.4231	a1	2.000	-261.4391	a1	2.000	-261.427	a1	2.000	-261.425
a1	2.000	-31.9562	a1	2.000	-31.9754	a1	2.000	-31.9608	a1	2.000	-31.9581
b1	2.000	-27.4433	b1	2.000	-27.4604	b2	2.000	-27.3414	b1	2.000	-27.4451
a1	2.000	-27.4390	a1	2.000	-27.4582	a1	2.000	-27.3395	a1	2.000	-27.441
b2	2.000	-27.4390	b2	2.000	-27.4575	b1	2.000	-27.2963	b2	2.000	-27.4409
a1	2.000	-20.8025	a1	2.000	-20.8062	a1	2.000	-20.8038	a1	2.000	-20.7958
a1	2.000	-4.1722	a1	2.000	-4.2195	a1	2.000	-4.1804	a1	2.000	-4.1739
a1	2.000	-2.7936	a1	2.000	-2.8118	b1	1.999	-2.9444	a1	2.000	-2.7957
b2	2.000	-2.7936	b2	2.000	-2.8103	b2	1.999	-2.8993	b2	2.000	-2.7953
b1	2.000	-2.7915	b1	2.000	-2.8098	a1	1.999	-2.8933	b1	2.000	-2.7935
a1	2.000	-1.5988	a1	2.000	-1.6022	a1	2.000	-1.601	a1	2.000	-1.3296
b2	2.000	-0.9668	B2	2.000	-0.9703	b2	2.000	-0.9683	a1	1.980	-1.1148
a1	2.000	-0.8565	A1	2.000	-0.8613	a1	2.000	-0.865	b2	1.978	-0.9468
b1	2.000	-0.7560	B1	2.000	-0.7597	b1	2.000	-0.7598	b1	1.982	-0.7499
b2	**2.000**	**-0.6158**	**B2**	**1.981**	**-0.6212**	**a1**	**1.982**	**-0.6235**	**a1**	**1.984**	**-0.6328**
a1	**1.984**	**-0.6301**	**A1**	**1.981**	**-0.6181**	**b2**	**2.000**	**-0.6196**	**b2**	**2.000**	**-0.6200**
b1	**1.000**	**-0.2358**	**A2**	**1.001**	**-0.2522**	**a2**	**1.001**	**-0.2418**	**a2**	**1.000**	**-0.2395**
a2	**1.000**	**-0.2376**	**B1**	**0.995**	**-0.2514**	**b1**	**1.001**	**-0.2393**	**b1**	**1.000**	**-0.2379**
a1	**1.000**	**-0.2297**	**A1**	**0.993**	**-0.2450**	**a1**	**1.001**	**-0.2332**	**a1**	**1.000**	**-0.2319**
a1_3d/4s	0.016	0.7914	a1_4d/4s	0.018	1.0870	a1_3d/4s	0.019	0.7337	a1_3d/4s	0.022	0.6494
			b2_4d	0.017	1.1623				b2_w3py	0.021	0.6630
			a1_4d	0.007	1.2354				a1_w3pz	0.015	0.8098
			b1_4d	0.007	1.3802				b1_w3px	0.017	0.8821

a. The first section represents the inner shells, *i.e.* Fe_1s, Fe_2s, Fe_2p, w_1s, Fe_1s, Fe_3s orbitals. The second section represents Fe_3p orbitals. The last section represents all the other orbitals within the active space.

Table 27. Orbital symmetry, occupation number, and orbital energy (in hartree) of $^4A_2$ $Fe^+(H_2O)$ for various CASSCF calculations.

(7, 6)			(7, 9)			(13, 9)			(13, 12)		
sym	**Occ**	**Energy**	**sym**	**Occ**	**Energy**	**sym**	**Occ**	**Energy**	**sym**	**Occ**	**Energy**
a1	2.000	-261.6049	a1	2.000	-261.4394	a1	2.000	-261.4125	a1	2.000	-261.6074
a1	2.000	-32.1615	a1	2.000	-31.9756	a1	2.000	-31.9444	a1	2.000	-32.1640
a1	2.000	-27.6501	b2	2.000	-27.4635	a1	2.000	-27.4210	a1	2.000	-27.6527
b2	2.000	-27.6373	b1	2.000	-27.4632	b1	2.000	-27.3705	b2	2.000	-27.6398
b1	2.000	-27.6371	a1	2.000	-27.4500	b2	2.000	-27.3705	b1	2.000	-27.6395
a1	2.000	-20.8451	a1	2.000	-20.7986	a1	2.000	-20.7918	a1	2.000	-20.8373
a1	2.000	-4.3992	a1	2.000	-4.2211	a1	2.000	-4.1901	a1	2.000	-4.4017
a1	2.000	-2.9857	b2	2.000	-2.8139	b2	1.999	-2.8456	a1	2.000	-2.9882
b2	2.000	-2.9727	b1	2.000	-2.8134	b1	1.999	-2.8451	b2	2.000	-2.9751
b1	2.000	-2.9725	a1	2.000	-2.8054	a1	2.000	-2.7770	b1	2.000	-2.9748
a1	2.000	-1.6430	a1	2.000	-1.5947	a1	2.000	-1.5180	a1	2.000	-1.3773
b2	2.000	-1.0101	b2	2.000	-0.9631	b2	2.000	-0.9609	a1	1.980	-1.1681
a1	2.000	-0.9162	a1	2.000	-0.8514	a1	1.990	-0.9164	b2	1.979	-0.9917
b1	2.000	-0.8015	b1	2.000	-0.7527	b1	2.000	-0.7491	b1	1.983	-0.7944
a2	**2.000**	**-0.7885**	**b2**	**1.893**	**-0.5805**	**b2**	**1.856**	**-0.5455**	**a2**	**2.000**	**-0.7908**
a1	**1.292**	**-0.4520**	**b1**	**1.894**	**-0.5799**	**b1**	**1.856**	**-0.5450**	**a1**	**1.287**	**-0.4530**
b2	**1.000**	**-0.4166**	**a2**	**1.090**	**-0.3067**	**a2**	**1.144**	**-0.2990**	**b2**	**1.000**	**-0.4192**
b1	**1.000**	**-0.4138**	**a1**	**1.083**	**-0.3041**	**a1**	**1.144**	**-0.2989**	**b1**	**1.000**	**-0.4164**
a1	**1.000**	**-0.3836**	**a1**	**0.993**	**-0.2276**	**a1**	**1.000**	**-0.2067**	**a1**	**1.000**	**-0.3857**
a1_3d/4s	0.708	-0.2846	a1_4d/4s	0.008	1.1647	a1_3d/4s	0.011	0.8931	a1_3d/4s	0.713	-0.2884
			b2_4d	0.016	1.1783				a1_w3pz	0.021	0.6354
			b1_4d	0.016	1.2093				b2_w3py	0.021	0.6428
			a1_4d	0.007	1.3124				b1_w3px	0.017	0.8634

a. The first section represents the inner shells, *i.e.* Fe_1s, Fe_2s, Fe_2p, w_1s, Fe_1s, Fe_3s orbitals. The second section represents Fe_3p orbitals. The last section represents all the other orbitals within the active space.

Table 28. Orbital symmetry, occupation number, and orbital energy (in hartree) of $^6A_1$ $Fe^+(H_2O)Ar$ where argon atom is bound to Fe^+ for various CASSCF calculations.

(7, 6)			(13, 12)			(19, 15)		
sym	Occ	Energy	sym	Occ	Energy	sym	Occ	Energy
a1	2.000	-261.6127	a1	2.000	-261.6116	a1	2.000	-261.6113
a1	2.000	-118.7043	a1	2.000	-118.7045	a1	2.000	-118.7045
a1	2.000	-32.1728	a1	2.000	-32.1718	a1	2.000	-32.0314
a1	2.000	-27.6632	a1	2.000	-27.5703	a1	2.000	-27.5680
b1	2.000	-27.6470	b1	2.000	-27.5211	b2	2.000	-27.3844
b2	2.000	-27.6463	b2	2.000	-27.5114	b1	2.000	-27.0485
a1	2.000	-20.8353	a1	2.000	-20.8352	a1	2.000	-20.8351
a1	2.000	-12.4154	a1	2.000	-12.4155	a1	2.000	-12.4156
a1	2.000	-9.6644	a1	2.000	-9.6645	a1	2.000	-9.6646
b2	2.000	-9.6644	b2	2.000	-9.6645	b2	2.000	-9.6645
b1	2.000	-9.6644	b1	2.000	-9.6645	b1	2.000	-9.6645
a1	2.000	-4.4064	a1	2.000	-4.4055	a1	2.000	-4.4975
a1	2.000	-2.9887	b2	1.997	-3.1116	b2	1.997	-3.1083
b1	2.000	-2.9795	b1	1.997	-3.1033	b1	1.996	-3.1028
b2	2.000	-2.9792	a1	1.996	-3.0757	a1	1.996	-3.0758
a1	2.000	-1.6329	a1	2.000	-1.6334	a1	2.000	-1.6349
a1	2.000	-1.3701	a1	2.000	-1.3702	a1	2.000	-1.3702
b2	2.000	-0.9994	b2	2.000	-0.9995	b1	2.000	-1.2633
a1	2.000	-0.9034	a1	2.000	-0.9064	b2	2.000	-1.1293
a1	**2.000**	**-0.7944**	b1	2.000	-0.7912	a1	2.000	-0.9544
b1	2.000	-0.7907	**a1**	**1.990**	**-0.7876**	**a1**	**1.990**	**-0.7867**
a1	2.000	-0.6844	a1	2.000	-0.6845	a1	2.000	-0.6846
b2	2.000	-0.6831	b2	2.000	-0.6833	b2	2.000	-0.6833
b1	2.000	-0.6831	b1	2.000	-0.6833	b1	2.000	-0.6833
b2	**1.000**	**-0.4209**	**a1**	**1.003**	**-0.4250**	**a1**	**1.003**	**-0.4245**
b1	**1.000**	**-0.4205**	**b1**	**1.002**	**-0.4218**	**b1**	**1.002**	**-0.4212**
a1	**1.000**	**-0.4164**	**b2**	**1.002**	**-0.4211**	**b2**	**1.002**	**-0.4212**
a2	**1.000**	**-0.3890**	**a2**	**1.001**	**-0.3899**	**a2**	**1.001**	**-0.3896**
a1	**1.000**	**-0.3178**	**a1**	**1.000**	**-0.3102**	**a1**	**1.000**	**-0.3104**
			a1	0.008	1.2050	a1	0.008	1.2586
			b1	0.003	4.5896	b1	0.003	4.7826
			b2	0.003	4.6483	b2	0.003	4.8101

a. Thefirst section represents the inner shells, *i.e.* Fe_1s, Ar_1s, Fe_2s, Fe_2p, w_1s, Ar_2s, Ar_2p, Fe_3s orbitals. The second section represents Fe_3p orbitals. The third section represents w_2s, Ar_3s orbitals. The last section represents all the other orbitals within the active space.

Table 29. Orbital symmetry, occupation number, and orbital energy (in hartree) of $^6B_1$ $Fe^+(H_2O)Ar$ where argon atom is bound to Fe^+ for various CASSCF calculations.

(7, 6)			(13, 12)			(19, 15)		
sym	Occ	Energy	sym	Occ	Energy	sym	Occ	Energy
a1	2.000	-261.6164	a1	2.000	-261.6153	a1	2.000	-261.6149
a1	2.000	-118.7074	a1	2.000	-118.7072	a1	2.000	-118.7072
a1	2.000	-32.1764	a1	2.000	-32.1752	a1	2.000	-32.0543
b2	2.000	-27.6675	b2	2.000	-27.5773	b2	2.000	-27.5784
b1	2.000	-27.6500	b1	2.000	-27.5352	a1	2.000	-27.5119
a1	2.000	-27.6495	a1	2.000	-27.5165	b1	2.000	-27.0725
a1	2.000	-20.8163	a1	2.000	-20.8167	a1	2.000	-20.8166
a1	2.000	-12.4185	a1	2.000	-12.4183	a1	2.000	-12.4183
a1	2.000	-9.6675	a1	2.000	-9.6672	a1	2.000	-9.6673
b2	2.000	-9.6674	b2	2.000	-9.6672	b2	2.000	-9.6672
b1	2.000	-9.6674	b1	2.000	-9.6672	b1	2.000	-9.6672
a1	2.000	-4.4105	a1	2.000	-4.4085	a1	2.000	-4.5220
b2	2.000	-2.9956	a1	1.997	-3.1073	a1	1.997	-3.1113
b1	2.000	-2.9829	b2	1.996	-3.0827	b2	1.996	-3.0805
a1	2.000	-2.9805	b1	1.997	-3.0559	b1	1.996	-3.0382
a1	2.000	-1.6136	a1	2.000	-1.6145	a1	2.000	-1.6146
a1	2.000	-1.3731	a1	2.000	-1.3729	a1	2.000	-1.3729
b2	2.000	-0.9804	b2	2.000	-0.9809	b1	2.000	-1.2350
a1	2.000	-0.8777	a1	2.000	-0.8842	b2	2.000	-0.9810
b1	**2.000**	**-0.8064**	**b1**	**1.992**	**-0.8266**	a1	2.000	-0.8900
b1	2.000	-0.7588	b1	2.000	-0.7714	**b1**	**1.992**	**-0.8420**
a1	2.000	-0.6875	a1	2.000	-0.6873	a1	2.000	-0.6873
b2	2.000	-0.6862	b2	2.000	-0.6859	b2	2.000	-0.6860
b1	2.000	-0.6861	b1	2.000	-0.6859	b1	2.000	-0.6860
a1	**1.000**	**-0.4338**	**a1**	**1.002**	**-0.4352**	**a1**	**1.003**	**-0.4365**
a2	**1.000**	**-0.4298**	**a2**	**1.002**	**-0.4300**	**a2**	**1.002**	**-0.4297**
b2	**1.000**	**-0.4261**	**b2**	**1.002**	**-0.4267**	**b2**	**1.002**	**-0.4264**
a1	**1.000**	**-0.3834**	**a1**	**1.001**	**-0.3859**	**a1**	**1.001**	**-0.3845**
a1	**1.000**	**-0.3222**	**a1**	**1.000**	**-0.3194**	**a1**	**1.000**	**-0.3189**
			b1	0.008	1.2551	b1	0.008	1.2886
			a1	0.003	4.4476	a1	0.003	4.6661
			b2	0.002	4.6282	b2	0.002	4.8413

a. Thefirst section represents the inner shells, *i.e.* Fe_1s, Ar_1s, Fe_2s, Fe_2p, w_1s, Ar_2s, Ar_2p, Fe_3s orbitals. The second section represents Fe_3p orbitals. The third section represents w_2s, Ar_3s orbitals. The last section represents all the other orbitals within the active space.

Table 30. Orbital symmetry, occupation number, and orbital energy (in hartree) of $^6B_2$ $Fe^+(H_2O)Ar$ where argon atom is bound to Fe^+ for various CASSCF calculations.

(7, 6)			(13, 12)			(19, 15)		
sym	Occ	Energy	sym	Occ	Energy	sym	Occ	Energy
a1	2.000	-261.6153	a1	2.000	-261.6157	a1	2.000	-261.6157
a1	2.000	-118.7061	a1	2.000	-118.7056	a1	2.000	-118.7057
a1	2.000	-32.1754	a1	2.000	-32.1760	a1	2.000	-32.0296
b1	2.000	-27.6664	b1	2.000	-27.5849	b1	2.000	-27.5903
b2	2.000	-27.6492	b2	2.000	-27.5434	a1	2.000	-27.5285
a1	2.000	-27.6485	a1	2.000	-27.5272	b2	2.000	-27.4840
a1	2.000	-20.8231	a1	2.000	-20.8247	a1	2.000	-20.8244
a1	2.000	-12.4171	a1	2.000	-12.4167	a1	2.000	-12.4167
a1	2.000	-9.6661	a1	2.000	-9.6657	a1	2.000	-9.6657
b1	2.000	-9.6661	b1	2.000	-9.6656	b1	2.000	-9.6657
b2	2.000	-9.6661	b2	2.000	-9.6656	b2	2.000	-9.6657
a1	2.000	-4.4093	a1	2.000	-4.4082	a1	2.000	-4.5434
b1	2.000	-2.9941	a1	1.997	-3.0966	a1	1.997	-3.0933
b2	2.000	-2.9822	b2	1.997	-3.0848	b2	1.997	-3.0805
a1	2.000	-2.9794	b1	1.996	-3.0746	b1	1.995	-3.0657
a1	2.000	-1.6201	a1	2.000	-1.6223	a1	2.000	-1.6225
a1	2.000	-1.3718	a1	2.000	-1.3713	a1	2.000	-1.3714
b2	2.000	-0.9876	b2	2.000	-0.9884	b2	2.000	-1.0522
a1	2.000	-0.8862	a1	2.000	-0.8945	a1	2.000	-0.9054
b2	**2.000**	**-0.7928**	**b2**	**1.992**	**-0.7910**	**b2**	**1.992**	**-0.7898**
b1	2.000	-0.7777	b1	2.000	-0.7796	b1	2.000	-0.7820
a1	2.000	-0.6861	a1	2.000	-0.6857	a1	2.000	-0.6858
b1	2.000	-0.6848	b1	2.000	-0.6844	b2	2.000	-0.6845
b2	2.000	-0.6848	b2	2.000	-0.6844	b1	2.000	-0.6845
a2	**1.000**	**-0.4288**	**a1**	**1.002**	**-0.4361**	**a1**	**1.002**	**-0.4372**
a1	**1.000**	**-0.4278**	**a2**	**1.002**	**-0.4300**	**a2**	**1.002**	**-0.4297**
b1	**1.000**	**-0.4226**	**b1**	**1.002**	**-0.4240**	**b1**	**1.002**	**-0.4236**
a1	**1.000**	**-0.3915**	**a1**	**1.001**	**-0.3814**	**a1**	**1.001**	**-0.3793**
a1	**1.000**	**-0.3147**	**a1**	**1.000**	**-0.3184**	**a1**	**1.000**	**-0.3186**
			b2	0.007	1.4091	b2	0.007	1.5071
			b1	0.003	2.9073	b1	0.003	2.8252
			a1	0.003	3.8670	a1	0.003	3.8149

a. Thefirst section represents the inner shells, *i.e.* Fe_1s, Ar_1s, Fe_2s, Fe_2p, w_1s, Ar_2s, Ar_2p, Fe_3s orbitals. The second section represents Fe_3p orbitals. The third section represents w_2s, Ar_3s orbitals. The last section represents all the other orbitals within the active space.

Table 31. Orbital symmetry, occupation number, and orbital energy (in hartree) of $^6A_2$ $Fe^+(H_2O)Ar$ where argon atom is bound to Fe^+ for various CASSCF calculations.

(7, 6)			(13, 12)			(19, 15)		
sym	Occ	Energy	sym	Occ	Energy	sym	Occ	Energy
a1	2.000	-261.6127	a1	2.000	-261.6051	a1	2.000	-261.6041
a1	2.000	-118.7044	a1	2.000	-118.7044	a1	2.000	-118.7044
a1	2.000	-32.1728	a1	2.000	-32.1638	a1	2.000	-32.0403
a1	2.000	-27.6632	a1	2.000	-27.5657	a1	2.000	-27.5645
b2	2.000	-27.6467	b2	2.000	-27.5530	b2	2.000	-27.5521
b1	2.000	-27.6466	b1	2.000	-27.5528	b1	2.000	-27.4429
a1	2.000	-20.8353	a1	2.000	-20.8347	a1	2.000	-20.8349
a1	2.000	-12.4154	a1	2.000	-12.4155	a1	2.000	-12.4154
a1	2.000	-9.6644	a1	2.000	-9.6645	a1	2.000	-9.6644
b2	2.000	-9.6644	b2	2.000	-9.6644	b2	2.000	-9.6644
b1	2.000	-9.6644	b1	2.000	-9.6644	b1	2.000	-9.6644
a1	2.000	-4.4064	a1	2.000	-4.3991	a1	2.000	-4.5149
a1	2.000	-2.9887	a1	1.996	-3.0667	a1	1.996	-3.0659
b2	2.000	-2.9795	b2	1.997	-3.0568	b2	1.997	-3.0557
b1	2.000	-2.9791	b1	1.997	-3.0563	b1	1.996	-3.0553
a1	2.000	-1.6329	a1	2.000	-1.6329	a1	2.000	-1.6333
a1	2.000	-1.3701	a1	2.000	-1.3702	a1	2.000	-1.3701
b2	2.000	-0.9993	b2	2.000	-0.9987	b2	2.000	-0.9992
a1	2.000	-0.9033	a1	2.000	-0.9053	a1	2.000	-0.9115
a2	**2.000**	**-0.7945**	b1	2.000	-0.7902	b1	2.000	-0.8994
b1	2.000	-0.7906	**a2**	**1.996**	**-0.7881**	**a2**	**1.997**	**-0.7874**
a1	2.000	-0.6844	a1	2.000	-0.6845	a1	2.000	-0.6845
b2	2.000	-0.6832	b2	2.000	-0.6832	b2	2.000	-0.6832
b1	2.000	-0.6832	b1	2.000	-0.6832	b1	2.000	-0.6832
b2	**1.000**	**-0.4219**	**a1**	**1.002**	**-0.4177**	**a1**	**1.003**	**-0.4177**
b1	**1.000**	**-0.4195**	**b2**	**1.002**	**-0.4170**	**b2**	**1.002**	**-0.4165**
a1	**1.000**	**-0.4111**	**b1**	**1.002**	**-0.4146**	**b1**	**1.002**	**-0.4140**
a1	**1.000**	**-0.3984**	**a1**	**1.001**	**-0.3837**	**a1**	**1.000**	**-0.3827**
a1	**1.000**	**-0.3138**	**a1**	**1.000**	**-0.3110**	**a1**	**1.000**	**-0.3107**
			b1	0.003	4.4642	b2	0.003	4.6257
			b2	0.003	4.4647	b1	0.003	4.6259
			a1	0.002	4.5634	a1	0.002	4.8328

a. Thefirst section represents the inner shells, *i.e.* Fe_1s, Ar_1s, Fe_2s, Fe_2p, w_1s, Ar_2s, Ar_2p, Fe_3s orbitals. The second section represents Fe_3p orbitals. The third section represents w_2s, Ar_3s orbitals. The last section represents all the other orbitals within the active space.

Table 32. Orbital symmetry, occupation number, and orbital energy (in hartree) of $^4A_1$ $Fe^+(H_2O)Ar$ where argon atom is bound to Fe^+ for various CASSCF calculations.

(7, 6)			(13, 12)			(19, 15)		
sym	Occ	Energy	sym	Occ	Energy	sym	Occ	Energy
a1	2.000	-261.5479	a1	2.000	-261.4741	a1	2.000	-261.5110
a1	2.000	-118.8177	a1	2.000	-118.8267	a1	2.000	-118.8319
a1	2.000	-32.0970	a1	2.000	-32.0054	a1	2.000	-31.9282
a1	2.000	-27.5854	b2	2.000	-27.3984	a1	2.000	-27.4351
b2	2.000	-27.5791	b1	2.000	-27.3973	b2	2.000	-27.4080
b1	2.000	-27.5782	a1	2.000	-27.3018	b1	2.000	-27.4051
a1	2.000	-20.8280	a1	2.000	-20.8168	a1	2.000	-20.8261
a1	2.000	-12.5280	a1	2.000	-12.5368	a1	2.000	-12.5421
a1	2.000	-9.7771	a1	2.000	-9.7859	a1	2.000	-9.7913
b2	2.000	-9.7768	b2	2.000	-9.7856	b2	2.000	-9.7909
b1	2.000	-9.7768	b1	2.000	-9.7856	b1	2.000	-9.7909
a1	2.000	-3.8397	a1	2.000	-4.1877	a1	2.000	-4.3652
b2	2.000	-2.9132	a1	1.997	-3.0823	b2	1.997	-3.0025
b1	2.000	-2.9123	b2	1.997	-2.9429	b1	1.997	-3.0023
a1	2.000	-2.8958	b1	1.997	-2.9423	a1	1.997	-2.9886
a1	2.000	-1.5681	a1	2.000	-1.6165	a1	2.000	-1.6285
a1	2.000	-1.4788	a1	2.000	-1.4908	a1	2.000	-1.4971
a1	2.000	-1.4779	b2	2.000	-0.9830	a1	2.000	-0.9554
b2	2.000	-0.9951	a1	2.000	-0.9126	b2	2.000	-0.9146
a1	2.000	-0.8141	a1	2.000	-0.8181	b2	2.000	-0.8894
b1	2.000	-0.7895	b2	2.000	-0.7990	a1	2.000	-0.8304
b2	2.000	-0.7895	b1	2.000	-0.7990	b1	2.000	-0.8017
b1	2.000	-0.7846	b1	2.000	-0.7725	b1	2.000	-0.7931
a1	**2.000**	**-0.7393**	**a1**	**1.980**	**-0.6463**	**a1**	**1.975**	**-0.6789**
a1	**1.641**	**-0.5036**	**a1**	**1.958**	**-0.5877**	**a1**	**1.840**	**-0.5441**
b2	**1.000**	**-0.3592**	**b2**	**0.996**	**-0.2844**	**b2**	**1.002**	**-0.3235**
b1	**1.000**	**-0.3545**	**b1**	**0.996**	**-0.2801**	**b1**	**1.002**	**-0.3189**
a2	**1.000**	**-0.3302**	**a2**	**1.001**	**-0.2747**	**a2**	**1.001**	**-0.3027**
a1	**0.359**	**-0.1321**	**a1**	**0.043**	**0.3979**	**a1**	**0.164**	**-0.0039**
			a1	0.020	1.1047	a1	0.021	0.8574
			b2	0.008	1.3665	b2	0.003	4.7308
			b1	0.007	1.4385	b1	0.003	4.7576

a. Thefirst section represents the inner shells, *i.e.* Fe_1s, Ar_1s, Fe_2s, Fe_2p, w_1s, Ar_2s, Ar_2p, Fe_3s orbitals. The second section represents Fe_3p orbitals. The third section represents w_2s, Ar_3s orbitals. The last section represents all the other orbitals within the active space.

Table 33. Orbital symmetry, occupation number, and orbital energy (in hartree) of $^4B_1$ $Fe^+(H_2O)Ar$ where argon atom is bound to Fe^+ for various CASSCF calculations.

(7, 6)			(13, 12)			(19, 15)		
sym	Occ	Energy	sym	Occ	Energy	sym	Occ	Energy
a1	2.000	-261.4009	a1	2.000	-261.4385	a1	2.000	-261.4415
a1	2.000	-118.7969	a1	2.000	-118.8076	a1	2.000	-118.8092
a1	2.000	-31.9334	a1	2.000	-31.9771	a1	2.000	-31.7415
b2	2.000	-27.4195	b2	2.000	-27.4249	b2	2.000	-27.2844
a1	2.000	-27.4164	b1	2.000	-27.3266	b1	2.000	-27.1722
b1	2.000	-27.4158	a1	2.000	-27.3179	a1	2.000	-27.1698
a1	2.000	-20.7903	a1	2.000	-20.7997	a1	2.000	-20.8004
a1	2.000	-12.5066	a1	2.000	-12.5179	a1	2.000	-12.5194
b2	2.000	-9.7560	a1	2.000	-9.7671	a1	2.000	-9.7686
a1	2.000	-9.7474	b2	2.000	-9.7668	b2	2.000	-9.7683
b1	2.000	-9.7465	b1	2.000	-9.7668	b1	2.000	-9.7683
a1	2.000	-4.1789	a1	2.000	-4.2143	a1	1.999	-4.3772
a1	2.000	-2.7710	b1	1.998	-2.9395	a1	1.997	-3.1006
b2	2.000	-2.7703	a1	1.997	-2.9308	b1	1.998	-3.0660
b1	2.000	-2.7701	b2	1.995	-2.8442	b2	1.997	-2.9765
a1	2.000	-1.5872	a1	2.000	-1.5976	a1	2.000	-1.6000
a1	2.000	-1.4486	a1	2.000	-1.4719	a1	2.000	-1.4742
b2	2.000	-0.9555	b2	2.000	-0.9660	b2	2.000	-0.9827
a1	2.000	-0.8434	a1	2.000	-0.8645	a1	2.000	-0.9184
a1	1.996	-0.8036	a1	2.000	-0.7991	a1	2.000	-0.8193
b1	1.993	-0.7780	b1	2.000	-0.7811	b1	2.000	-0.8025
b2	2.000	-0.7711	b2	2.000	-0.7809	b2	2.000	-0.7830
b1	2.000	-0.7470	b1	2.000	-0.7556	b1	2.000	-0.7714
b1	**2.000**	**-0.5913**	**b1**	**1.983**	**-0.6151**	**b1**	**1.983**	**-0.6218**
a1	**2.000**	**-0.5906**	**a1**	**1.971**	**-0.5900**	**a1**	**1.978**	**-0.6088**
b2	**1.000**	**-0.2179**	**a2**	**1.002**	**-0.2537**	**a2**	**1.001**	**-0.2538**
a2	**1.000**	**-0.2154**	**b2**	**1.001**	**-0.2486**	**b2**	**0.995**	**-0.2533**
a1	**1.000**	**-0.2075**	**a1**	**1.001**	**-0.2413**	**a1**	**0.994**	**-0.2435**
a1	**0.010**	**0.6023**	**a1**	**0.028**	**0.6618**	**a1**	**0.023**	**0.9033**
			b1	0.017	1.0705	a1	0.009	1.1876
			b2	0.005	2.0033	b1	0.018	1.2081
			a1	0.002	4.4848	b2	0.008	1.3933

a. Thefirst section represents the inner shells, *i.e.* Fe_1s, Ar_1s, Fe_2s, Fe_2p, w_1s, Ar_2s, Ar_2p, Fe_3s orbitals. The second section represents Fe_3p orbitals. The third section represents w_2s, Ar_3s orbitals. The last section represents all the other orbitals within the active space.

Table 34. Orbital symmetry, occupation number, and orbital energy (in hartree) of $^4B_2$ $Fe^+(H_2O)Ar$ where argon atom is bound to Fe^+ for various CASSCF calculations.

(7, 6)			(13, 12)			(19, 15)		
sym	Occ	Energy	sym	Occ	Energy	sym	Occ	Energy
a1	2.000	-261.4167	a1	2.000	-261.4306	a1	2.000	-261.4388
a1	2.000	-118.8037	a1	2.000	-118.8002	a1	2.000	-118.8073
a1	2.000	-31.9520	a1	2.000	-31.9553	a1	2.000	-31.7312
b1	2.000	-27.4396	a1	2.000	-27.3730	b1	2.000	-27.2936
b2	2.000	-27.4345	b1	2.000	-27.3677	b2	2.000	-27.1849
a1	2.000	-27.4329	b2	2.000	-27.2187	a1	2.000	-27.1666
a1	2.000	-20.7988	a1	2.000	-20.8024	a1	2.000	-20.8056
a1	2.000	-12.5141	a1	2.000	-12.5106	a1	2.000	-12.5176
a1	2.000	-9.7632	a1	2.000	-9.7597	a1	2.000	-9.7667
b1	2.000	-9.7630	b1	2.000	-9.7594	b1	2.000	-9.7664
b2	2.000	-9.7630	b2	2.000	-9.7594	b2	2.000	-9.7664
a1	2.000	-4.1740	a1	2.000	-4.0380	a1	1.999	-4.3992
b2	2.000	-2.7876	a1	1.995	-3.0138	a1	1.997	-3.0660
a1	2.000	-2.7872	b2	1.998	-2.9723	b2	1.998	-3.0556
b1	2.000	-2.7845	b1	1.996	-2.8777	b1	1.997	-2.9022
a1	2.000	-1.5953	a1	2.000	-1.5999	a1	2.000	-1.6056
a1	2.000	-1.4678	a1	2.000	-1.4647	a1	2.000	-1.4721
b2	2.000	-0.9637	b2	2.000	-0.9675	b2	2.000	-0.9801
a1	2.000	-0.8532	a1	2.000	-0.8790	a1	2.000	-0.9419
a1	2.000	-0.7900	a1	2.000	-0.7943	b1	2.000	-0.8350
b2	2.000	-0.7774	b2	2.000	-0.7741	a1	2.000	-0.8131
b1	2.000	-0.7770	b1	2.000	-0.7737	b2	2.000	-0.7876
b1	2.000	-0.7524	b1	2.000	-0.7613	b1	2.000	-0.7791
b2	**2.000**	**-0.6085**	**b2**	**1.984**	**-0.6676**	**b2**	**1.982**	**-0.6296**
a1	**1.978**	**-0.6057**	**a1**	**1.981**	**-0.6132**	**a1**	**1.979**	**-0.6089**
a2	**1.000**	**-0.2316**	**a2**	**1.001**	**-0.2429**	**a2**	**1.002**	**-0.2497**
b1	**1.000**	**-0.2272**	**b1**	**0.997**	**-0.2391**	**b1**	**0.996**	**-0.2478**
a1	**1.000**	**-0.2211**	**a1**	**0.998**	**-0.2336**	**a1**	**0.994**	**-0.2413**
a1_4s	**0.022**	**0.5972**	**a1**	**0.019**	**1.0732**	**a1**	**0.021**	**0.9787**
			b2	0.016	1.2680	a1	0.009	1.1710
			b1	0.007	1.5054	b2	0.018	1.1760
			a1	0.007	1.6257	b1	0.008	1.3981

a. Thefirst section represents the inner shells, *i.e.* Fe_1s, Ar_1s, Fe_2s, Fe_2p, w_1s, Ar_2s, Ar_2p, Fe_3s orbitals. The second section represents Fe_3p orbitals. The third section represents w_2s, Ar_3s orbitals. The last section represents all the other orbitals within the active space.

Table 35. Orbital symmetry, occupation number, and orbital energy (in hartree) of $^4A_2$ $Fe^+(H_2O)Ar$ where argon atom is bound to Fe^+ for various CASSCF calculations.

(7, 6)			(13, 12)			(19, 15)		
sym	Occ	Energy	sym	Occ	Energy	sym	Occ	Energy
a1	2.0000	-261.5478	a1	2.000	-261.5411	a1	2.000	-261.5469
a1	2.0000	-118.8177	a1	2.000	-118.8194	a1	2.000	-118.8175
a1	2.0000	-32.1004	a1	2.000	-32.0933	a1	2.000	-31.9713
a1	2.0000	-27.5859	a1	2.000	-27.5785	b1	2.000	-27.4903
b2	2.0000	-27.5786	b2	2.000	-27.5718	a1	2.000	-27.4901
b1	2.0000	-27.5785	b1	2.000	-27.5717	b2	2.000	-27.4893
a1	2.0000	-20.8278	a1	2.000	-20.8269	a1	2.000	-20.8288
a1	2.0000	-12.5280	a1	2.000	-12.5285	a1	2.000	-12.5279
a1	2.0000	-9.7771	a1	2.000	-9.7665	a1	2.000	-9.7770
b1	2.0000	-9.7768	b1	2.000	-9.7658	b1	2.000	-9.7767
b2	2.0000	-9.7768	b2	2.000	-9.7658	b2	2.000	-9.7767
a1	2.0000	-4.3378	a1	2.000	-4.3308	a1	2.000	-4.4650
a1	2.0000	-2.9277	a1	2.000	-2.9210	a1	1.996	-3.0154
b1	2.0000	-2.9126	b1	2.000	-2.9059	b2	1.997	-2.9981
b2	2.0000	-2.9125	b2	2.000	-2.9058	b1	1.997	-2.9972
a1	2.0000	-1.6264	a1	2.000	-1.6254	a1	2.000	-1.6286
a1	2.0000	-1.4819	a1	2.000	-1.4805	a1	2.000	-1.4819
b2	2.0000	-0.9948	b2	2.000	-0.9940	b2	2.000	-0.9412
a1	2.0000	-0.8966	a1	2.000	-0.8951	a1	2.000	-0.9029
a1	2.0000	-0.8076	a1	1.976	-0.8220	b2	2.000	-0.8454
b1	2.0000	-0.7896	b1	1.988	-0.8024	a1	2.000	-0.8079
b2	2.0000	-0.7895	b2	1.988	-0.8024	b1	2.000	-0.7893
b1	2.0000	-0.7844	b1	2.000	-0.7835	b1	2.000	-0.7867
a2	**1.9988**	**-0.7304**	**a2**	**1.999**	**-0.7240**	**a2**	**1.996**	**-0.7305**
a1	**1.6453**	**-0.5046**	**a1**	**1.675**	**-0.5085**	**a1**	**1.630**	**-0.4979**
b2	**1.0000**	**-0.3580**	**b2**	**1.000**	**-0.3513**	**b2**	**1.002**	**-0.3597**
b1	**1.0000**	**-0.3554**	**b1**	**1.000**	**-0.3486**	**b1**	**1.002**	**-0.3570**
a1	**1.0000**	**-0.3302**	**a1**	**1.000**	**-0.3244**	**a1**	**1.001**	**-0.3300**
a1	**0.3558**	**-0.1307**	**a1**	**0.327**	**-0.1151**	**a1**	**0.372**	**-0.1306**
			a1	0.017	0.5683	b1	0.003	4.5252
			b1	0.016	0.5805	b2	0.003	4.5334
			b2	0.016	0.5806	a1	0.002	4.5734

a. Thefirst section represents the inner shells, *i.e.* Fe_1s, Ar_1s, Fe_2s, Fe_2p, w_1s, Ar_2s, Ar_2p, Fe_3s orbitals. The second section represents Fe_3p orbitals. The third section represents w_2s, Ar_3s orbitals. The last section represents all the other orbitals within the active space.

BIBLIOGRAPHY

(1) *Cluster Ions*; Ng, C.-Y.; Baer, T.; Powis, I., Eds.; Wiley: Chichester, U.K., 1993.

(2) *Clusters of Atoms and Molecules*; Haberland, H., Ed.; Springer-Verlag: Berlin, 1994; Vol. 56.

(3) Mackay, A. L. *Acta. Crystallogr.* **1962**, *15*, 916.

(4) Harris, I. A.; Kidwell, R. S.; Northby, J. A. *Phys. Rev. Lett.* **1984**, *53*, 2390.

(5) Gutowsky, H. S.; Chuang, C.; Klots, K. D.; Emilsson, T.; Ruoff, R. S.; Krause, K. R. *J. Chem. Phys.* **1988**, *88*, 2919.

(6) Elrod, M. J.; Saykally, R. J. *J. Chem. Rev.* **1994**, *94*, 1975.

(7) Nesbitt, D. J. *Annu. Rev. Phys. Chem.* **1994**, *45*, 367.

(8) Buck, U.; Huisken, F.; Lauenstein, C.; Meyer, H.; Sronka, R. *J. Chem. Phys.* **1987**, *87*, 6276.

(9) Buck, U. *J. Phys. Chem.*, **1988**, *92*, 447.

(10) Huisken, F. *Adv. Chem. Phys.* **1992**, *81*, 63.

(11) Lisy, J. M. In *Cluster Ions*; Ng, C., Baer, T., Powis, I., Eds.; Wiley: Chichester, UK., 1993.

(12) Okumura, M.; Yeh, L. I.; Lee, Y. T. *J. Chem. Phys.* **1988**, *88*, 79.

(13) Okumura, M.; Yeh, L. I.; Myers, J. D.; Lee, Y. T. *J. Phys. Chem.* **1990**, *94*, 3416.

(14) Price, J. M.; Crofton, M. W.; Lee, Y. T. *J. Phys. Chem.* **1991**, *95*, 2182.

(15) Okumura, M.; Yeh, L. I.; Lee, Y. T. *J. Chem. Phys.* **1985**, *83*, 3705.

(16) Yeh, L. I.; Okumura, M.; Myers, J. D.; Price, J. M.; Lee, Y. T. *J. Chem. Phys.* **1989**, *91*, 7319.

(17) Nizkorodov, S. A.; Dopfer, O.; Ruchti, T.; Meuwly, M.; Maier, J. P.; Bieske, E. J. *J. Phys. Chem.* **1995**, *99*, 17118.

(18) Dopfer, O.; Nizkorodov, S. A.; Meuwly, M.; Bieske, E. J.; Maier, J. P. *Intl. J. Mass Spectrom. & Ion Processes* **1997**, *167*, 637.

(19) Olkhov, R. V.; Nizkorodov, S. A.; Dopfer, O. *Chem. Phys.* **1998**, *239*, 393.

(20) Olkhov, R. V.; Nizkorodov, S. A.; Dopfer, O. *J. Chem. Phys.* **1998**, *108*, 1.

(21) Dopfer, O.; Roth, D.; Maier, J. P. *J. Phys. Chem. A* **2000**, *104*, 11702.

(22) Dopfer, O.; Roth, D.; Maier, J. P. *J. Chem. Phys.* **2001**, *114*, 7081.

(23) Bailey, C. G.; Kim, J.; Dessent, C. E. H.; Johnson, M. A. *Chem. Phys. Lett.* **1997**, *269*, 122.

(24) Ayotte, P.; Weddle, G. H.; Kim, J.; Johnson, M. A. *Chem. Phys.* **1998**, *239*, 485.

(25) Ayotte, P.; Weddle, G. H.; Kim, J.; Johnson, M. A. *J. Am. Chem. Soc.* **1998**, *120*, 12361.

(26) Ayotte, P.; Bailey, C. G.; Kim, J.; Johnson, M. A. *J. Chem. Phys.* **1998**, *108*, 444.

(27) Nielson, S. B.; Ayotte, P.; Kelley, J. A.; Johnson, M. A. *J. Chem. Phys.* **1999**, *111*, 9593.

(28) Price, E. A.; Robertson, W. H.; Diken, E. G.; Weddle, G. H.; Johnson, M. A. *Chem. Phys. Lett.* **2002**, *366*, 412.

(29) Robertson, W. H.; Johnson, M. A. *Annu. Rev. Phys. Chem.* **2003**, *54*, 173.

(30) Armbruster, M.; Haberland, H.; Schindler, H.-G. *Phys. Rev. Lett.* **1981**, *47*, 323.

(31) Ayotte, P.; Johnson, M. A. *J. Chem. Phys.* **1997**, *106*, 811.

(32) Desfrancois, C.; Bailon, B.; Schermann, J. P.; Arnold, S. T.; Hendricks, J. H.; Bowen, K. H. *J. Chem. Phys.* **1991**, *95*, 7760.
(33) Ayotte, P.; Weddle, G. H.; Bailey, G. G.; Johnson, M. A.; Vila, F.; Jordan, K. D. *J. Chem. Phys.* **1999**, *110*, 6268.
(34) Barnett, R. N.; Landman, U.; Cleveland, C. L.; Jortner, J. *Chem. Phys. Lett.* **1998**, *145*, 382.
(35) Kim, K. S.; Lee, S.; Kim, J.; Lee, Y. Y. *J. Am. Chem. Soc.* **1997**, *119*, 9329.
(36) Smith, D. M. A.; Smets, J.; Elkadi, Y.; Adamowicz, L. *J. Chem. Phys.* **1997**, *107*, 5788.
(37) Kelley, J. A.; Weddle, G. H.; Robertson, W. H.; Johnson, M. A. *J. Chem. Phys.* **2002**, *116*, 1201.
(38) Weber, J. M.; Kim, J.; Woronowicz, E. A.; Weddle, G. H.; Becker, I.; Cheshnovsky, O.; Johnson, M. A. *Chem. Phys. Lett.* **2001**, *339*, 337.
(39) Lee, H. M.; Lee, S.; Kim, K. S. *J. Chem. Phys.* **2003**, *119*, 187.
(40) Harberland, H.; Ludewigt, C.; Schindler, H.-G.; Worsnop, D. R. *Phys. Rev. A* **1987**, *36*, 967.
(41) Harberland, H.; Ludewigt, C.; Schindler, H.-G.; Worsnop, D. R. *Z. Phys. A* **1985**, *320*, 151.
(42) Bowen, K. H.; Eaton, J. G. In *The Structure of Small Molecules and Ions*; Naaman, R., Vager, Z., Eds.; Plenum: New York, 1988.
(43) Arnold, S. T.; Eaton, J. G.; Patel-Misra, D.; Sarkas, H. W.; Bowen, K. H. In *Ion and Cluster Ion Spectroscopy and Structure*; Maier, J. P., Ed.; Elsevier: Amsterdam, 1989.
(44) Bouteiller, Y.; Desfrancois, C.; Abdoul-Carime, H.; Shermann, J. P. *J. Chem. Phys.* **1996**, *105*, 6420.
(45) Coe, J. V.; Lee, G. H.; Eaton, J. G.; Arnold, S. T.; Sarkas, H. W.; Bowen, K. H.; Ludewigt, C.; Haberland, H.; Worsnop, D. R. *J. Chem. Phys.* **1990**, *92*, 3980.
(46) Wang, F.; Jordan, K. D. *Annu. Rev. Phys. Chem.* **2003**, *54*, 367.
(47) Fermi, E.; Teller, E. *Phys. Rev.* **1947**, *72*, 399.
(48) Turner, J. E.; Anderson, V. E.; Fox, K. **1968**, *174*, 81.
(49) Jordan, K. D. *Acc. Chem. Res.* **1979**, *12*, 36.
(50) Chipman, D. M. *J. Phys. Chem.* **1979**, *83*, 1657.
(51) Simons, J.; Jordan, K. D. *Chem. Rev.* **1987**, *87*, 535.
(52) Ayotte, P.; Johnson, M. A., private communication.
(53) Corelli, S. A.; Kelley, J. A.; Tully, J. C.; Johnson, M. A. *J. Phys. Chem. A* **2002**, *106*, 4872.
(54) Kroto, H. W.; J. R. Heath; O'brien, S. C.; Curl, R. F.; Smalley, R. E. *Nature* **1985**, *318*, 162.
(55) Gutowski, M.; Jordan, K. D.; Skurski, P. *J. Phys. Chem. A* **1998**, *102*, 2624.
(56) Gutowski, M.; Skurski, P.; Boldyrev, A.; Simons, J.; Jordan, K. D. *Phys. Rev. A* **1996**, *54*, 1906.
(57) Simons, J.; Skurski, P. In *Theoretical Prospect of Negative Ions*; Kalcher, J., Ed.; Research Signpost: India, 2002.
(58) Dang, L. X.; Chang, T. M. *J. Chem. Phys.* **1997**, *106*, 8149.
(59) Cohen, R. C.; Saykally, R. J. *J. Chem. Phys.* **1993**, *98*, 6007.
(60) Space, B.; Coker, D. F.; Liu, Z. H.; Berne, B. J.; Martyna, G. *J. Chem. Phys.* **1992**, *97*, 2002.

(61) Shepard, A. C.; Beers, Y.; Klein, G. P.; Rothman, L. S. *J. Chem. Phys.* **1973**, *59*, 2254.
(62) Verhoeven, J.; Dymanus, A. *J. Chem. Phys.* **1970**, *52*, 3222.
(63) Wang, F.; Jordan, K. D. *J. Chem. Phys.* **2002**, *116*, 6973.
(64) Kirkpatrick, S.; Gelatt, C. D.; Vecchi, M. P. *Science* **1983**, *220*, 671.
(65) Press, W. H.; Flannery, B. P.; Teukolky, S. A.; Vetterling, W. T. In *Numerical recipes in C: The Art of Scientific Computing 2nd edition*; Cambridge University Press, 1993.
(66) Ghayal, M. R.; Curotto, E. *J. Chem. Phys.* **1999**, *111*, 5522.
(67) Metropolis, N.; Rosenbluth, A. W.; Rosenbluth, M. N.; Teller, A. H.; Teller, E. *J. Chem. Phys.* **1953**, *21*, 1087.
(68) Gascón, J. A.; Hall, R. W.; Ludewigt, C.; Haberland, H. *J. Chem. Phys.* **2002**, *117*, 8391.
(69) Pople, J. A.; Head-Gordan, M.; Raghavachari, K. *J. Chem. Phys.* **1987**, *87*, 5968.
(70) Dunning, T. H., Jr. *J. Chem. Phys.* **1989**, *90*, 1007.
(71) Woon, D. E.; Dunning, T. H., Jr. *J. Chem. Phys.* **1993**, *98*, 1358.
(72) R. A. Kendall; T. H. Dunning, J.; Harrison, R. J. *J. Chem. Phys.* **1992**, *96*, 6796.
(73) Johnson, M. A., private communication.
(74) Weerasinghe, S.; Amar, F. G. *J. Chem. Phys.* **1993**, *98*, 4967.
(75) Frantz, D. D. *J. Chem. Phys.* **1995**, *102*, 3747.
(76) Frantz, D. D.; Freeman, D. L.; Doll, J. D. *J. Chem. Phys.* **1990**, *93*, 2769.
(77) Bieske, E. J.; Dopfer, O. *Chem. Rev.* **2000**, *100*, 3963.
(78) Duncan, M. A. *Int. J. Mass Spectrom.* **2000**, *200*, 545.
(79) *Organometallic Ion Chemistry*; Freiser, B. S., Ed.; Kluwer Academic Publishers: Dordrecht, The Netherlands, 1996.
(80) *Adv. Metal and Semiconductor Clusters*; Duncan, M. A., Ed.; Elsevier Science: Amsterdam, 2001; Vol. 5.
(81) Marinelli, P. J.; Squires, R. R. *J. Am. Chem. Soc.* **1989**, *111*, 4101.
(82) Dalleska, N. F.; Honma, K.; Sunderlin, L. S.; Armentrout, P. B. *J. Am. Chem. Soc.* **1994**, *116*, 3519.
(83) Clemmer, D. E.; Chen, Y.-M.; Aristov, N.; Armentrout, P. B. *J. Phys. Chem.* **1994**, *98*, 7538.
(84) Dalleska, N. F.; Tjelta, B. L.; Armentrout, P. B. *J. Phys. Chem.* **1994**, *98*, 4191.
(85) Meyer, F.; Khan, F. A.; Armentrout, P. B. *J. Am. Chem. Soc.* **1995**, *117*, 9740.
(86) Armentrout, P. B.; Baer, T. *J. Phys. Chem.* **1996**, *100*, 12866.
(87) Tjelta, B. L.; Armentrout, P. B. *J. Phys. Chem.* **1997**, *101*, 2064.
(88) Sievers, M. R.; Jarvis, L. M.; Armentrout, P. B. *J. Am. Chem. Soc.* **1998**, *120*, 1891.
(89) Rogers, M. T.; Armentrout, P. B. *Mass Spectrom. Rev.* **2000**, *19*, 215.
(90) Tjelta, B. L.; Walter, D.; Armentrout, P. B. *Int. J. Mass Spectrom.* **2001**, *204*, 7.
(91) Harms, A. C.; Khanna, S. N.; Chen, B.; Castleman, A. W., Jr. *J. Chem. Phys.* **1994**, *100*, 3540.
(92) Beyer, M. B. C.; Gorlitzer, H. W.; Schindler, T.; Achatz, U.; Albert, G.; Niedner-Schatteburg, G.; Bondybey, V. E. *J. Am. Chem. Soc.* **1996**, *118*, 7386.
(93) Beyer, M. A.; Achatz, U.; Berg, C.; Joos, S.; Niedner-Schatteburg, G.; Bondybey, V. E. *J. Phys. Chem. A* **1999**, *103*, 671.
(94) Bondybey, V. E.; Beyer, M. K. *Intl. Rev. Phys. Chem.* **2002**, *21*, 277.

(95) Fox, B. S.; Balteanu, I.; Balaj, O. P.; Liu, H.; Beyer, M. K.; Bondybey, V. E. *Phys. Chem. Chem. Phys.* **2002**, *4*, 2224.
(96) Berg, C.; Achatz, U.; Beyer, M. K.; Joos, S.; Albert, G.; Schindler, T.; Niedner-Schatteburg, G.; Bondybey, V. E. *Int. J. Mass Spectrom.* **1997**, *167*, 723.
(97) Berg, C.; Beyer, M. K.; Achatz, U.; Joos, S.; Niedner-Schatteburg, G.; Bondybey, V. E. *Chem. Phys.* **1998**, *239*, 379.
(98) Bondybey, V. E.; Beyer, M. K.; Achatz, U.; Fox, B.; Niedner-Schatteburg, G. *Adv. Met. & Semicond. Clusters* **2001**, *5*, 295.
(99) Rodriguez-Cruz, S.; Jockusch, R. A.; Williams, E. R. *J. Am. Chem. Soc.* **2002**, *121*, 1986.
(100) Bauschlicher, C. W., Jr.; Partridge, H. *J. Phys. Chem.* **1991**, *95*, 3946.
(101) Bauschlicher, C. W., Jr.; Sodupe, M.; Partridge, H. *J. Chem. Phys.* **1992**, *96*, 4453.
(102) Partridge, H.; Bauschlicher, C. W., Jr. *Chem. Phys. Lett.* **1992**, *195*, 494.
(103) Watanabe, H.; Iwata, S.; Hashimoto, K.; Misaizu, F.; Fuke, K. *J. Am. Chem. Soc.* **1995**, *117*, 755.
(104) Watanabe, H.; Iwata, S. *J. Phys. Chem. A* **1997**, *101*, 487.
(105) Watanabe, H.; Iwata, S. *J. Chem. Phys.* **1998**, *108*, 10078.
(106) Fuke, K.; Hashimoto, K. I., S. *Adv. Chem. Phys.* **1999**, *110*, 431.
(107) Watanabe, H.; Iwata, S. *J. Phys. Chem.* **1996**, *100*, 3377.
(108) Reinhard, B. M.; Niedner-Schatteburg, G. *J. Phys. Chem. A* **2002**, *106*, 7988.
(109) Reinhard, B. M.; Niedner-Schatteburg, G. *Phys. Chem. Chem. Phys.* **2002**, *4*, 1471.
(110) Reinhard, B. M.; Niedner-Schatteburg, G. *J. Chem. Phys.* **2003**, *118*, 3571.
(111) Markham, G. D.; Glusker, J. P.; Bock, C. W. *J. Phys. Chem. B* **2002**, *106*, 5118.
(112) Lessen, D. E.; Asher, R. L.; Brucat, P. J. *J. Chem. Phys.* **1990**, *93*, 6102.
(113) Willey, K. F.; Yeh, C. S.; Robbins, D.; Pilgrim, J. S.; Duncan, M. A. *J. Chem. Phys.* **1992**, *97*, 8886.
(114) Scurlock, C. T.; Pullins, S. H.; Reddic, J. E.; Duncan, M. A. *J. Chem. Phys.* **1996**, *104*, 4591.
(115) Sanekata, M.; Misaizu, F.; Fuke, K. *J. Chem. Phys.* **1996**, *104*, 9768.
(116) Misaizu, F.; Sanekata, M.; Tsukamoto, K.; Fuke, K.; Iwata, S. *J. Phys. Chem.* **1992**, *96*, 8259.
(117) Sanekata, M.; Misaizu, F.; Fuke, K.; Iwata, S.; Hashimoto, K. *J. Am. Chem. Soc.* **1995**, *117*, 747.
(118) Fuke, K.; Hashimoto, K.; Takasu, R. *Adv. Met. & Semicond. Clusters* **2001**, *5*, 1.
(119) Yoshida, S.; Okai, N.; Fuke, K. *Chem. Phys. Lett.* **2001**, *347*, 93.
(120) Faherty, K. P.; Thompson, C. J.; Aquirre, F.; Michne, J.; Metz, R. B. *J. Phys. Chem.* **2001**, *105*, 10054.
(121) Thompson, C. J.; Husband, J.; Aguirre, F.; Metz, R. B. *J. Phys. Chem. A* **2000**, *104*, 8155.
(122) Husband, J.; Aguirre, F.; Thompson, C. J.; Laperle, C. M.; Metz, R. B. *J. Phys. Chem. A* **2000**, *104*, 2020.
(123) Wang, K.; Rodham, D. A.; McKoy, V.; Blake, G. A. *J. Chem. Phys.* **1998**, *108*, 4817.
(124) Agreiter, J. K.; Knight, A. M.; Duncan, M. A. *Chem. Phys. Lett.* **1999**, *313*, 162.

(125) Selegue, T. J.; Cabarcos, O. M.; Lisy, J. M. *J. Chem. Phys.* **1994**, *100*, 4790.
(126) Cabarcos, O. M.; Weinheimer, C. J.; Lisy, J. M. *J. Chem. Phys.* **1999**, *110*, 8429.
(127) Cabarcos, O. M.; Weinheimer, C. J.; Lisy, J. M. *J. Chem. Phys.* **1998**, *108*, 5151.
(128) Lisy, J. M. *Int. Rev. Phys. Chem.* **1997**, *16*, 267.
(129) Weinheimer, C. J.; Lisy, J. M. *Int. J. Mass Spectrom. Ion Processes* **1996**, *159*, 197.
(130) Weinheimer, C. J.; Lisy, J. M. *J. Phys. Chem.* **1996**, *100*, 15305.
(131) Weinheimer, C. J.; Lisy, J. M. *J. Chem. Phys.* **1996**, *105*, 2938.
(132) Vaden, T. D.; Forinash, B.; Lisy, J. M. *J. Chem. Phys.* **2002**, *117*, 4628.
(133) Vaden, T. D.; Weinheimer, C. J.; Lisy, J. M. *J. Chem. Phys.* **2004**, *121*, 3102.
(134) Walters, R. S.; Walker, N. R.; Pillai, E. D.; Duncan, M. A. *J. Chem. Phys.* **2003**, *119*, 10471.
(135) Walters, R. S.; Duncan, M. A. *Austr. J. Chem.* **2004**, *57*, 1145.
(136) Inokuchi, Y.; Ohshimo, K.; Misaizu, F.; Nishi, N. *Chem. Phys. Lett.* **2004**, *390*, 140.
(137) Inokuchi, Y.; Ohshimo, K.; Misaizu, F.; Nishi, N. *J. Phys. Chem. A* **2004**, *108*, 5034.
(138) Yeh, C. S.; Pilgrim, J. S.; Robbins, D. L.; Willey, K. F.; Duncan, M. A. *Int. Rev. Phys. Chem.* **1994**, *13*, 231.
(139) Pilgrim, J. S.; Berry, K. R.; Duncan, M. A. *J. Chem. Phys.* **1994**, *100*, 7945.
(140) Willey, K. F.; Yeh, C. S.; Robbins, D. L.; Duncan, M. A. *J. Chem. Phys.* **1993**, *98*, 1867.
(141) Reddic, J. E.; Duncan, M. A. *J. Chem. Phys.* **1999**, *110*, 9948.
(142) Pullins, S. H.; Scurlock, C. T.; Reddic, J. E.; Duncan, M. A. *J. Chem. Phys.* **1996**, *104*, 7518.
(143) France, M. R.; Pullins, S. H.; Duncan, M. A. *J. Chem. Phys.* **1998**, *109*, 8842.
(144) Duncan, M. A. *Annu. Rev. Phys. Chem.* **1997**, *48*, 69.
(145) Gregoire, G.; Brinkmann, N. R.; van Heijnsbergen, D.; Schaefer, H. F.; Duncan, M. A. *J. Phys. Chem. A* **2003**, *107*, 218.
(146) Duncan, M. A. *Int. Rev. Phys. Chem.* **2003**, *22*, 407.
(147) Linnartz, H.; Verdes, D.; Maier, J. P. *Science* **2002**, *297*, 1166.
(148) Fuji, A.; Fujimaki, E.; Ebata, T.; Mikami, N. *J. Chem. Phys.* **2000**, *112*, 6275.
(149) Fujimaki, E.; Fuji, A.; Ebata, T.; Mikami, N. *J. Phys. Chem.* **2001**, *105*, 4882.
(150) Pino, T.; Boudin, N.; Brechnignac, P. *J. Chem. Phys.* **1999**, *111*, 7337.
(151) Corcelli, S. A.; Kelley, J. A.; Tully, J. C.; Johnson, M. A. *J. Phys. Chem. A* **2002**, *106*, 4872.
(152) Nakanaga, T.; Ito, F. *Chem. Phys. Lett.* **2002**, *355*, 109.
(153) Walters, R. S.; Schleyer, P. v. R.; Corminboeuf, C.; Duncan, M. A. *J. Am. Chem. Soc.* **2005**, *127*, 1100.
(154) Gaussian 03, R. A., Frisch, M. J.; Trucks, G. W.; Schlegel, H. B.; Scuseria, G. E.; Robb, M. A.; Cheeseman, J. R.; Montgomery, J. A.; Vreven, T.; Kudin, K. N.; Burant, J. C.; Millam, J. M.; Iyengar, S. S.; Tomasi, J.; Barone, V.; Mennucci, B.; Cossi, M.; Scalmani, G.; Rega, N.; Petersson, G. A.; Nakatsuji, H.; Hada, M.; Ehara, M.; Toyota, K.; Fukuda, R.; Hasegawa, J.; Ishida, M.; Nakajima, T.; Honda, Y.; Kitao, O.; Nakai, H.; Klene, M.; Li, X.; Knox, J. E.; Hratchian, H. P.; Cross, J. B.; Adamo, C.; Jaramillo, J.; Gomperts, R.; Stratmann, R. E.; Yazyev, O.; Austin, A. J.; Cammi, R.; Pomelli, C.; Ochterski, J. W.; Ayala, P. Y.;

Morokuma, K.; Voth, G. A.; Salvador, P.; Dannenberg, J. J.; Zakrzewski, V. G.; Dapprich, S.; Daniels, A. D.; Strain, M. C.; Farkas, O.; Malick, D. K.; Rabuck, A. D.; Raghavachari, K.; Foresman, J. B.; Ortiz, J. V.; Cui, Q.; Baboul, A. G.; Clifford, S.; Cioslowski, J.; Stefanov, B. B.; Liu, G.; Liashenko, A.; Piskorz, P.; Komaromi, I.; Martin, R. L.; Fox, D. J.; Keith, T.; Al-Laham, M. A.; Peng, C. Y.; Nanayakkara, A.; Challacombe, M.; Gill, P. M. W.; Johnson, B.; Chen, W.; Wong, M. W.; Gonzalez, C.; Pople, J. A., Gaussian, Inc., Pittsburgh PA, 2003.

(155) Kendall, R. A.; Dunning, T. H., Jr.; Harrison, R. J. *J. Chem. Phys.* **1992**, *96*, 6796.

(156) Fuentealba, P.; Szentpaly, L. V.; Preuss, H.; Stoll, H. *J. Phys. B* **1985**, *18*, 1287.

(157) Nicklass, A.; Dolg, M.; Stoll, H.; Preuss, H. *J. Chem. Phys.* **1995**, *102*, 8942.

(158) Boys, S. F.; Bernardi, F. *Mol. Phys.* **1970**, *19*, 553.

(159) Simon, S.; Duran, M.; Dannenberg, J. J. *J. Chem. Phys.* **1996**, *105*, 11024.

(160) Shimanouchi, T. *Molecular Vibrational Frequencies, 69 ed.*; Chemistry WebBook, NIST Standard Reference Database (http://webbook.nist.gov), 2001.

(161) Hegarty, D.; Robb, M. A. *Mol. Phys.* **1979**, *38*, 1795.

(162) Burgess, J. *Metal Ion in Solution*; John Wiley and Sons: New York, 1978.

(163) Dukan, L.; del Fabbro, L.; Pradel, P.; Sublemontier, O.; Mestdagh, J.-M.; Visticot, J.-P. *Eur. Phys. J. D* **1998**, *3*, 257.

(164) Poisson, L.; Pradel, P.; Lepetit, F.; Reau, F.; Mestdagh, J.-M.; Visticot, J.-P. *Eur. Phys. J. D* **2001**, *14*, 89.

(165) Poisson, L.; Dukan, L.; Sublemontier, O.; Lepetit, F.; Reau, F.; Pradel, P.; Mestdagh, J.-M.; Visticot, J.-P. *Int. J. Mass Spectrom.* **2002**, *220*, 111.

(166) Feller, D.; Glendening, E. D.; de Jong, W. A. *J. Chem. Phys.* **1999**, *110*, 1475.

(167) Ricca, A.; Bauschlicher, C. W., Jr. *J. Phys. Chem.* **1995**, *90*, 9003.

(168) Rosi, M.; Bauschlicher, C. W., Jr. *J. Chem. Phys.* **1990**, *92*, 1876.

(169) Rosi, M.; Bauschlicher, C. W., Jr. *J. Phys. Chem.* **1989**, *90*, 7264.

(170) Schäfer, A.; Hubert, C.; Ahlrichs, R. *J. Chem. Phys.* **1994**, *100*, 5829.

(171) Wachters, A. J. *J. Chem. Phys.* **1970**, *52*, 1033.

(172) Hay, P. J. *J. Chem. Phys.* **1971**, *66*, 4377.

(173) Raghavachari, K.; Trucks, G. W. *J. Chem. Phys.* **1989**, *91*, 1062.

(174) Werner., H.-J. *Mol. Phys.* **1996**, *89*, 645.

(175) Becke, A. D. *J. Chem. Phys.* **1993**, *98*, 5648.

(176) Amos, R. D.; Bernhardsson, A.; Berning, A.; Celani, P.; Cooper, D. L.; Deegan, M. J. O.; Dobbyn, A. J.; Eckert, F.; Hampel, C.; Hetzer, G.; Knowles, P. J.; Korona, T.; Lindh, R.; Lloyd, A. W.; McNicholas, S. J.; Manby, F. R.; Meyer, W.; Mura, M. E.; Nicklass, A.; Palmieri, P.; Pitzer, R.; Rauhut, G.; Schütz, M.; Schumann, U.; Stoll, H.; Stone, A. J.; Tarroni, R.; Thorsteinsson, T.; Werner., H.-J. MOLPRO; 2002.1 ed.